Two-Speed Compressor Operation in a Refrigerator/Freezer

P. R. Srichai and C. W. Bullard

ACRC TR-121 July 1997

For additional information:

Air Conditioning and Refrigeration Center
University of Illinois
Mechanical & Industrial Engineering Dept.
1206 West Green Street
Urbana, IL 61801

(217) 333-3115

Prepared as part of ACRC Project 66
Cycling Performance of Refrigerator-Freezer System
C. W. Bullard, Principal Investigator

The Air Conditioning and Refrigeration Center was founded in 1988 with a grant from the estate of Richard W. Kritzer, the founder of Peerless of America Inc. A State of Illinois Technology Challenge Grant helped build the laboratory facilities. The ACRC receives continuing support from the Richard W. Kritzer Endowment and the National Science Foundation. The following organizations have also become sponsors of the Center.

Amana Refrigeration, Inc.
Brazeway, Inc.
Carrier Corporation
Caterpillar, Inc.
Copeland Corporation
Dayton Thermal Products
Delphi Harrison Thermal Systems
Eaton Corporation
Ford Motor Company
Frigidaire Company
General Electric Company
Hydro Aluminum Adrian, Inc.
Indiana Tube Corporation
Lennox International, Inc.
Modine Manufacturing Co.
Peerless of America, Inc.
Redwood Microsystems, Inc.
The Trane Company
Whirlpool Corporation
York International, Inc.

For additional information:

Air Conditioning & Refrigeration Center
Mechanical & Industrial Engineering Dept.
University of Illinois
1206 West Green Street
Urbana IL 61801

217 333 3115

Abstract

A two-speed compressor was installed in a side-by-side refrigerator in order to validate simulation results which predicted significant increases in energy efficiency due to better load matching and reduced temperature lift. The steady state system COP at the low compressor speed (2400 rpm) was found to increase by 12% to 19% when compared to the high compressor speed (3600 rpm). About 9% of the energy savings achieved at the low compressor speed were attributable to the lower temperature lift; most of the remainder was due to the fact that the compressor itself operated more efficiently at the low speed. The savings observed at the low speed are net of the penalty incurred by the heat exchanger fans consuming some of the energy savings during the longer on-cycles. Additional experiments demonstrated that a refrigerator's energy efficiency could be increased by reducing the condenser fan speed when operating at low ambient temperatures. The decrease in fan speed causes a re-distribution of charge from the condenser to the evaporator resulting in a reduction in evaporator superheat and an overall increase in evaporator capacity.

Table of Contents

Chapter

Appendix

List of Tables

List of Figures

Chapter 1

Introduction

1.1 Introduction

Multi-speed and variable-speed compressors are being examined as potential ways for manufacturers to increase the energy efficiency of refrigerator/freezer systems by better matching the loading conditions seen in a real refrigerator. If the refrigerator sees frequent door openings or if warm food is placed inside, then the refrigerator would be able to switch to a high speed in order to pull down the temperature. Since refrigerators are undisturbed most of the time, and are located in rooms where ambient temperatures are moderate, it could run at low speed the vast majority of the time. With continuously variable-speed compressors, continuous operation might be possible, which would eliminate all cycling losses (Krause and Bullard, 1996 and Coulter and Bullard, 1995) and possibly improve the reliability of the refrigerator. The scope of this project was limited to examination of a two-speed compressor. Results of this analysis will hopefully allow manufacturers to design refrigerator systems that are more energy efficient, while maintaining sufficient pull-down capability.

1.2 Purpose

The experimental work described in this report builds on simulation analyses performed by Woodall and Bullard (1997), analyzing the performance of refrigerator/freezer systems using a two-speed compressor. Woodall simulated a 20 cubic foot top mount refrigerator, for which the model had been carefully validated with a single-speed compressor. Since Woodall had no experimental data from a two-speed compressor, his analysis dealt mainly with energy savings obtainable from having a lower temperature lift on the compressor. This report analyzes experimental results obtained from a two-speed compressor, operating in a 25 cubic foot side-by-side refrigerator. Calculations of system COP reveal the origins of energy savings achieved. Additional experiments were also conducted at varying condenser fan speeds, to validate Woodall's simulations which showed that significant energy savings could be achieved.

1.3 Experimental refrigerator

The data for the two-speed compressor analysis were obtained from experiments with a 25 cubic foot, side-by-side Amana refrigerator, model SRD25S5W, charged with the factory recommended 5.125 ounces of R-134a. The original single speed Tecumseh compressor, model TP1390YXA, was replaced with a two-speed Americold compressor, model RV800. Testing for the refrigerator was conducted at four different ambient temperatures: 60 °F, 75 °F, 90 °F, and 100 °F and at the two different compressor speeds. The nominal compressor speeds of 2400 rpm and 3600 rpm were verified experimentally using accelerometers and found to be 2440-2500 rpm for the low speed and 3700-3840 rpm for the high speed. At each of the four ambient temperatures, the fresh food and freezer compartment temperatures were varied over a wide range in order to provide a sufficiently diverse data set for use in model validation. The wide range in fresh food and freezer compartment temperatures also allowed the compressor mass flow and power to vary across a range wide enough to develop compressor performance maps based on in-situ calorimetry (see Appendix I). In the fresh food compartment, two small 15 cfm muffin fans which consume 4W each were used to reduce stratification as described in Appendix A.

Chapter 2

Two-Speed Compressor

2.1 Evaporator capacity and power reduction

Experiments were conducted with the two-speed compressor over a wide range of cabinet compartment temperatures. Although this was done to validate component submodels and to generate reliable compressor performance maps (see Appendix I), it revealed surprising anomalies in evaporator performance which will be described below.

At each of the four ambient temperatures, there is a noticeable trend in the data for evaporating capacity and power to increase as the compartment temperatures rise. This can be seen in Figure 2.1 below which was performed at 75 °F ambient. The corresponding graphs for 60 °F, 90 °F, and 100 °F (see Appendix K) are similar and show the same trend except that the increase at the 90 °F and 100 °F is not as great as in the 60 °F and 75 °F. The increase in evaporator capacity and power is due to having a larger temperature difference occurring across the evaporator which will tend to increase the evaporating temperature and hence the refrigerant mass flow. For the 90 °F and 100 °F, the increase in evaporating temperature was not as great as in the 60 °F and 75 °F data.

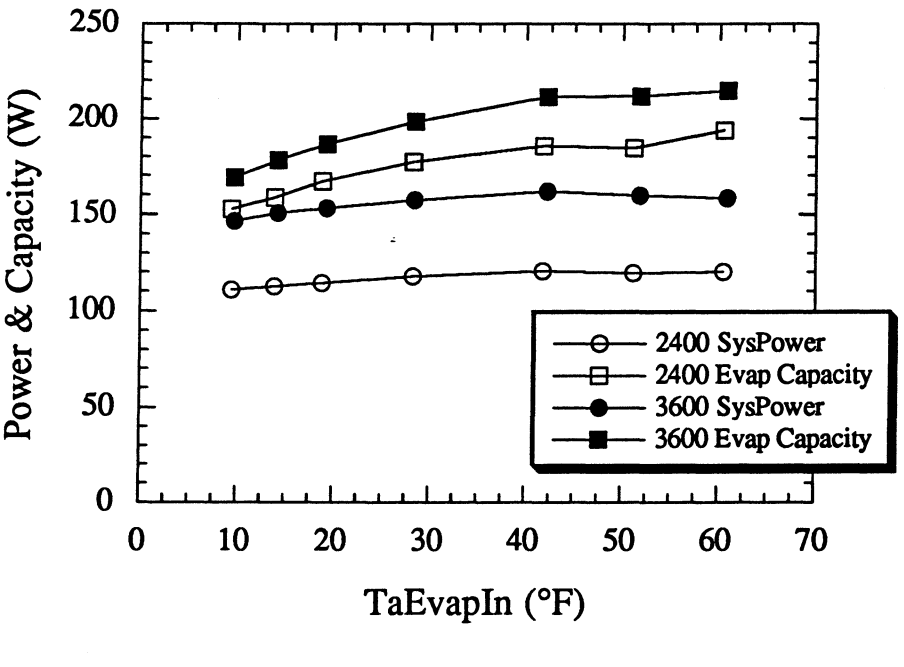

Figure 2.1 Capacity and power variation for two speeds

Comparing the 2400 and 3600 rpm operation reveals an average evaporator capacity difference for the four ambient temperatures of 11-14%, and an average system power difference of 21-27%. The greater reduction in the system power than evaporator capacity leads to an overall increase in COP at 2400 rpm.

2.2 COP increases

The system COP for each data point is calculated as the ratio of the evaporator capacity minus the evaporator fan to the system power as shown in Equation 2.1.

$$COP_{system,ss} = \frac{\dot{Q}_{evap\,load} - \dot{W}_{evap\,fan}}{\dot{W}_{system}} \tag{2.1}$$

where:

$$\dot{Q}_{evap\,load} = UA_z \cdot (T_{amb} - T_{az}) + UA_f \cdot (T_{amb} - T_{af}) + \dot{W}_{frez} + \dot{W}_{freshf} + \dot{Q}_{liq\,line} \tag{2.2}$$

The evaporator load is calculated by adding the known heat leakage through the cabinet walls (see Appendix B for a description of reverse heat leak tests) and the heater power input to each compartment. The refrigerator had a long liquid line (post-condenser loop) used for preventing moisture condensation near the door gasket. Although the liquid line heat transfer is small (less than 5% of evaporator capacity), most its heat is transferred into the cabinet walls so it was necessary to include it for the evaporator load calculation.

Table 2.1 Net COP gain

Ambient Temp (°F)	COP		COP gain (%)
	2400 RPM	3600 RPM	
60	1.6	1.3	19
75	1.4	1.2	19
90	1.1	1.0	14
100	1.0	0.9	12

The increase in system COP associated with running the compressor at the low speed is shown in Table 2.1. For each ambient temperature listed, system COP was calculated from measured capacity based on compressor and fan powers for an inlet evaporator air temperature of 12 °F. The 12 °F is typical of the inlet evaporator air that refrigerators experience during operation.

The system COP can increase as much as 19% in a 60 °F ambient room and 12% in a 100 °F ambient room. Previous simulation results by Woodall had identified a 9% energy savings due to the reduced temperature lift in a top-mount refrigerator. For the actual compressor tested in our side-by-side Amana test unit, 15% additional energy savings were achieved because the compressor is approximately 15% more efficient running at the low speed. However, some of those energy savings is lost due to the offsetting effect of the fans consuming more energy during the longer on-cycle. The savings shown in Table 2.1 are net savings.

2.3 Effects of reducing condenser fan speed

The idea of reducing the condenser fan speed was first examined by Woodall and Bullard (1997), whose simulations suggested that energy savings could be achieved at low ambient temperatures where the evaporator is often highly superheated and the condenser highly subcooled. When the condenser fan speed is decreased, the air-side heat transfer coefficient will decrease and raise the condensing temperature, thus reducing the amount of subcooling in the condenser. The extra charge then migrates to the evaporator where it reduces the amount of superheat, thus increasing the overall evaporator UA and increasing evaporating temperature and capacity.

To test this hypothesis, experiments were performed at the low compressor speed of 2400 rpm, the speed most multi-speed refrigerators would operate. In these experiments, only small energy savings were achieved by reducing the condenser fan speed. These observations, however were not inconsistent with Woodall's simulations, because there was no subcooling existing at the capillary tube inlet of our test unit. Since the capillary tube inlet was 2-phase, only about half as much refrigerant migrated to the evaporator compared to a subcooled case. Therefore the superheat was decreased only slightly, resulting in only a slight increase in the evaporating temperature.

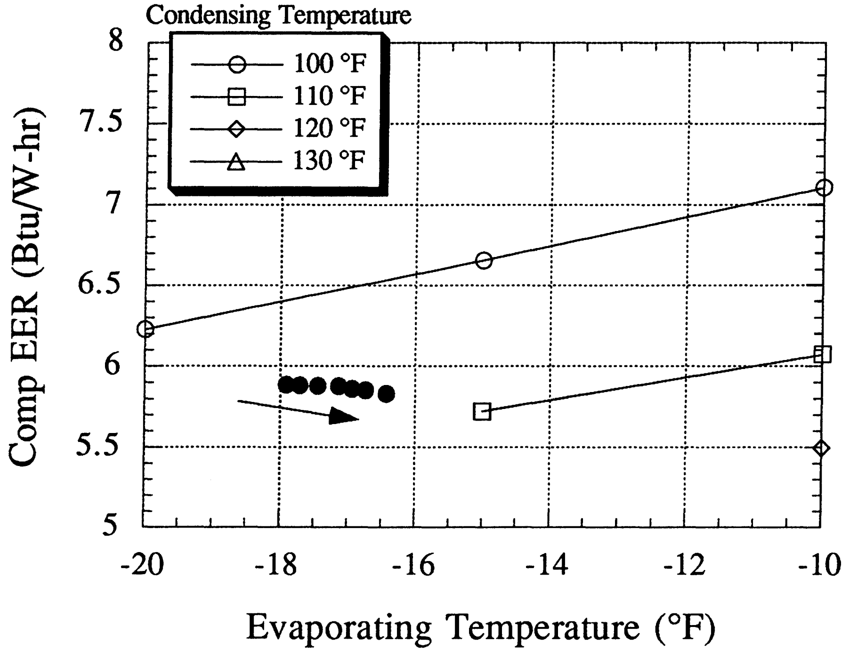

Figure 2.2 Compressor EER map showing effects of reducing condenser fan speed

The compressor performance maps showed that EER remained constant when the fan speed was initially reduced because the increase in condensing temperature offset the effect of the increasing evaporating temperature (see Figure 2.2). Therefore, the only energy savings achieved were at the condenser fan.

Another factor responsible for the small energy savings is the efficiency of the condenser fan itself. The permanent split capacitor motor used for the condenser fan was not designed for variable speed operation. Therefore, its efficiency declines as the speed is reduced. Had a constant efficiency DC fan been used, then the power consumption should decrease as the cube of the speed reduction as suggested by the fan law shown in Equation 2.3.

$$\frac{\mathrm{Power}_{\mathrm{new}}}{\mathrm{Power}_{\mathrm{nominal}}} = \left(\frac{N_{\mathrm{new}}}{N_{\mathrm{nominal}}}\right)^3 \tag{2.3}$$

Figure 2.3 shows how the system COP changed as the condenser fan speed was reduced to about 65% of its nominal speed. In the experiment, the freezer and fresh food air temperatures were set to 5 °F and 45 °F respectively, first in a 90 °F and then in a 60 °F ambient chamber. Figure 2.3 shows how the optimal fan speed reduction depends on the ambient temperature. The lower the ambient temperature, the lower the optimal fan speed and the greater the energy savings, as predicted by Woodall's simulations. The effect of a constant-efficiency motor is also shown. The energy savings shown in Figure 2.3 would be larger in refrigerators where the capillary tube inlet is slightly subcooled at the 90 °F test condition, and therefore highly subcooled at normal kitchen temperature.

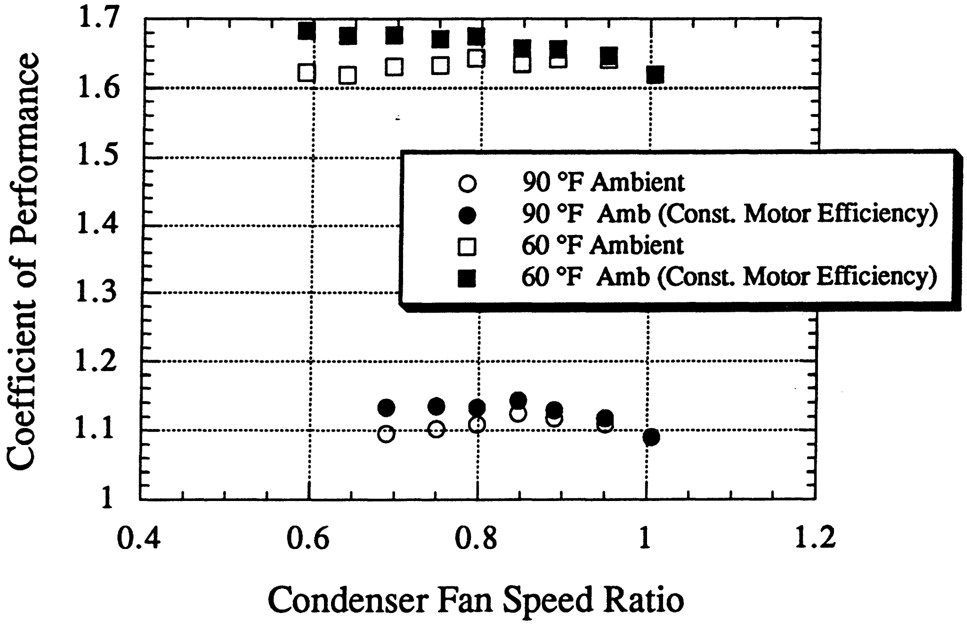

Figure 2.3 Varying condenser fan speed

The evaporating temperature increases as the condenser fan speed is reduced, so the maximum temperature difference between the air and refrigerant decreases. At low superheat (high-ambient operating conditions), an increase in evaporator capacity is not seen because the increase in overall evaporator UA is not sufficient to overcome the decrease in the air-refrigerant ΔT. On the other hand, at the higher superheat seen at the lower ambient temperatures, significant energy savings can be achieved via condenser fan speed reduction and the resultant redistribution of refrigerant to the evaporator.

2.4 Evaporator performance

2.4.1 Evaporator modeling for air-side heat transfer coefficient

The evaporator in the experimental refrigerator had both a counterflow and parallel flow configuration with respect to the air stream. In the initial modeling of the evaporator, it was assumed that the evaporator would consist of 3 zones as shown in Figure 2.4a.

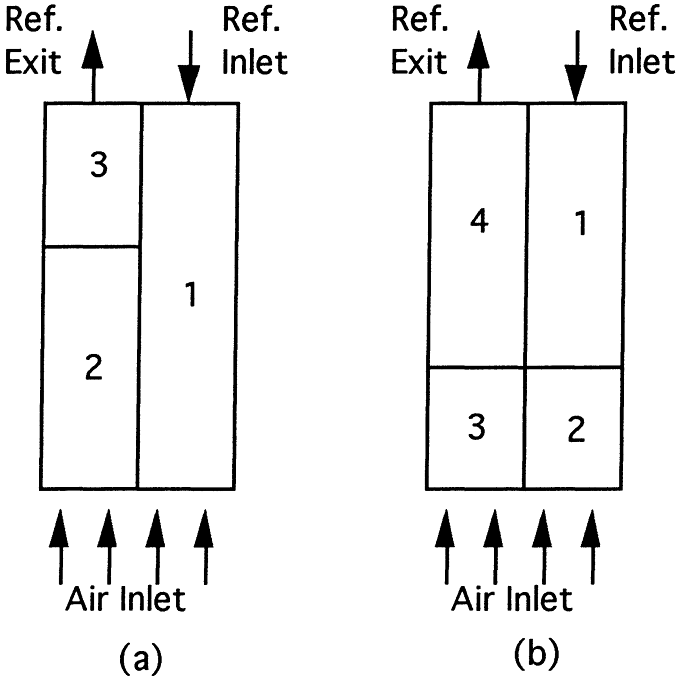

Figure 2.4 Three and four-zone model of evaporator

Zone 1 would consist of 2-phase refrigerant in counterflow with the inlet air, zone 2 would consist of 2-phase refrigerant in parallel flow, and zone 3 would consist of superheated vapor in parallel flow with the inlet air. This configuration for the evaporator model is consistent with that in the RFSIM model. The evaporator model was first used in the data reduction program in order to experimentally estimate the evaporator air-side heat transfer coefficient. Altogether, there were 24 steady state data points taken over a wide range of cabinet temperatures and ambient temperatures as described in Appendix D.

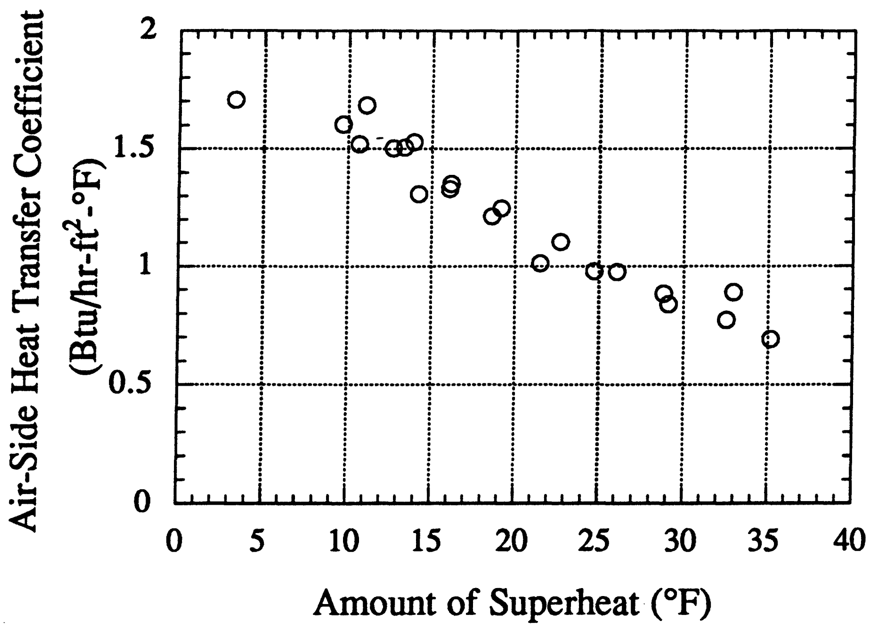

Figure 2.5 Air-side heat transfer coefficient versus superheat

Analysis of these data revealed that the air-side heat transfer coefficient had a large dependence on superheat (see Figure 2.5), which is clearly impossible because fan speed remained unchanged. As superheat increased, the calculated air-side heat transfer coefficient decreased by as much as 50% at the high superheat cases. The air-side heat transfer coefficient should not be a strong function of temperature, and the inlet velocity varied only slightly with cabinet air temperature at the constant volumetric flow rate. The 3 zone model predicted that the counterflow section of the evaporator would remain 2-phase until the exit superheat reached about 40 °F.

2.4.2 Experimental results from thermocouples on fins

Since the model was failing to predict heat transfer for superheat conditions greater than 15 °F, thermocouples were mounted at several locations on the evaporator fins (see Appendix G). At test conditions exceeding 15 degrees of measured superheat at the evaporator exit, the evaporator fin temperatures showed that already half of the evaporator consisted of superheated vapor. The fin temperatures at the leading edges of the fins measured nearly the same temperature as the inlet air temperature.

Figure 2.6 shows these fin surface temperatures along with the predicted refrigerant temperature distribution through the evaporator for a case having more than 15 °F of exit superheat. The inlet air temperature, and the surface temperatures, are measured values. The thin lines represent the calculated temperature drop for the two air temperatures. The thick line represents the predicted temperature distribution of the refrigerant through the evaporator. Notice that after all of the 2-phase refrigerant evaporates in the parallel flow section, the refrigerant can become highly superheated at the halfway point and then desuperheat as it proceeds to the exit. The colder part of the fin in the 2-phase counterflow region can extract heat through conduction to cool both the air and the refrigerant temperature in the parallel-flow section. Since the 3-zone model assumes that the entire counterflow section is 2-phase, such behavior could not be described.

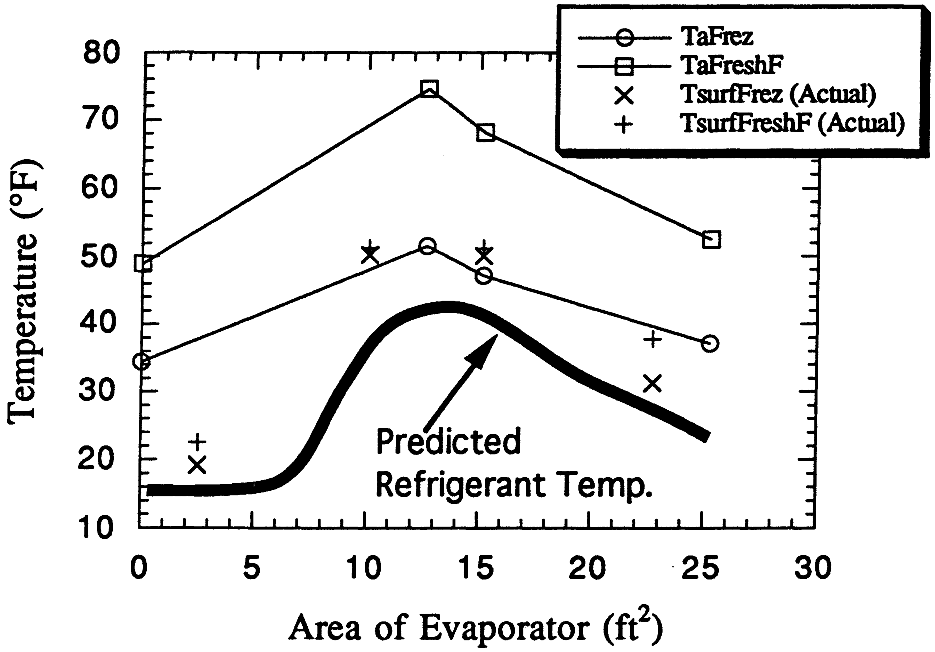

Figure 2.6 Prediction of refrigerant temperature at high superheat

2.4.3 Evaporator model with fixed air-side heat transfer coefficient

The next working hypothesis was to determine if the true value of the air-side heat transfer coefficient, approximately 1.6 Btu/hr-ft^2-°F, could be determined accurately by the 3-zone model using only the data having less than 15 °F of measured exit superheat. The air-side heat transfer coefficient calculated for such conditions is consistent with experiments performed by Korte (1997) on a similar evaporator using a single phase fluid for which the liquid heat transfer coefficient was accurately known. When an air-side heat transfer coefficient of 1.6 Btu/hr-ft^2-°F is used in the 3-zone model, it was found that the calculated exit superheat is overpredicted, but only slightly for calculated and measured superheat less than 15 °F. For data points having more than 15 °F of measured superheat, calculated values exceed 40 °F and the 3-zone model breaks down because the assumption that the counterflow half of the evaporator is 2-phase has been violated. It is also at 15 °F of measured superheat that the fin temperature experiment showed that half of the evaporator was superheated vapor. This supports the conclusion that the air-side heat transfer coefficient is actually 1.6 Btu/hr-ft^2-°F and that evaporator model inaccuracies account for the error inconsistencies observed.

2.4.4 4-zone modeling

Another model was then written for the evaporator, consisting of 4 zones as shown in Figure 2.4b. With the four zone model, zone 1 would be 2-phase while the other 3 zones would exist as superheated vapor. With the four zone model, desuperheating can now occur on the parallel-side of the heat exchanger (in the 3-zone model, superheat increased in the one superheated zone by definition). For the data points having measured superheat higher than 15 °F, the 4-zone model was used. The air-side heat transfer coefficient was fixed at 1.6 Btu/hr-ft^2-°F and the exit superheat calculated. The results showed that the 4-zone model is generally consistent with the fin temperature measurements shown in Figure 2.6, but it still underpredicts the exit superheat for all cases.

2.4.5 Fin conduction and contact resistance

Sensitivity analyses were then performed on fin conduction and contact resistance between the fins and tubes to see if they can explain why superheat is overpredicted in the 3-zone model for measured superheat less than 15 °F and underpredicted in the 4-zone model when the exit superheat is greater than 15 °F. For the original 3 and 4-zone models, fin conduction was modeled crudely by assuming a linear temperature distribution between the centroids of the zones. This approximation overpredicts conductive heat transfer because it neglects the flattening of the temperature distribution caused by the heat transfer from the air to the fin area between the zones. The temperature in the fin will actually remain relatively flat in the higher temperature zone and fall off sharply as it approaches the tube on the colder side of the fin.

Contact resistance between the fins and tubes is also unknown. Although other research has found that contact resistance is negligible and can be neglected on these types of dogbone fins, Davis, Jacobi, and Hrnjak (1996) compared nearly identical conventional and brazed evaporators and found that contact resistance can account for approximately 20% of the total heat exchanger resistance. Correcting both of these approximations tends to reduce or eliminate the error in predicting refrigerant superheat exit in both the 3 and 4-zone models.

2.5 Refrigerator system simulation

It is now clear that a very detailed model would be required in order to simulate performance of this geometrically complex evaporator under conditions of very high superheat (greater than 15 °F). However, at normal operating conditions, a simple 3-zone model is adequate in yielding good agreement with the cabinet calorimetry as shown in Figure 2.7. Since the superheated zone 3 is quite small when the difference between the refrigerant and air inlet temperatures (ΔT max) are less than 35 °F, the effects of interzone conductive heat transfer can also be neglected without sacrificing accuracy in the system simulation model.

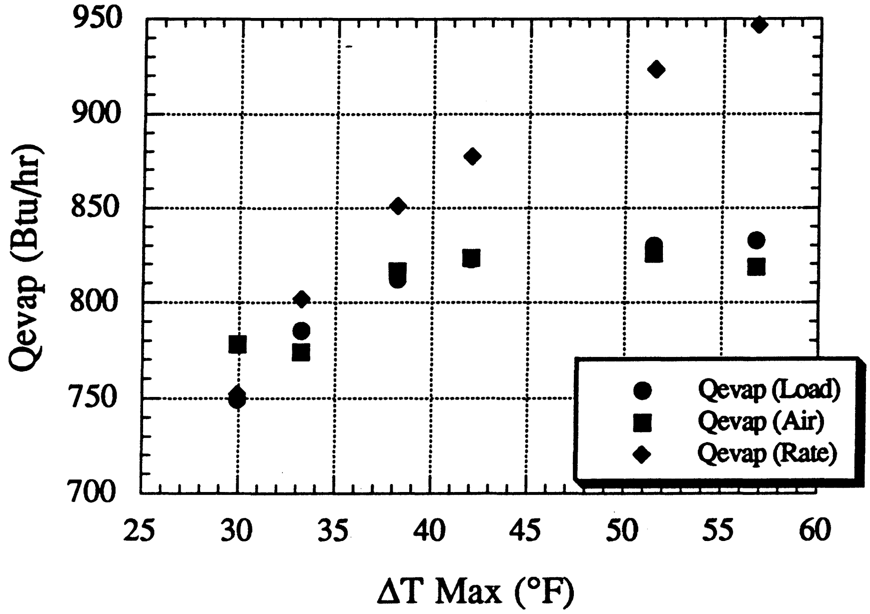

Figure 2.7 Evaporator capacity prediction

Chapter 3

Conclusions and Recommendations

The experiments reported here quantified the energy savings that could be achieved by running a two-speed compressor at a low speed most of the time, reserving high speed operation for extreme high ambient temperature conditions and when fast pull-down is required. Overall, net savings from 12% to 19% were observed in experiments conducted at 100 °F, 90 °F, 75 °F, and 60 °F. The energy savings are attributable to two factors: the reduced temperature lift; and the increase in compressor efficiency itself. Offsetting these savings are increased in fan energy during the longer on-cycles.

Reducing the condenser fan speed showed that up to a 5% increase in system COP could be achieved by using a condenser fan motor with an efficiency that did not deteriorate at low speed. The key benefit of this increase in COP is due to an increase in evaporator capacity from charge re-distribution from the condenser to the evaporator. Greater energy savings could have been achieved had subcooling existed at the capillary tube inlet. Energy savings are greatest at low (60-70 °F) ambients, but multi-speed operation might be justified on the basis of noise considerations alone.

A detailed analysis of the evaporator model was performed in order to understand its limitations. A very simple evaporator model will suffice at operating conditions that produce low evaporator superheat, producing results consistent with experimental observations. Low evaporator superheat is common when running simulations close to the design temperature of 5 °F and 38 °F in the freezer and fresh food compartments, respectively. The evaporator model predicts poorly at highly superheated conditions due mostly to the effects of fin conduction and possibly to contact resistance. A much more detailed (~40 zone) model would be required to accurately model performance of this geometrically complex evaporator under extreme conditions.

References

Admiraal, D.M., and C.W. Bullard, "Heat Transfer in Refrigerator Condensers and Evaporators," Transactions of the American Society of Heating, Refrigeration, and Air Conditioning Engineers, 101:1, 34-43, 1995.

Cavallaro, A.R., and C.W. Bullard, "Effects of Varying Fan Speed on a Refrigerator/Freezer System," Transactions of the American Society of Heating, Refrigeration, and Air Conditioning Engineers, 101:2, pp. 1218-1224, 1995.

Coriano, J., personal communication by Krause, 1993.

Coulter, W.H., and C.W. Bullard, "An Experimental Analysis of Cycling Losses in Domestic Refrigerator-Freezers," ACRC TR-77, University of Illinois at Urbana-Champaign, 1995.

Davis, G.L., and T.C. Scott, "Component Modeling Requirements for Refrigeration System Simulation." Purdue Compressor Technology Conference Proceedings, pp.401-408, 1976.

Davis, M.A., A.M. Jacobi, and P.S. Hrnjak, "Evaporator Calorimeter: The Study of Overall Heat Transfer Performance," ACRC TR-107, University of Illinois at Urbana-Champaign, 1996.

Dobson, M.K., and J.C. Chato, "Heat Transfer and Flow Regimes During Condensation in Horizontal Tubes," ACRC TR-57, University of Illinois at Urbana-Champaign, 1994.

Fischer, S.K., and C.K. Rice, "The Oak Ridge Heat Pump Models." Oak Ridge National Laboratory, 1983. ORNL/CON-80/R1.

Goodson, M.P., and C.W. Bullard, "Modelling a Refrigerator/Freezer System," ACRC TR-61, University of Illinois at Urbana-Champaign, 1994.

Grebner, J.J., and R.R. Crawford, "The Effects of Oil on the Thermodynamic Properties of Dichlorodifluoromethand (R-12) and Tetrafluoroethane (R-134a)," ACRC TR-13, University of Illinois at Urbana-Champaign, 1992.

Jensen, A.C., and W.E. Dunn, "Refrigerant-Side Instrumentation in Room Air-Conditioners," ACRC TR-101, 1996.

Kirby, E.S., and Bullard, C.W., "Effects of Airflow Nonuniformity on Room Air Conditioner Performance," University of Illinois at Urbana-Champaign, 1997.

Korte, C., personal communication, University of Illinois at Urbana-Champaign, 1997.

Krause, P.E., and C.W. Bullard, "Cycling and Quasi-Steady Behavior of a Refrigerator," Transaction of the American Society of Heating, Refrigeration, and Air Conditioning Engineers, 102:1, pp. 1061-1070, 1996.

Krause, P.E., notes, 1994.

Konczal, R., "Time Required for Refrigerant to Complete a Refrigeration Cycle," ME-393 project, University of Illinois at Urbana-Champaign, 1994.

Liu, Y., and C.W. Bullard, "An Experimental and Theoretical Analysis of Capillary Tube-Suction Line Heat Exchangers," ACRC TR-109, University of Illinois at Urbana-Champaign, 1997.

Porter, K., "Accuracy of Refrigerant Tube Surface Thermocouples," ACRC TM-12, University of Illinois at Urbana-Champaign, 1994.

Sanvordenker, K.S., "Durability of R-134a compressors: The role of the lubricant," ASHRAE Journal, February 1991, p. 42.

Staley, D.M., C.W. Bullard, and R.R. Crawford, "Steday-State Performance of a Domestic Refrigerator/Freezer Using R12 and R134a," University of Illinois at Urbana-Champaign, ACRC TR-22, 1992.

Stoecker, W.F., and J.W. Jones, Refrigeration and Air Conditioning, 2nd ed., New York: McGraw-Hill, 1986.

Wattelet, J.P., and J.C. Chato, "Heat Transfer Flow Regimes of Refrigerants in a Horizontal-Tube Evaporator," ACRC TR-55, University of Illinois at Urbana-Champaign, 1994.

Woodall, R.J., and C. W. Bullard, "Simulating effects of variable speed compressor on refrigerator/freezer performance," Transactions of the American Society of Heating, Refrigeration, and Air Conditioning Engineers, 103:1, in press, 1997.

Yoon. H., personal communication, 1995.

Appendix A

Side-by-Side Amana Instrumentation

A.1 Air-side instrumentation

Air-side thermocouples were placed throughout the fresh food and freezer compartment and along the air inlet and exit of the evaporator and condenser. The air-side thermocouples were made from 24 AWG type T thermocouples purchased from Omega Engineering. Since extra thermocouple wires were left over from the previous project, there are actually two batches of wire used in the instrumentation setup. Since each terminal panel which the thermocouple wires are connect to are calibrated separately, using two different batches of thermocouple wire should not affect the thermocouple measurements at all. The air-side thermocouples at the evaporator inlet and exit and both fresh food and freezer compartment where from the first batch and the air-side thermocouples on the inlet and exit of the condenser are from the second batch. The first batch of thermocouple wire is stated to have an uncertainty of ±1.8 °F while the second batch of thermocouple wires was of the same brand, but had a special limit of error on it so its uncertainty was ±0.7 °F. Once the thermocouples are placed inside the refrigerator they are calibrated a final time so that the real uncertainty is less than that stated by the manufacturer. Figure A.1 shows the location of the air-side thermocouples within the fresh food and freezer compartments.

A total of six air thermocouples are used to measure the average temperature of the freezer compartment and another six thermocouples are used to measure the average temperature of the fresh food compartment. Since only about 15% of the evaporator air actually makes it into the fresh food compartment, it was necessary to place two muffin fans, one in the middle and one at the bottom, in the fresh food compartment in order to reduce stratification. The muffin fans themselves use only 4 W and circulate 15 cfm of air each. In order to accurately measure a UA for our evaporator, accurate temperature measurements are needed at the evaporator inlet and exit. At the exit of the evaporator, four equally spaced thermocouples were placed behind the duct and the variations between the four thermocouples appeared to be only about ±0.8 °F. Further downstream of the duct, two more thermocouples were placed at the air inlet to the fresh food compartment. Although these two thermocouples are not used when calculating the evaporator exit air temperature during a refrigerator run, they are used extensively when a reverse heat leak test is performed when estimating the UA values of both food compartment. The inlet air stream to the evaporator consists of a mixing of air from both the fresh food and freezer compartment. Two thermocouples were placed at the fresh food inlet to the evaporator. At the freezer air inlet to the evaporator, six thermocouples are electrically averaged into two temperature readings. The variations between these two averaged temperature readings were about ±0.6 °F.

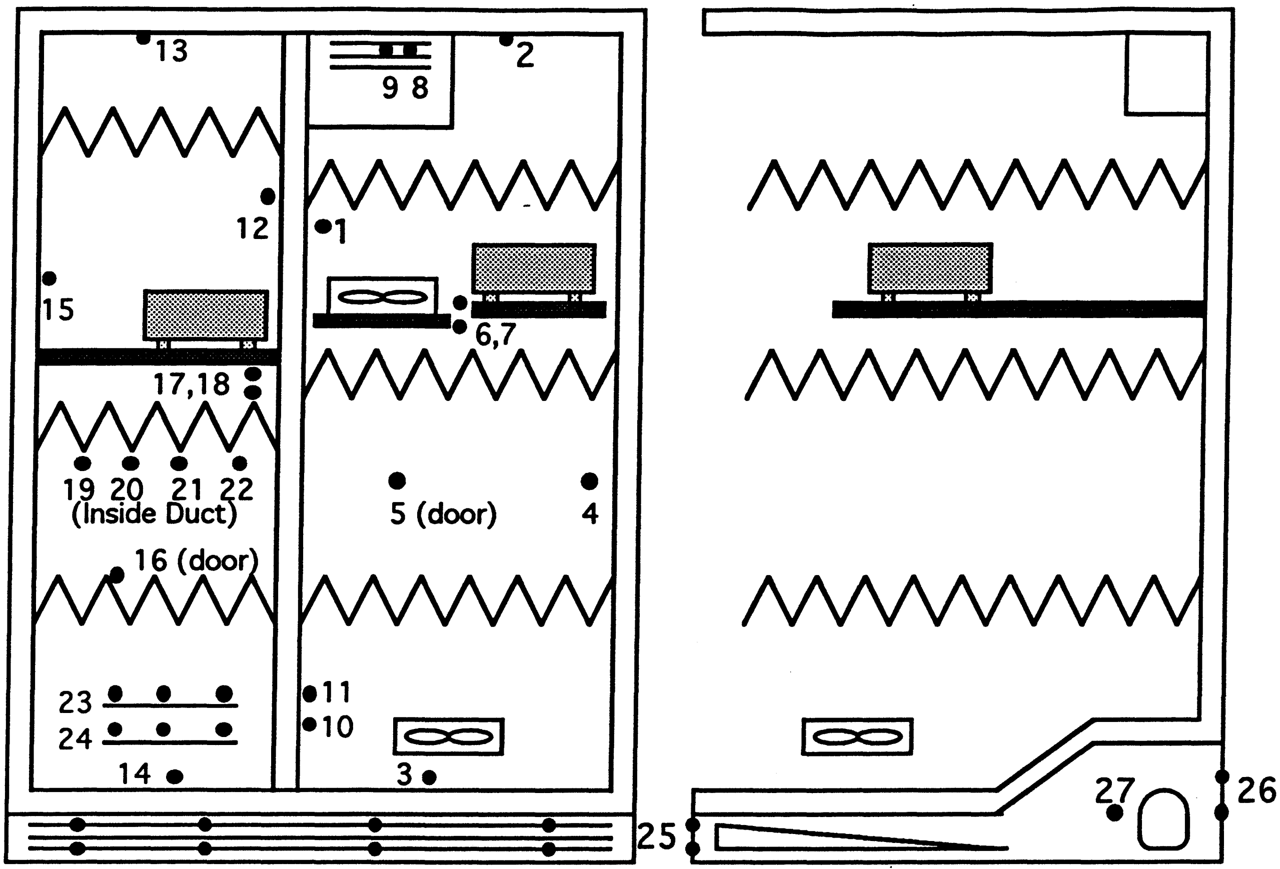

Figure A.1 Air-side configuration

Table A.1 Air-side thermocouple naming scheme

Number	Name	Number	Name	Number	Name
1	TA:FrigA	10	TA:FrmFrigA	19	TA:ToFrezA
2	TA:FrigB	11	TA:FrmFrigB	20	TA:ToFrezB
3	TA:FrigC	12	TA:FrezA	21	TA:ToFrezC
4	TA:FrigD	13	TA:FrezB	22	TA:ToFrezD
5	TA:FrigE	14	TA:FrezC	23	TA:FrmFrezT
6	TA:FrigF	15	TA:FrezD	24	TA:FrmFrezB
7	TA:FrigG	16	TA:FrezE	25	TA:GrilleIn
8	TA:ToFrigA	17	TA:FrezF	26	TA:CondFan
9	TA:ToFrigB	18	TA:FrezG	27	TA:CompIn

At the condenser air inlet, a total of eight thermocouples were placed on the grille equal distance apart and all eight thermocouples are electrically averaged into one temperature reading. At the exit of the condenser fan, a total of four air thermocouples are electrically averaged. One air-side thermocouple was placed right at the inlet air temperature for the compressor. This was done because the temperature right before the compressor is needed in order to estimate a UA for the compressor. Table A.1 explains the numbering scheme used in the air-side configuration and how each thermocouple was named.

A.2 Refrigerant-side instrumentation

In addition to the air-side thermocouples placed throughout the refrigerator, it was also necessary to install immersion thermocouples to measure the refrigerant temperature. Surface thermocouples were attached at the same location for comparison. Pressure transducers at the same location also allowed for enthalpy determination. Figure A.2 shows a diagram of the refrigerant tubing path and also the location of all the immersion thermocouples, surface thermocouples, and pressure transducers. Based on earlier instrumentation of refrigerators, it was determined that immersion thermocouples were necessary in only five locations. Since the inlet of the evaporator is always two-phase, it was decided to use a surface thermocouple at the evaporator inlet to approximate the refrigerant saturation temperature, and hence the pressure at the evaporator inlet. Since this refrigerator had an unusually long liquid line which is known as the post condenser loop, it was necessary to put a pressure transducer and immersion thermocouple at the liquid line exit. The liquid line for the refrigerator runs from the condenser exit to the front of the refrigerator where it is connected to the front metal plate which separates the freezer door from the fresh food door. By running the hot refrigerant in the liquid line to the front of the refrigerator, there is no need to put heaters in the mullion to reduce exterior moisture. This however does mean that there is an additional heat loss in the liquid line and an additional pressure drop which needs to be measured.

The immersion thermocouples used in the instrumentation procedure were T type thermocouples enclosed in a stainless steel sheath purchased from Omega Engineering part number TMQSS-020U-6 and TMQSS-032U-6. There are two part numbers listed because two different diameter thermocouples were used, 0.020 inch and 0.032 inch. From previous instrumentation experience, it was known that problems occurred with the immersion thermocouples breaking at the evaporator exit position. It was thought that problems occurred at the evaporator exit due to the fact that the 0.020 inch thermocouples were just too thin to take the force of the refrigerant exerted on them. Because of this, the 0.032 inch thermocouples were used at the evaporator exit and also at the compressor inlet due to the fact that the compressor inlet is where the refrigerant is at its highest velocity (Konczal, 1994). The placement of the larger diameter thermocouples at the evaporator exit and compressor inlet should not significantly affect the refrigerant flow. Based on cross-sectional area calculations, the tubing at evaporator exit and compressor inlet is the largest at 0.3125 inches. Therefore, the 0.032 inch thermocouples are taking up only approximately 1.5% of the internal area. The 0.020 inch thermocouples are placed in tubing that is 0.25 inch in diameter at the compressor exit and condenser exit and at one location where the tubing is 0.1875 inches in diameter at the liquid line exit. The total cross-sectional area that these thermocouples are taking up is approximately 1% and 2.5% respectively.

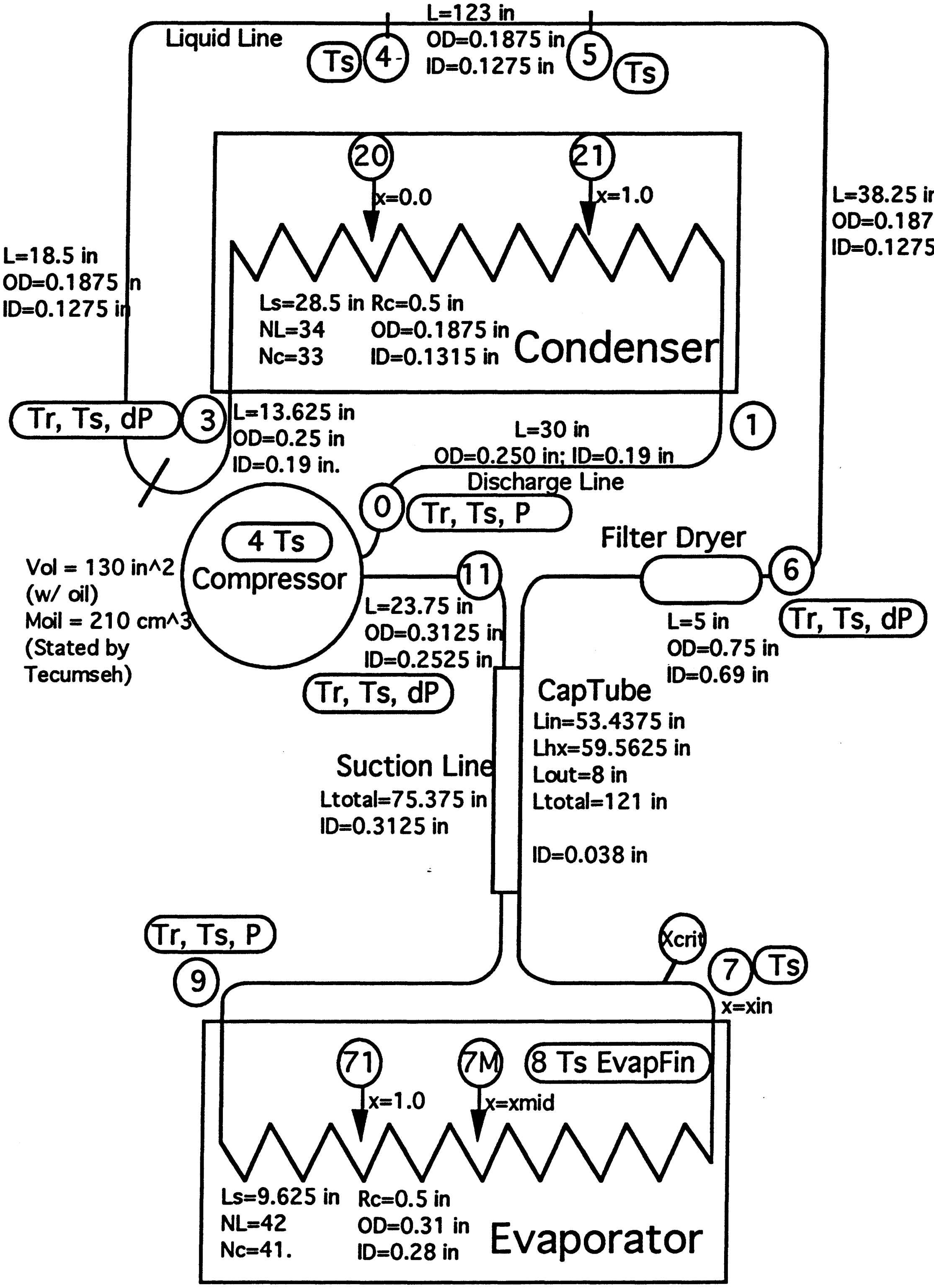

Figure A.2 Refrigerant loop for Amana refrigerator

At the five locations where the immersion thermocouples were placed, it was necessary to cut the refrigerant tubing and replace it with an instrumentation section. Figure A.3 shows the instrumentation section used for the installation of the immersion thermocouples. A 90° elbow is used for the placement of the immersion and surface thermocouples, and the immersion thermocouple and pressure transducer measurement are taken at the same point in the refrigerant tubing. Since the 90° elbow is used, it was necessary to find a natural bend in the refrigerant tubing where the refrigerant instrumentation section could be placed.

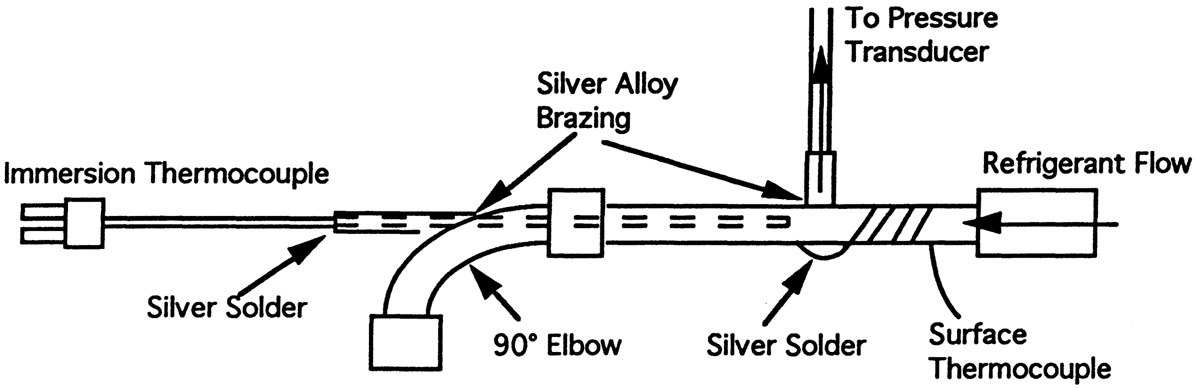

Figure A.3 Refrigerant instrumentation section

The surface thermocouples used in the refrigerator instrumentation were made from the 24 AWG type T thermocouples that were used in the air-side measurement. All of the surface thermocouples were made from the spool that had the special limits of error meaning that the manufacturer's uncertainty for the wire was ±0.7 °F. At the five locations where the immersion thermocouples were placed, the surface thermocouples were soldered to the refrigerant tubing. Also, on the liquid line tubing at point 4 and 5, the surface thermocouples were soldered to the tubing. The surface thermocouples at all the other locations were installed using an aluminum based thermal epoxy. This includes all of the surface thermocouples placed on the evaporator and on the compressor. For the compressor, there were four thermocouples installed at the top, bottom, front and back. For the eight surface thermocouples placed on the evaporator fin, four were place on one particular fin and the other four were place on another fin. The evaporator fins are basically rectangular in shape so the four thermocouples were placed approximately at all four corners of the fin. The first four thermocouples were placed on the tenth fin counting from the right side of the evaporator and the other four surface thermocouples were placed on the tenth fin counting from the left side of the evaporator.

All of the surface thermocouples installed on the refrigerant tubing were wrapped around the tubing about four times to ensure that the thermocouple wire saw the same temperature as the tubing thereby reducing any bias error that may occur from conduction down the thermocouple wire (Jensen and Dunn, 1996). After the thermocouple wire was wrapped around the tubing, approximately 0.25 inches of insulation was placed around the surface thermocouples (Porter, 1994). The only surface thermocouples not wrapped in insulation were the ones placed on the evaporator fins because wrapping them in insulation would disrupt the flow of air across the evaporator. The surface thermocouples on the evaporator fins were run up and down the fins to ensure that an accurate measurement of the evaporator fin was taken. A comparison can now be made to see how accurate out surface thermocouples are in estimating the refrigerant temperature. For the five surface thermocouples placed at the same location as the immersion thermocouples, data was taken to see how accurately they measured. Table A.2 shows compares the results observed over a range of operating conditions.

Table A.2 Immersion thermocouple measurement minus surface measurement

Thermocouple Location	Avg. Tr - Avg. Ts (°F)
Compressor Exit	14
Condenser Exit	0.2
Liquid Line Exit	0.2
Evaporator Exit	-5
Compressor Inlet	-3

All immersion and surface thermocouple were connected together with the air-side thermocouple to the thermocouple box and given a number. The air-side numbering is the same as that shown in Table A.1 and the numbering for the immersion and surface thermocouple is shown below in Table A.3

Table A.3 Refrigerant & surface thermocouple naming scheme

Number	Name	Number	Name	Number	Name
28	TR:CompIn	37	TS:CompShlT	46	TS:EvapOut
29	TR:CompOut	38	TS:CompShlB	57	TS:EvpfinPRB
30	TR:CondOut	39	TS:CompShlU	58	TS:EvpfinPRT
31	TS:MullionIn	40	TS:CompShlD	59	TS:EvpfinPLB
32	TS:MullionOut	41	TS:CompIn	60	TS:EvpfinPLT
33	TA:Chamber	42	TS:CompOut	61	TS:EvpfinCRB
34	TR:LiqLineout	43	TS:CondOut	62	TS:EvpfinCRT
35	TS:EvapIn	44	TS:LiqLineout	63	TS:EvpfinCLB
36	TR:EvapOut	45	TS:EvapoutAL	64	TS:EvpfinCLT

Currently there are only 48 temperature measurements, one terminal panel measures eight temperature, which can be measured at one moment in time. The thermocouple numbering scheme was designed such that the last terminal panel could be used to measure thermocouple 41-46 or 57-64. Thermocouple 57-64 contain the eight thermocouples placed on the evaporator fin while thermocouple 41-46 contain the surface thermocouples for which immersion thermocouple exist. Therefore there are two configurations for which data can be logged.

At each of the five locations that immersion thermocouples were placed, a pressure transducer was also installed. Across the condenser, liquid line, and suction line, differential pressure transducers were used. The differential pressure transducer were Setra Model C228-1. The differential pressure transducer were calibrated in house and are rated to have a range of 0 to 15 psid. At the compressor exit, a Setra Model 207 pressure transducer was used with a range of 0 to 250 psig. At the evaporator exit, there was a concern that perhaps the pressure might fall below atmospheric pressure so it was important that an absolute pressure transducer was used. The transducer used at the evaporator exit was a Setra Model C280E having a range of 0 to 100 psia. Both transducers, at the evaporator and compressor exit, were calibrated before they were installed.

A.3 Power instrumentation

In order to achieve cycling operation and steady state operation within the fresh food and freezer compartment, the thermostat which controls refrigerator cycling was rewired with a switch so that the experimental refrigerator could be used to test both operations. Resistance heaters were built for the two compartment so that different compartment temperatures could be achieved during the steady state operation. The heater wire was strung over a wood frame and made to fit the geometry of the two compartment. In order to attempt to get an even heating in the two compartments, each compartment had three heater frames that were placed such that they were approximately equidistant from each other and the wire was strung such that the total resistance of each individual heater was the same. Therefore each heater in the compartment will all have the same resistance and will therefore output the same wattage of heat as the other two. For the freezer compartment, the three heaters were placed on support brackets which was part of the original refrigerator from the original cabinets. For the fresh food heaters, a bracket frame located in the rear of the refrigerator was utilized. For two of the heaters, a bracket was attached to the rear such that they could be placed on the frame. For the third heater in the fresh food compartment, it was placed on a support frame which was part of the original refrigerator. In order to measure the amount of heat added to each compartment, watt transducers are used to measure the voltage and current sent to the heaters. The Watt transducers used for the heaters are manufactured from Scientific Columbus Model XL5C5-A2. In order to measure the power that the condenser fan and evaporator fan draws, the main electrical wire going to these fans were cut and wired into an Ohio Semitronics watt transducer. The watt transducer used for the evaporator fan is model PC5-103C and the model used for the condenser fan is model PC5-19E. In order to measure the power drawn by the compressor, a watt transducer is connected to the main power outlet that the refrigerator is plugged into. To obtain the compressor power, the power of both fans is subtracted from the total system power. The watt transducer used to measure the total system power is the same model as the one used to measure the condenser fan.

Appendix B

Conductance and Evaporator Air Flow Parameter Estimations

B.1 Whirlpool refrigerator

B.1.1 Split-air fraction and evaporator volumetric flow rate

The evaporator volumetric flow rate and split-air fraction are two important parameters needed in the refrigerator simulation model. In this analysis, these two parameters will be estimated using 25 steady state data points taken during the Fall 1995 semester. The Whirlpool refrigerator was used for acquiring data and the results will be compared to result found by Krause and Bullard (1996).

Previous work by Krause and Bullard (1996) had shown that the split-air fraction was 0.885 and the volumetric flow rate was 48.2 cfm, however, Krause had defined the split-air fraction on a mass basis. This analysis will take the density correction into consideration and define the split-air fraction on a volume basis. Realistically the density changes only slightly so the results on the volume basis should compare very well to the results on the mass basis. Krause also used a different experiment for calculating the volumetric flow rate. He initially placed a heater in the evaporator and performed an energy balance across the evaporator where he knew the power of the heater. The change in enthalpy across the control volume allowed him to calculate a volumetric flow rate. In this study, the evaporator load will be calculated from a steady-state energy balance around the entire refrigerator cabinets. After this, an energy balance will then be drawn across the evaporator where the evaporator load is known. Both experiments allow for the calculation of the volumetric flow rate, however it appears that the experiment performed by Krause should be more accurate since there are less parameters needed in his procedure.

Figure B.1 shows the control volumes used to estimate the volumetric flow rate and the split-air fraction. Equation B.1-4 show the equations used in the parameter estimation. Notice that a control volume is first drawn at the bottom of the evaporator in order to estimate Tma, the evaporator inlet mixed air temperature, and then another control volume is used to estimate the split-air fraction. In estimating the split-air fraction, the mass flow rate of the air needs to be known which leads to the estimation of the volumetric flow rate.

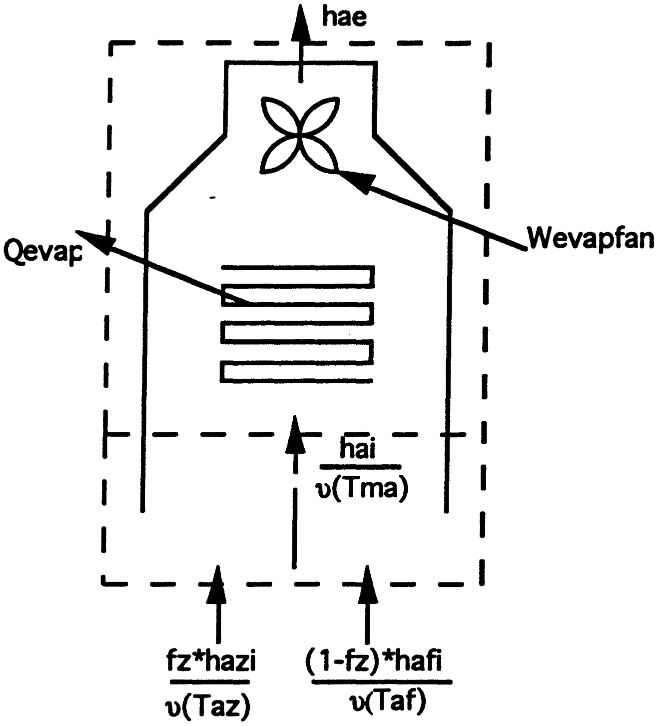

Figure B.1 Whirlpool evaporator geometry for f_z & $\dot{V}_{evap}$ estimation

$$\frac{h_{ai}(T_{ma})}{\upsilon(T_{ma},P_{atm})} = f_z \frac{h_{azi}(T_{frez})}{\upsilon(T_{frez},P_{atm})} + (1-f_z)\frac{h_{afi}(T_{frig})}{\upsilon(T_{frig},P_{atm})} \tag{B.1}$$

$$\dot{Q}_{evap} = w \cdot \left(h_{ai}(T_{ma}) - h_{aeo}(T_{evapout})\right) \tag{B.2}$$

$$\dot{Q}_{evap} = \dot{Q}_{frez} + \dot{Q}_{frig} + UA_{frez}(T_{amb} - T_{az}) + UA_{frig}(T_{amb} - T_{af}) + \dot{W}_{evapfan} \tag{B.3}$$

$$\dot{V}_{evap} = \frac{w \cdot \upsilon(T_{evapout},P_{atm})}{60} \tag{B.4}$$

The above equations were solved such that the f_z and $\dot{V}_{evap}$ parameters minimized the error between the measured and calculated evaporator load. The two UA parameters which are needed in this procedure are estimated in another procedure. Since the estimation of the UA parameters required knowing the f_z and $\dot{V}_{evap}$ parameters, the two procedures were reiterated until the final estimates of all the parameters were known. The best estimate of f_z was found to be 0.883 and $\dot{V}_{evap}$ was 51.6 cfm. Altogether there were 25 data steady state data points used in the estimation and Figure B.2 shows the scatter between the measured and calculated evaporator load.

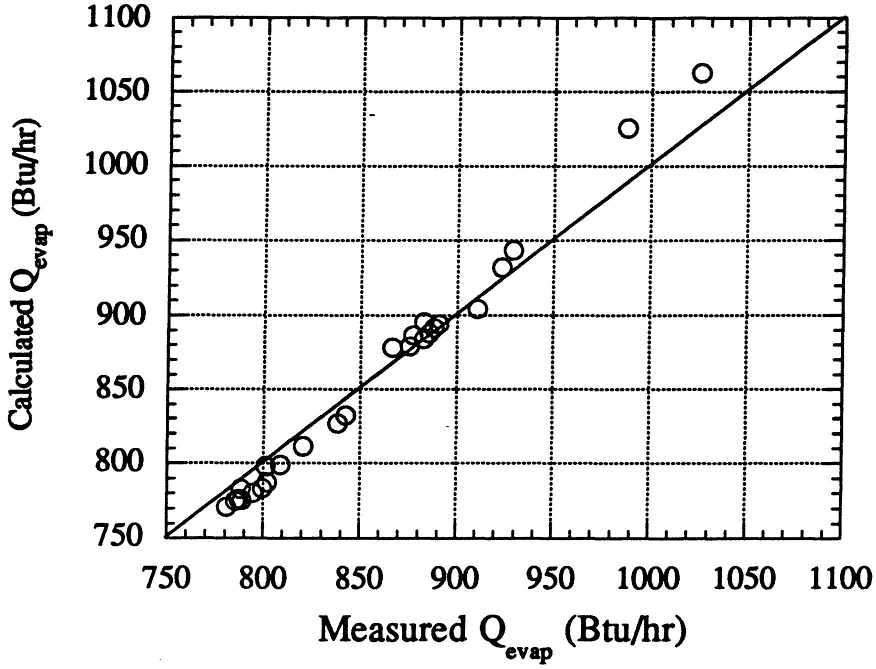

Figure B.2 Whirlpool evaporator volumetric flow and split-air estimation

Table B.1 Comparison of split-air fraction and volumetric flow rate for Whirlpool

	Spring 1994	Fall 1995
Split-air fraction	0.885	0.883
Volumetric flow rate	48.2 cfm	51.6 cfm

Table B.1 shows the comparison in the estimated split-air fraction and volumetric flow rate for the two data sets taken in the Spring of 1994 and in the Fall of 1995. The difference in the split-air fraction is only 0.2% while the difference in the volumetric flow rate is 6.6%. Some possible cause of errors in the calculations are the accuracy of our pressure and temperature measurement. All forty-eight thermocouples and five pressure taps were calibrated, but there are still some errors present in the calibration. It is known that the damper which controls the split-air fraction was moved and then placed back into its original position. This has the possibility of causing some error in the optimum value of the split-air fraction. Another cause for error in the split-air fraction is that the density correction applied could have changed the value. The 6.6% difference calculated for the volumetric flow rate is reasonably good considering that there was a greater chance for uncertainty in the Fall 1995 procedure.

B.1.2 Refrigerator cabinet conductances

The estimation of the two cabinet conductances is important in calculating the evaporator load from a steady-state energy balance around the entire refrigerator cabinets. In estimating the cabinet conductances, eight steady-state data points were taken where only the evaporator fan was running and the two compartmént temperatures where held greater than the ambient temperature. In order to eliminate the UA of the mullion, a measured amount of heat was inputted into each compartment such that both compartments remained at the same temperature until steady state was reached. Even if the two compartment temperatures did not match exactly, the $UA_{mullion}$ term would have had a negligible effect on the results as reported by Krause and Bullard (1996). A control volume was used as shown in Figure B.3 and an energy balance was set up to minimize the error between the calculated and measured power of both heaters. Equations B.5-6 show the energy balance equation for both the fresh food and freezer compartment.

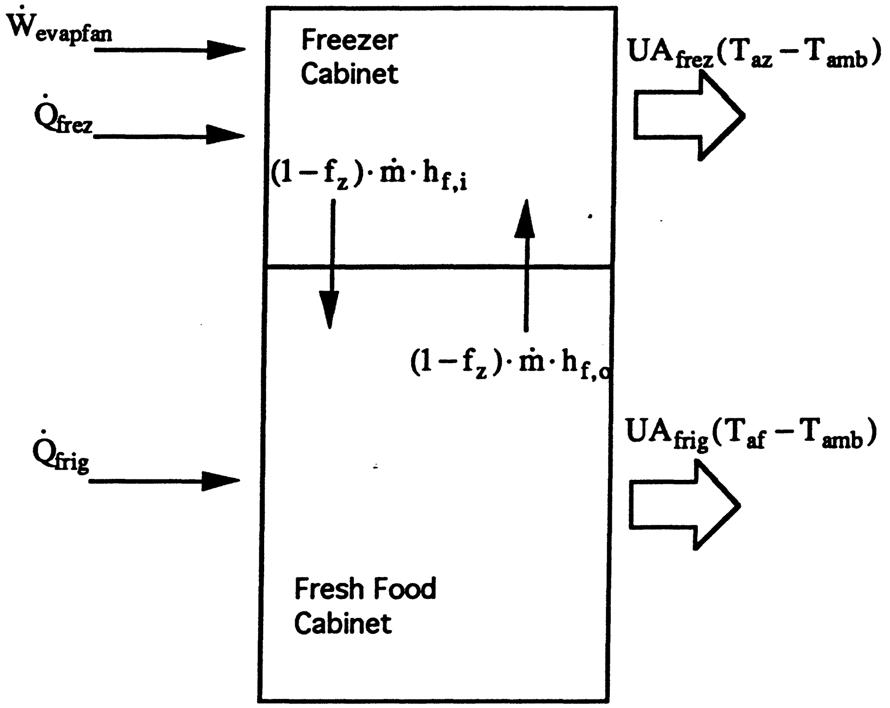

Figure B.3 Control volume for UA_{frig} and UA_{frez} estimation of Whirlpool refrigerator

$$\dot{Q}_{frez}+\dot{W}_{evapfan}+(1-f_z)\cdot\dot{m}_{air}\cdot h_{f,o}=UA_{frez}\cdot(T_{az}-T_{amb})+(1-f_z)\cdot\dot{m}_{air}\cdot h_{f,i} \tag{B.5}$$

$$\dot{Q}_{frig}+(1-f_z)\cdot\dot{m}_{air}\cdot h_{a,i}=UA_{frig}\cdot(T_{af}-T_{amb})+(1-f_z)\cdot\dot{m}_{air}\cdot h_{a,o} \tag{B.6}$$

The resulting optimization resulted in minimizing the error in the two heater loads at a UA_{frez} of 0.502 W/°F and a UA_{frig} of 0.855 W/°F. Figure B.4 shows the scatter in the two heater loads that produced the optimum UA values.

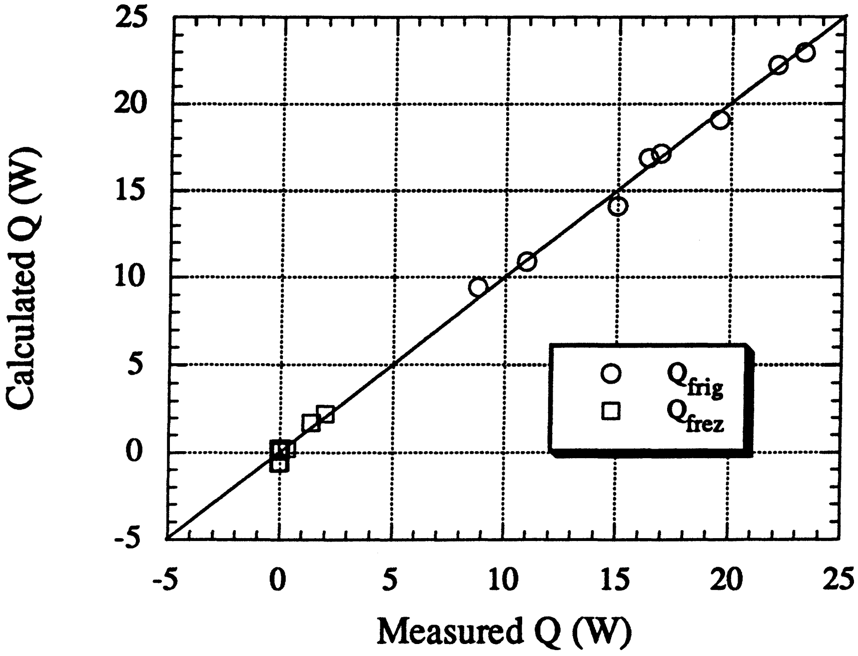

Figure B.4 Whirlpool UA_{frez} and UA_{frig} parameter estimation

Table B.2 Comparison of UA_{frez} and UA_{frig} for Whirlpool refrigerator

	Spring 1994	Fall 1995
UA_{frez}	0.508	0.502
UA_{frig}	0.846	0.855

Table B.2 shows the comparison of the two UA values with those estimated during the spring of 1994. As can be seen, the estimated UA values only changed by 1% since they were last estimated. The difference between the Spring 1994 and Fall 1995 lie within the range of pressure and temperature uncertainty error.

B.2 Side-by-side Amana refrigerator

B.2.1 Split-Air fraction and evaporator volumetric flow rate

For the side-by-side Amana refrigerator, the split-air fraction and evaporator volumetric flow rate could not be estimated the same way as for the Whirlpool due to the fact that the inlet freezer and inlet fresh food air do not mix before they enter the inlet of the evaporator. Another control volume analysis had to be taken for the Amana refrigerator which was different from the Whirlpool model. Figure B.5 shows a diagram of control volume used in the Amana. The two freezer and fresh food air streams are thought to be separate air streams with the split-air fraction determining what area percentage of the evaporator each saw. Considering the control volume in this respect, the following equations from B.7 - B.13 are then used to solve for f_z and $\dot{V}_{evap}$.

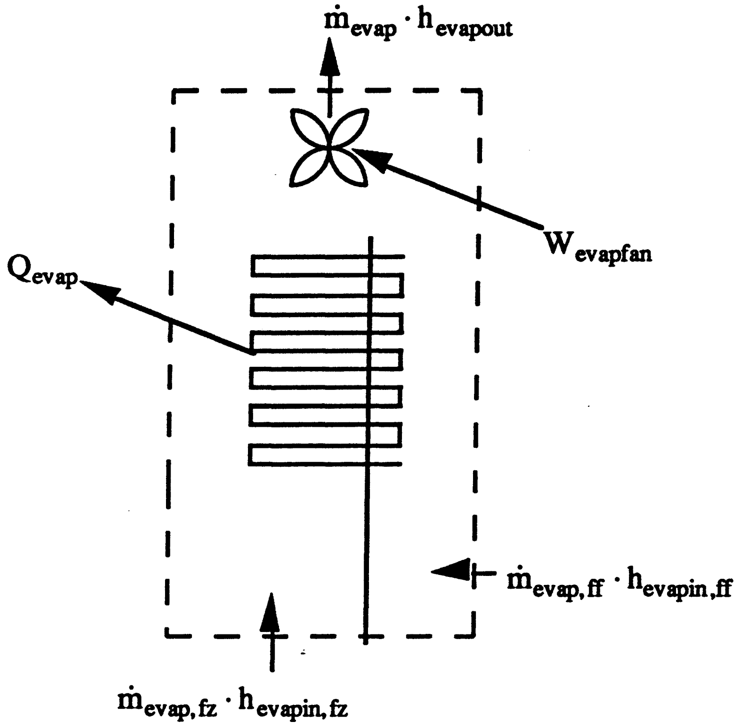

Figure B.5 Evaporator control volume for Amana refrigerator

$$\dot{m}_{evap,fz} \cdot h_{evapin,fz} + \dot{m}_{evap,ff} \cdot h_{evapin,ff} - Q_{evap} + W_{evapfan} = \dot{m}_{evap} \cdot h_{evapout} \tag{B.7}$$

$$\dot{Q}_{evap} = \dot{Q}_{frez} + \dot{Q}_{frig} + UA_{frez}(T_{amb} - T_{az}) + UA_{frig}(T_{amb} - T_{af}) + \dot{W}_{evapfan} \tag{B.8}$$

$$\dot{m}_{evap,fz} = \frac{\dot{V}_{evap,fz} \cdot 60}{\upsilon(T_{az}, P_{atm})} \tag{B.9}$$

$$\dot{m}_{evap,ff} = \frac{\dot{V}_{evap,ff} \cdot 60}{\upsilon(T_{af}, P_{atm})} \tag{B.10}$$

$$\dot{m}_{evap,fz} + \dot{m}_{evap,ff} = \dot{m}_{evap} \tag{B.11}$$

$$\frac{f_z}{(1-f_z)} = \frac{\dot{V}_{evap,fz}}{\dot{V}_{evap,ff}} \tag{B.12}$$

$$\dot{V}_{evap} = \frac{w \cdot \upsilon(T_{evapout}, P_{atm})}{60} \tag{B.13}$$

Notice how equation B.8 solves for the evaporator load based on how much heat load the evaporator must remove. This equation requires the knowledge of the two cabinet conductance parameters which are estimated by a reverse heat leak test which is described in the next section. The reverse heat leak test used to estimate the two cabinet conductances, however, does require the knowledge of the split-air fraction and the volumetric flow rate. Therefore both optimization programs are dependent upon one another and need to be reiterated until the error is minimized in both procedures. This dependence between the reverse heat leak test for estimating the cabinet conductances and the steady-state test to estimate the split-air and volumetric flow rate was also seen in the Whirlpool refrigerator explained earlier.

For estimating the split-air fraction and the volumetric flow rate, the steady-state data was solved such that the error in the measured and calculated evaporator fan outlet temperature was minimized. Initial results with steady-state data taken from the four ambient temperatures 60 °F, 75 °F, 90 °F, and 100 °F showed a large error which could be attributed to frost formation at the first two ambient temperatures. In order to get an accurate prediction of the split-air and volumetric flow rate, only the 90 and 100 °F ambient temperatures were used. Since it is estimated that our thermocouples are accurate to about 0.5 °F, Figure B.6 shows a valley from where the optimum f_z and $\dot{V}_{evap}$ could exist. Optimizing for the minimum error produced an estimation for f_z of 0.82 ± 0.2 and $\dot{V}_{evap}$ of 44.5 ± 1 cfm with a 95% confidence interval on the evaporator fan outlet temperature of 0.38 °F. Figure B.7 shows the error in the measured and calculated evaporator fan outlet temperature for the f_z and $\dot{V}_{evap}$ values of 0.82 ± 0.2 and 44.5 ± 1 cfm respectively.

B.2.2 Side-by-side Amana cabinet conductances

The UA of the freezer cabinet and fresh food cabinet are two of the parameters needed in order to run the steady-state refrigerator simulation model. Again just like the Whirlpool refrigerator, a reverse heat leak test is performed where both the fresh food and freezer compartment are heated to approximately the same temperature in order to eliminate the effects of the $UA_{mullion}$. The equations used for the side-by-side Amana refrigerator are the same as those used in the Whirlpool model shown as equation B.5-B.6. Figure B.8 shows a diagram of the control volume used for the Amana refrigerator.

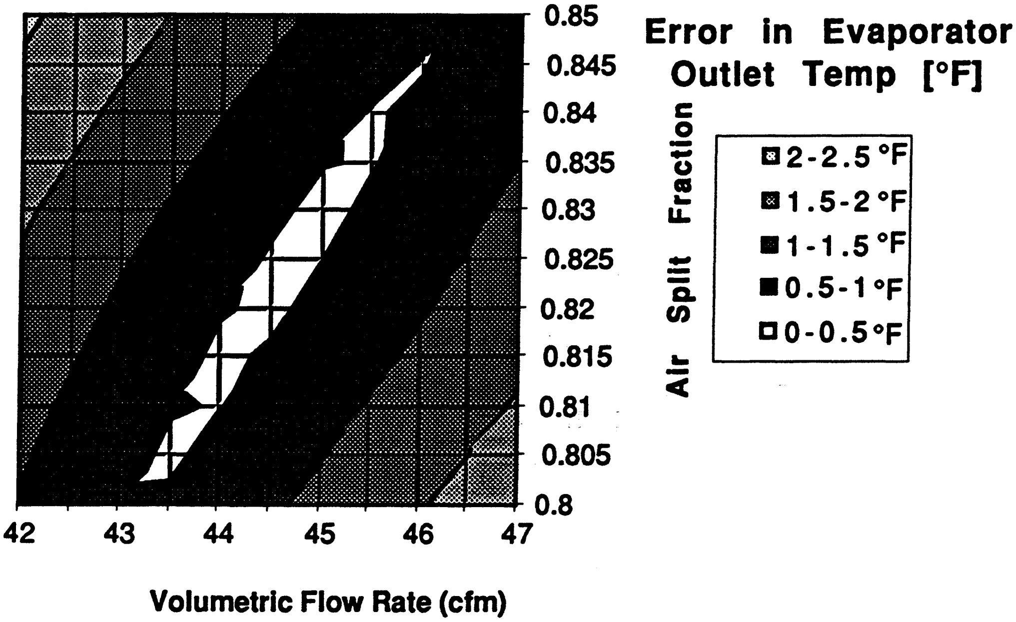

Figure B.6 Amana evaporator volumetric flow and split-air minimum

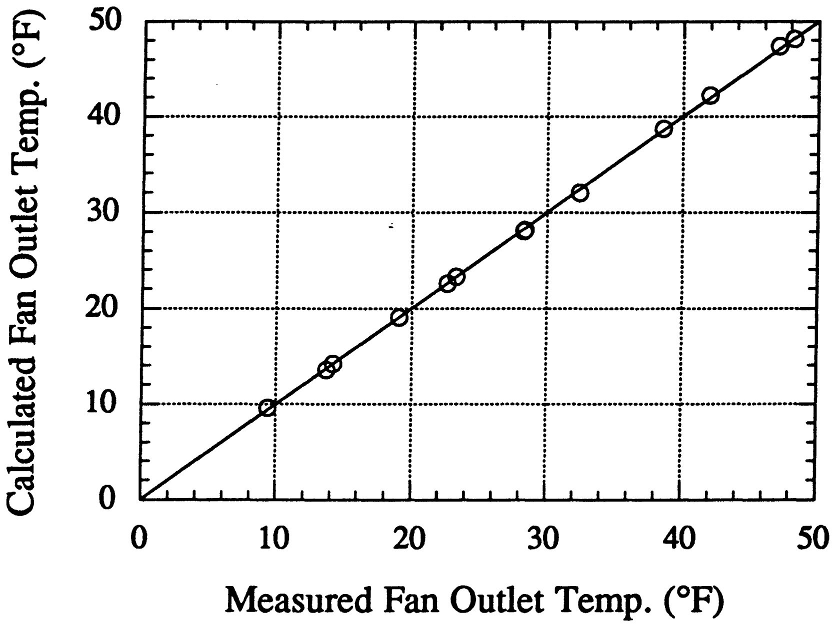

Figure B.7 Amana evaporator volumetric flow and split-air parameter estimation

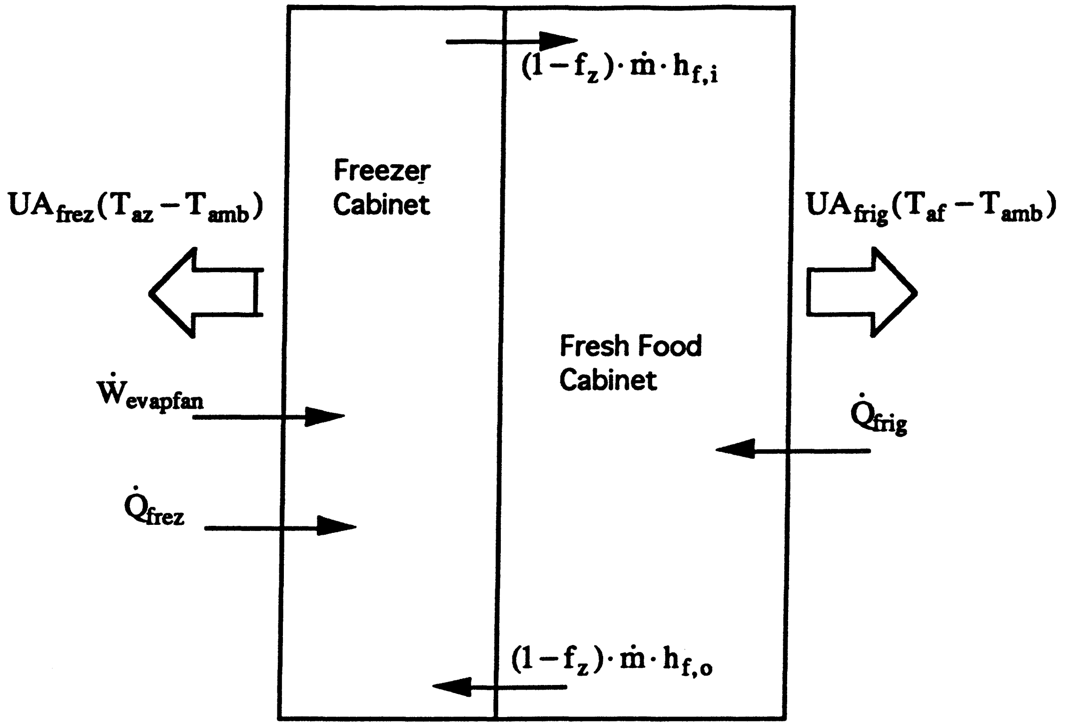

Figure B.8 Control volume for cabinet conductances on Amana refrigerator

B.2.3 Data sampling

In performing an energy balance around the fresh food and freezer cabinet, the amount of power dissipated by the heaters at steady-state must be known. Currently, the heaters in the fresh food and freezer cabinets are connected to an Omega microprocessor controller where one thermocouple is used by the controller to measure temperature. The controller currently employs a PI compensator to control the cabinet temperatures by switching the heater power ON/OFF as described in Appendix N. The length of the ON/OFF time can be controlled by the controller parameters along with the dead band and the integral time. Initially at steady state, large scatter in the measured input power was seen due to limitations of the watt transducer measuring the power. Realistically, the watt meter is designed to measure a continuous power source, however, the PI controller feeds the heaters an ON/OFF signal which is suppose to approximate a constant power. In order to get a confident average of the heater powers, the heater powers had to be sampled at the fastest rate of five seconds for at least one hour. Since it was only the heater powers that fluctuated at steady state and not the temperatures, all other temperatures were sampled every one minute for at least one hour.

B.2.4 Results

Together there were 6 data points used in the parameter estimation of the Amana cabinet conductances. All data points used were achieved by having a very cold ambient temperature of 50 °F and 55 °F and cabinet temperatures of 90 °F, 95 °F, and 100 °F. This resulted in a maximum and minimum ΔT of 50 °F and 35 °F respectively between the cabinet temperature and the ambient temperature. The resulting optimization resulted in a UA_{frez} value of 0.879 W/°F and a UA_{frig} value of 0.800 W/°F. Figure B.9 shows a plot of the scatter in the two heater loads that produced the optimum values. The 2 W scatter in the data may be due to error in the thermocouple wire itself.

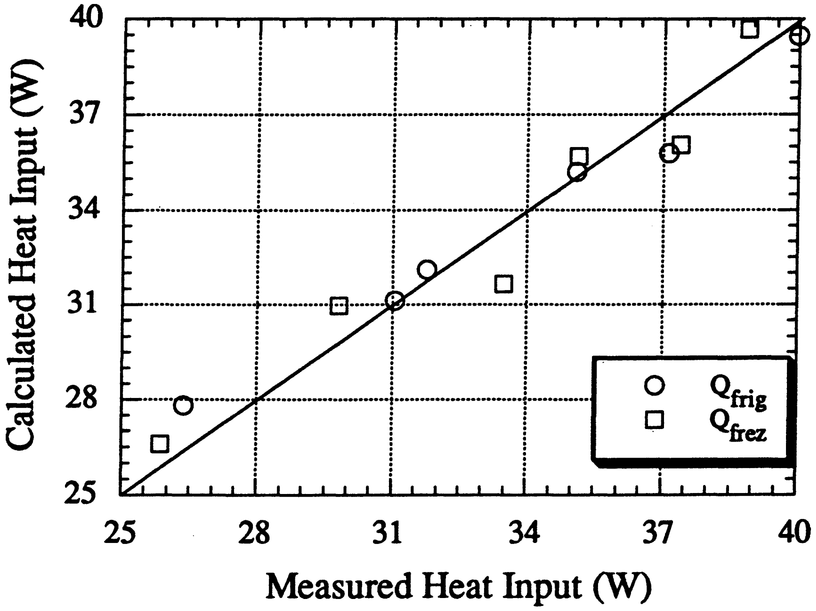

Figure B.9 Side-by-side Amana cabinet conductances parameter estimation

Appendix C

Condenser Parameter Estimations

C.1 Whirlpool refrigerator

C.1.1 Volumetric flow rate

This Appendix explains the estimation of the volumetric air flow rate through the condenser of the experimental refrigerator. The air flow rate through the condenser was estimated from an energy balance across the condenser, compressor, and condenser fan. Figure C.1 shows where temperature measurements were made over the bottom of the refrigerator. A cardboard divider was placed at the front of the refrigerator, and insulation was placed between the cracks to prevent the occurrence of recirculation of the air.

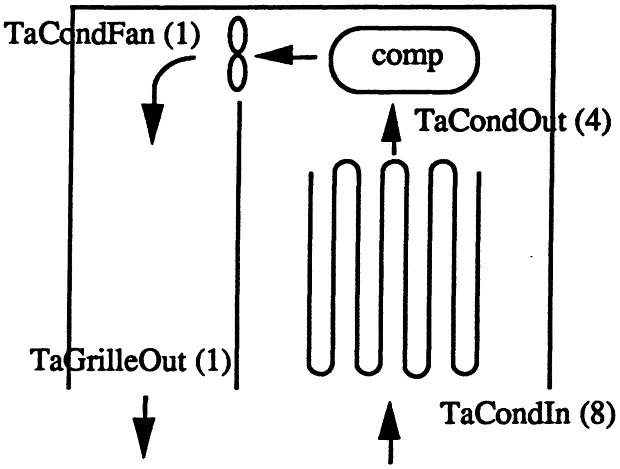

Figure C.1 Temperature readings over bottom of refrigerator

Equations C.1 through C.4 show the equations used to calculate the volumetric flow rate across the condenser using an energy balance method.

$$\dot{Q}_{cond} = \dot{m}_r \cdot (h_1 - h_3) \tag{C.1}$$

$$\dot{Q}_{comp} = \dot{m}_r \cdot (h_1 - h_{11}) \tag{C.2}$$

$$\dot{Q}_{cond} + \dot{Q}_{comp} - (-W_{cond\,fan}) = \dot{m}_{air,c} \cdot C_{p,air}(T_{aCondFan} - T_{aCondIn}) \tag{C.3}$$

$$\dot{V}_{cond} = \frac{\dot{m}_{air,c} \cdot \upsilon_{air,c}}{60} \tag{C.4}$$

The heat transfer from the compressor and the condenser was determined from a refrigerant-side energy balance. The refrigerant mass flow used in these calculations came from a refrigerant-side energy balance across the evaporator where the total heat load of the evaporator was known since cabinet conductances were estimated from reverse heat leak tests (see Appendix B). From the four equations, the estimated parameter $\dot{V}_{cond}$ minimized the error between the measured and predicted condenser heat load. The estimation resulted in an average volumetric flow rate of 105 cfm. Figure C.2 shows the scatter in the calculated and measured condenser heat load, suggesting that the variation in air flow rate is less than ±2%.

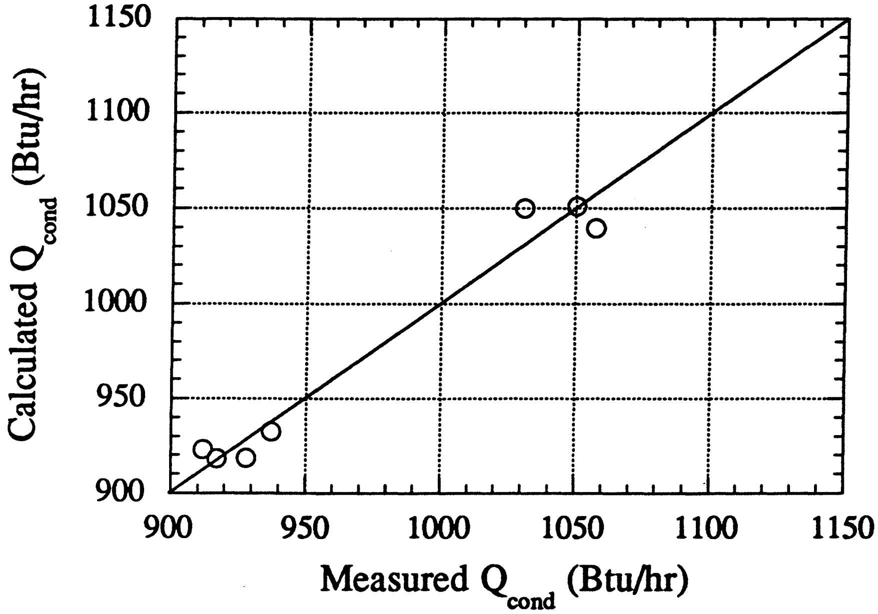

Figure C.2 Whirlpool condenser volumetric flow rate estimation

C.1.2 Recirculation fraction

The recirculation fraction is defined as the amount of condenser exit air that re-enters at the condenser inlet. Most of the recirculation occurs at the front grille of the refrigerator since there are no dividers or deflectors present to divert the exiting air. The temperature at the grille inlet cannot be used as the condenser inlet temperature since it is known that some air enters from the side of the refrigerator at a lower temperature than the grille inlet. To alleviate the problem, a new effective inlet condenser air temperature is calculated based on the known volumetric flow rate of air over the condenser which was just previously estimated. Essentially, equations C.1-4 were used above to estimate the volumetric flow rate, based on the assumption that all air entering the condenser area came originally from the room at ambient temperature. Now we solve for the condenser inlet temperature when the cardboard divider was removed and recirculation does occur, using data from a thermocouple array located at the grille inlet. This gives an effective condenser air inlet temperature which is then used to calculate the recirculation fraction shown in equation C.5.

$$\frac{h_{\text{GrilleIn}}}{\upsilon_{\text{GrilleIn}}} = f_{\text{recir}} * \frac{h_{\text{GrilleOut}}}{\upsilon_{\text{GrilleOut}}} + (1 - f_{\text{recir}}) * \frac{h_{\text{amb}}}{\upsilon_{\text{amb}}} \qquad \text{(C.5)}$$

The f_{recir} parameter was estimated by minimizing the error between the measured and calculated ambient temperature, (an arbitrary choice; the same result would be obtained from comparing the condenser inlet temperature). The best estimate of f_{recir} was found to be 0.22 and is shown in Figure C.3 as the solid line. The recirculation fraction calculated for each of the data points are also plotted in Figure C.3. The scatter may reflect random error in the thermocouples; any bias errors was eliminated during calibration process conducted in a constant-temperature bath.

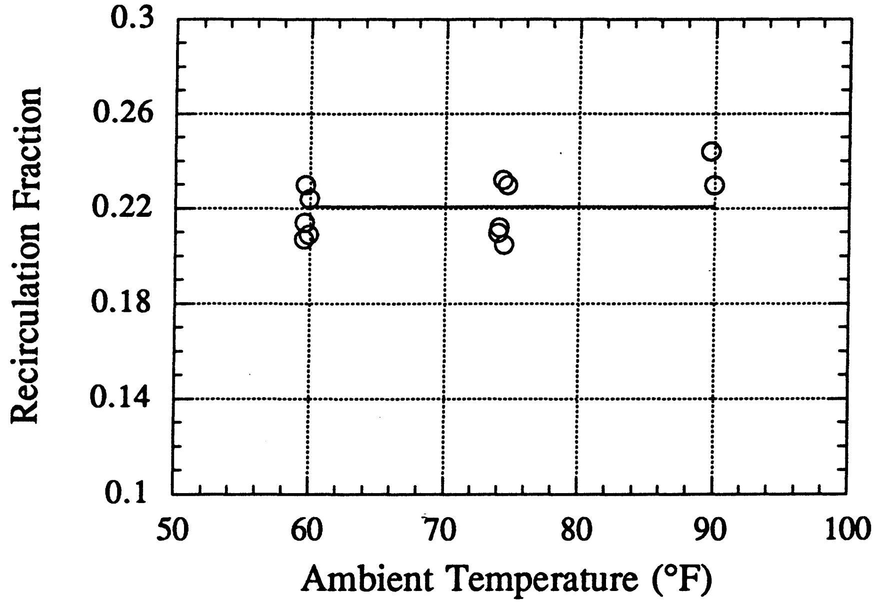

Figure C.3 Whirlpool recirculation fraction estimation

C.1.3 Condenser air-side heat transfer coefficient

Another parameter necessary for a steady-state refrigerator model is the condenser air-side heat transfer coefficient, $h_{\text{air cond}}$. The total resistance from the refrigerant temperature to the air temperature consists of a refrigerant resistance, a tube resistance, and an air resistance. The air resistance is assumed constant while the refrigerant resistance changes with changing mass flow rate and temperature. The resistance of the tubing is assumed to be negligible. Figure C.4 shows a drawing of the actual condenser used in the analysis. In modeling the refrigerator condenser, there are three zones where the refrigerant passes from a superheated inlet to a two-phase region and then finally to a subcooled state until the exit. For the model, it is assumed that a fraction of the inlet air stream passes through each of the three zones and then a final mixing is seen at the condenser fan. Figure C.5 shows a detailed configuration of the condenser modeling with respect to the three zones encountered.

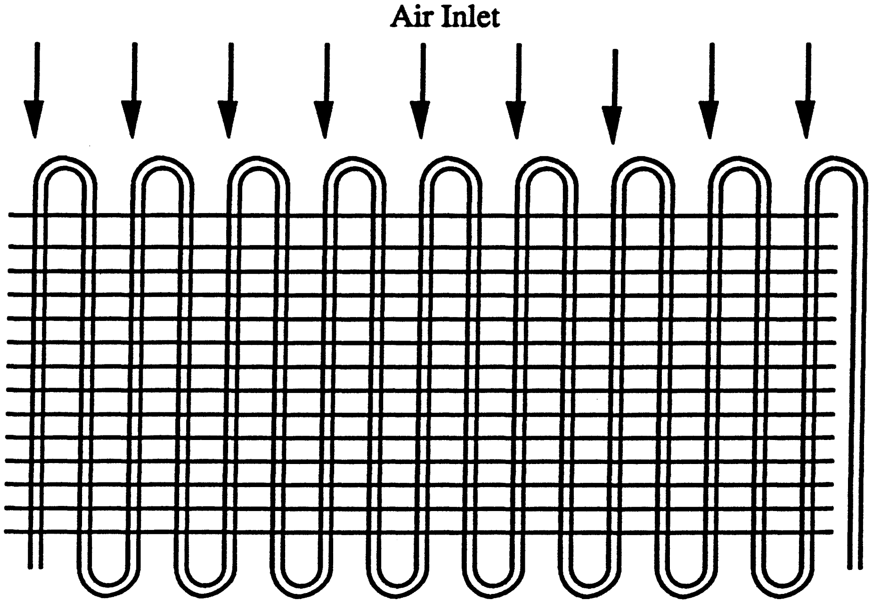

Figure C.4 Actual condenser configuration

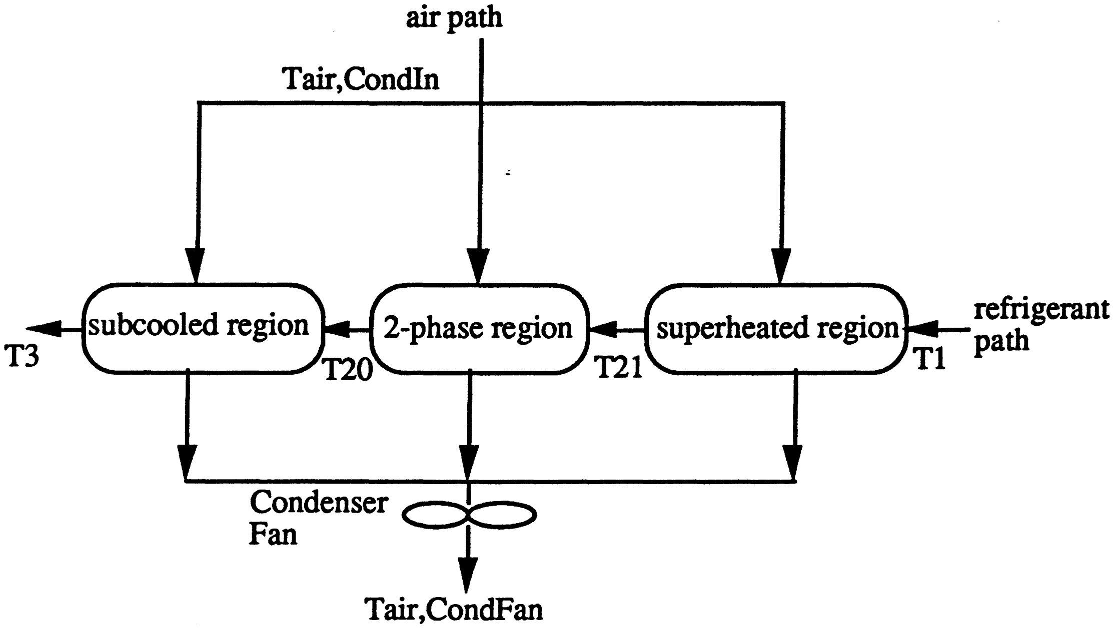

Figure C.5 Condenser model configuration

For the estimation of the air side heat transfer coefficient, refrigerant side energy balances along with effectiveness-NTU rate equations are used in each of the three zones in order to characterize its heat transfer. Since the heat transfer equations for the rate equation will be written from the refrigerant to the air temperature, it is necessary to write the overall heat transfer coefficient for each of the three zones which considers only air side heat transfer coefficient and the refrigerant side heat transfer coefficient. The resistance due to the wall tubing and the resistance due to the wire to tube contact is neglected. The conductance equations for the three zones can then be written as shown in equations C.6-C.8.

Superheated zone:

$$\frac{1}{U_{\text{cond sup}}}=\frac{1}{h_{\text{air cond}}}+\frac{\alpha_{\text{cond}}}{h_{\text{ref sup}}} \tag{C.6}$$

Two-phase zone:

$$\frac{1}{U_{\text{cond 2p}}}=\frac{1}{h_{\text{air cond}}}+\frac{\alpha_{\text{cond}}}{h_{\text{ref 2p}}} \tag{C.7}$$

Subcooled zone:

$$\frac{1}{U_{\text{cond sub}}}=\frac{1}{h_{\text{air cond}}}+\frac{\alpha_{\text{cond}}}{h_{\text{ref sub}}} \tag{C.8}$$

Alpha represents the outer to inner area ratio since the results are based on the outer area. Refrigerant-side heat transfer coefficient for the single phase zones was calculated using the Gnielinski correlation (Incropera and DeWitt, 1990) while the refrigerant-side heat transfer coefficient for the two-phase zone was calculated for the correlation developed by Dobson and Chato (1994). The heat transfer equations representing the refrigerant side energy balance and the rate equations for each zone are then shown in equation C.9-C.22.

Superheated zone:

$$Q_{\text{cond,sup}}=w\cdot(h_0-h_{21}) \tag{C.9}$$

$$Q_{\text{cond,sup}}=\varepsilon_{\text{cond,sup}}\cdot C_{\text{min,cond,sup}}\cdot f_{\text{cond,sup}}\cdot\left(T_0-T_{\text{air,condin}}\right) \tag{C.10}$$

$$\varepsilon_{\text{cond,sup}}=f\left(U_{\text{cond,sup}},A_{\text{cond,sup}},C_{\text{min,cond,sup}},C_{\text{max,cond,sup}}\right) \tag{C.11}$$

$$f_{\text{cond,sup}}=\frac{A_{\text{cond,sup}}}{A_{\text{cond}}} \tag{C.12}$$

Two-phase zone:

$$Q_{cond,2p} = w \cdot (h_{21} - h_{20}) \tag{C.13}$$

$$Q_{cond,2p} = \varepsilon_{cond,2p} \cdot C_{cond,air} \cdot f_{cond,2p} \cdot (T_{20} - T_{air,condin}) \tag{C.14}$$

$$\varepsilon_{cond,2p} = f(U_{cond,2p}, A_{cond,2p}, C_{cond,air}) \tag{C.15}$$

$$f_{cond,2p} = \frac{A_{cond,2p}}{A_{cond}} \tag{C.16}$$

Subcooled zone:

$$Q_{cond,sub} = w \cdot (h_{20} - h_3) \tag{C.17}$$

$$Q_{cond,sub} = \varepsilon_{cond,sub} \cdot C_{min,cond,sub} \cdot f_{cond,sub} \cdot (T_{20} - T_{air,condin}) \tag{C.18}$$

$$\varepsilon_{cond,sub} = f(U_{cond,sub}, A_{cond,sub}, C_{min,cond,sub}, C_{max,cond,sub}) \tag{C.19}$$

$$f_{cond,sub} = \frac{A_{cond,sub}}{A_{cond}} \tag{C.20}$$

System:

$$\dot{Q}_{cond} = \dot{Q}_{cond\ sup} + \dot{Q}_{cond\ 2p} + \dot{Q}_{cond\ sub} \tag{C.21}$$

$$A_{cond} = A_{cond\ sup} + A_{cond\ 2p} + A_{cond\ sub} \tag{C.22}$$

The effectiveness calculations used in the above equations are explained by Admiraal and Bullard (1995). A parallel-counterflow with mixed shell fluid effectiveness correlation was used for the single phase regions. The volumetric air flow rate was fixed at 105 cfm which was explained in Section C.1.1, and the refrigerant mass flow rate was calculated from the energy balance over the evaporator where the cooling capacity of the evaporator is calculated from estimated values of UA for both the freezer and fresh food compartments. The refrigerant exiting the condenser must be subcooled in order to determine the mass flow rate since the enthalpy at the capillary tube inlet must be known. The experimental refrigerator was only able to achieve subcooled condenser exit at unusually warm cabinet temperatures and cool ambient temperatures.

The air side heat transfer coefficient was estimated by solving the seventeen equations and minimizing the total squared error in the calculated and measured condenser heat load. The optimized value for the air side heat transfer coefficient was found to be 4.893 Btu/hr-ft^2-$^\circ$F . This produced a 95% confidence interval on the calculated condenser heat load of 72.4 Btu/hr, or about 7% of the average heat load. Figure C.6 shows the scatter in the calculated condenser heat load to the measured heat load.

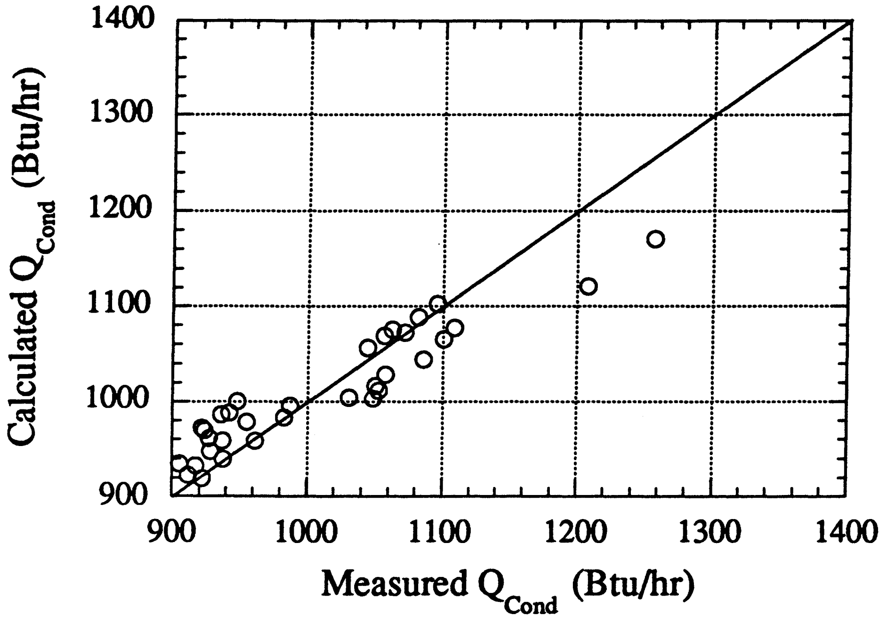

Figure C.6 Whirlpool air-side heat transfer estimation

A total of 33 data points were used in the estimation of the condenser air-side heat transfer coefficient. All the data points were subcooled, which was required for the mass flow rate to be determined. The ambient temperature for the 33 data points ranged from 60 °F to 90 °F.

A good test to see how the parameter estimation will affect the RFSIM model is to see how well the parameters are able to predict the amount of subcooling. Figure C.7 shows what effect the condenser air-side heat transfer coefficient and $\dot{V}_{cond}$ parameter estimations have on the measured and calculated subcooling. The graph shows that at sufficiently high subcooling, the estimated parameters give a predicted subcooling that is closely related to the actual amount of subcooling. At low degrees of subcooling, the parameters appear to give a false estimation of the amount of subcooling. The worst case shown was a prediction of a quality exit at the highest degree of subcooling of 10 °F. It is also important to note that the compressor map equations were used to calculate the mass flow rate and errors in the mass flow can cause a drastic change in the prediction.

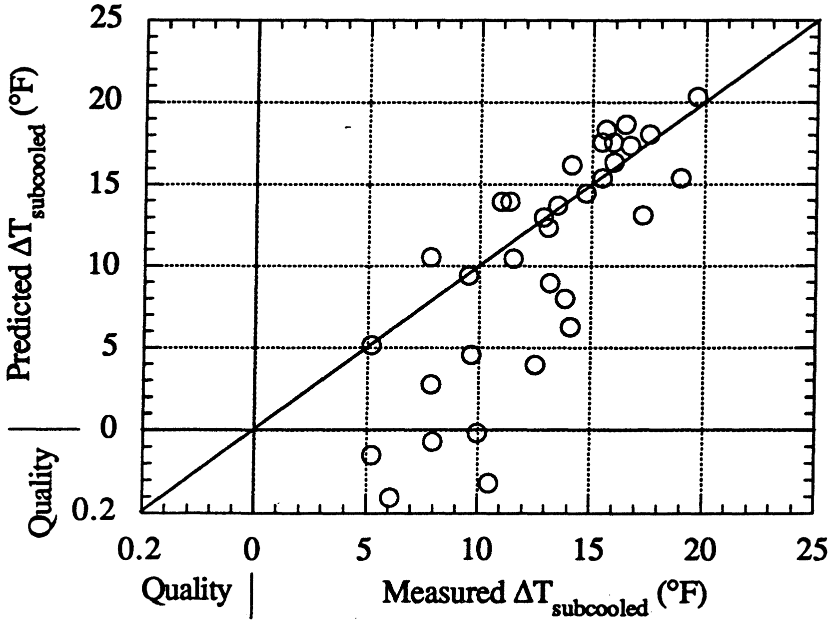

Figure C.7 Whirlpool model predicting subcooling

C.1.4 Comparison with previous results

Earlier parameter estimation for this refrigerator were previously performed by Krause and Bullard (1996). A comparison of the parameter estimation with those performed a year ago are shown in Table C.1.

Table C.1 Comparison of condenser parameter estimations

	Spring 1994	Fall 1995
Condenser volumetric flow rate	188 cfm	105 cfm
Recirculation fraction	0.305	0.22
Condenser air-side heat transfer coefficient	4.90 Btu/hr-ft^2-°F	4.893 Btu/hr-ft^2-°F

Differences between the volumetric flow rate can be attributed to Krause performing a different experiment to obtain his data. Krause inserted a large heater in the condenser compartment and took data with the fan blowing to get his estimate of the volumetric flow rate. In this report the volumetric flow rate was calculated by equating air side energy balances across the condenser for data points where the entire refrigerator was running. Krause reported an estimated measurement uncertainty of 35 cfm which shows that he encountered large inaccuracy in his experiment. A large inconsistency also appears to occur between the present estimate of the recirculation fraction (22%) and that obtained one year ago from another data set (30%). It was concluded that possibly the back panel of the refrigerator was not sealed exactly the same way for the two cases. Having extra air leak out through the back of the refrigerator will cause a slight decrease in the recirculation fraction which is observed between the two data sets. For the condenser air side heat transfer coefficient, the data performed a year ago appear to be in good agreement with the 33 data points taken recently.

C.2 Side-by-side Amana refrigerator

C.2.1 Volumetric flow rate

For the Amana refrigerator, the volumetric flow rate was estimated by equating refrigerant and air-side energy balances across the condenser, compressor, and condenser fan as was done for the Whirlpool refrigerator. The refrigerant mass flow rate was not measured but calculated from cabinet heat loads, which in turn were obtained from power measurements and reverse heat leak tests. Appendix A gave a detailed description of where the air thermocouples were placed throughout the condenser which were used in the parameter estimation. The new design of the Amana is made such that there is no recirculation because the air coming from the front exits at the rear of the system. Equations C.1-C.4 are solved which minimized the error between the measured and calculated condenser fan air temperature.

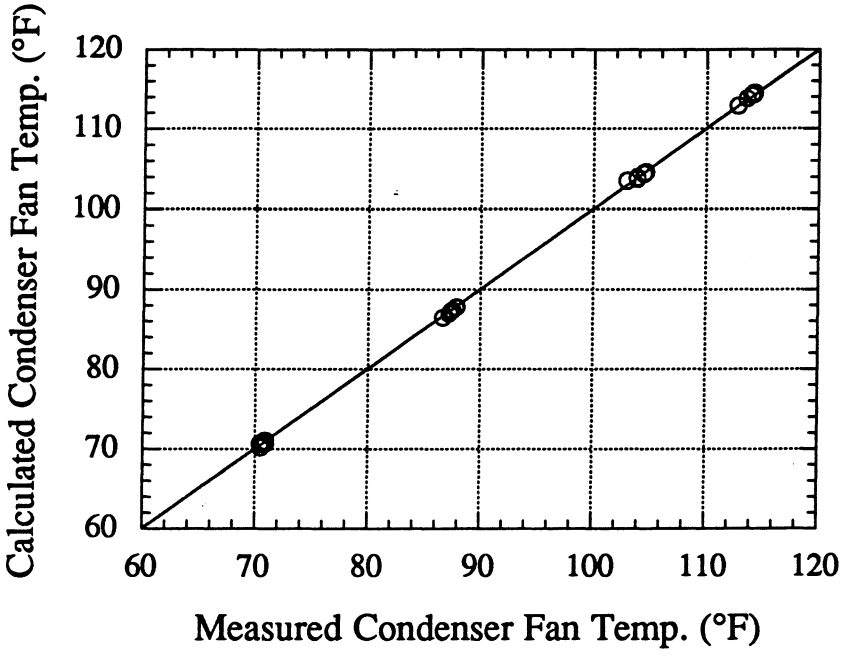

Figure C.8 Amana volumetric flow rate estimation

The optimization program resulted in a volumetric flow rate of 116.370 cfm with a 95% confidence interval on the condenser fan temperature of 0.4 °F. Figure C.8 above shows this 0.4 °F difference in the measured and calculated condenser fan temperature. This result is actually well within the accuracy stated by the manufacturer for the thermocouple wire. Repeated calibration of the thermocouple wire, as described in Appendix O, has helped in reducing the error in the thermocouple wire.

C.2.2 Condenser air-side heat transfer coefficient

The condenser air-side heat transfer coefficient for the current Amana refrigerator was estimated exactly the same as the Whirlpool. There were no differences in the way that both condensers were modeled so the approach as shown in Figure C.5 was used where there are three zones being considered. Equations C.6-C.22 were used in the estimation process where the air-side heat transfer coefficient was optimized by minimizing the error in the calculated and measured condenser load. By calculating the error in the measured and calculated condenser heat load based on a heat transfer rate method, both the air-side heat transfer coefficient and volumetric flow rate could be optimized simultaneously. The results shown in Figure C.9 show a valley in which the minimum error could occur. The graph shows that an air-side heat transfer coefficient of 3.75 Btu/hr-ft^2-°F produces a minimum for a volumetric flow rate value in the range of 113 to 118 cfm. By taking the earlier results of the estimated condenser volumetric flow rate which was calculated by an air-side energy balance across the condenser, the following optimization could be used to solve for just the air-side heat transfer coefficient, estimated to be 3.74 Btu/hr-ft^2-°F. Figure C.10 shows the scatter in the measured and calculated condenser load having a 95% confidence interval of 54 Btu/hr which translate to about a 6% error in the average calculated condenser load.

With the condenser volumetric flow rate estimated at 116.4 cfm and the condenser air-side heat transfer coefficient estimated at 3.74 Btu/hr-ft^2-°F, a more rigorous examination of the simulation model can be performed by seeing how it predicts the exit condition of the condenser. The inlet air and refrigerant conditions are inputted along with air and refrigerant-side heat transfer coefficient for the 24 data points. For the inlet mass flow to the condenser, the compressor map was used. Figure C.11 shows both experimental and predicted condenser outlet conditions. The graph shows that for some of the low subcooled points, a quality exit is predicted.

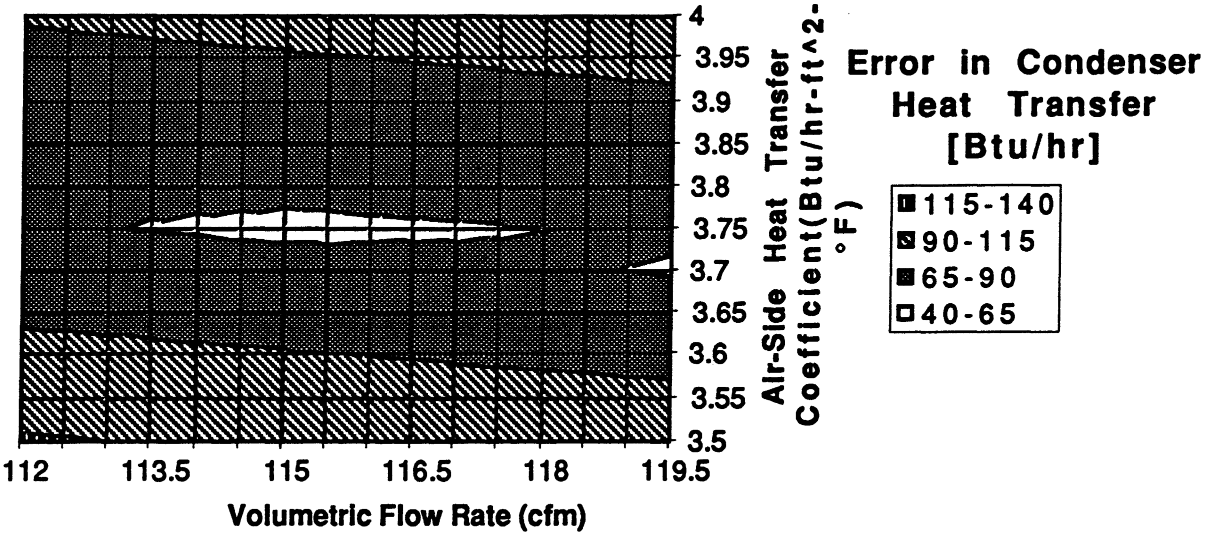

Figure C.9 Minimizing error in condenser heat transfer (Btu/hr)

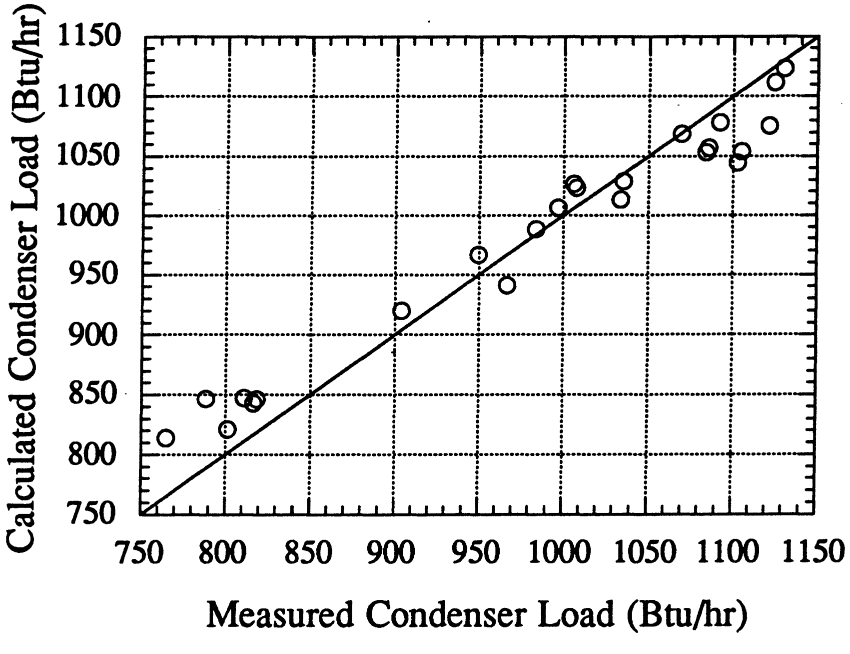

Figure C.10 Amana air-side heat transfer estimation

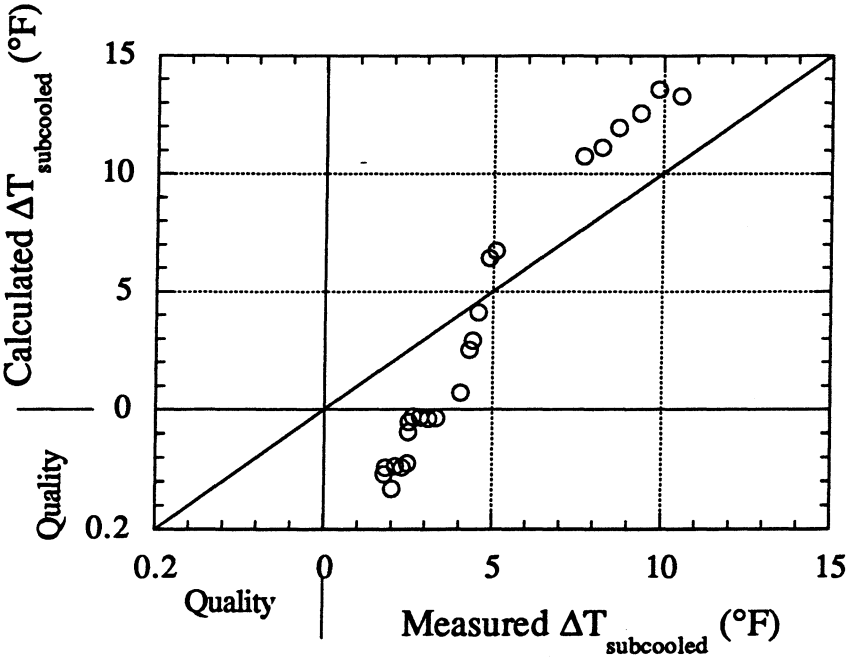

Figure C.11 Amana model predicting subcooling

Appendix D

Evaporator Parameter Estimations

D.1 Whirlpool refrigerator

D.1.1 Evaporator air-side heat transfer coefficient

D.1.1.1 Evaporator modeling

In order to correctly estimate an evaporator air-side heat transfer coefficient, an accurate model of the evaporator system must first be developed. Figure D.1 shows the actual configuration of the evaporator as it sits in the refrigerator. It is important to note that the refrigerant flows downwards over the first half of the evaporator and then it flows upwards over the second half. This means that when the inlet air flows across the evaporator, half of the air will see a counterflow heat exchanger while the other half will see a parallel flow heat exchanger. In modeling this evaporator, it was assumed that the counterflow half of the evaporator would always see a two-phase refrigerant flow while the parallel section of the evaporator would see a two-phase and a superheated zone. Figure D.2 shows a detailed drawing of the evaporator model paths. Together there are three zones where refrigerant side energy balances and an effectiveness-NTU rate equations are solved.

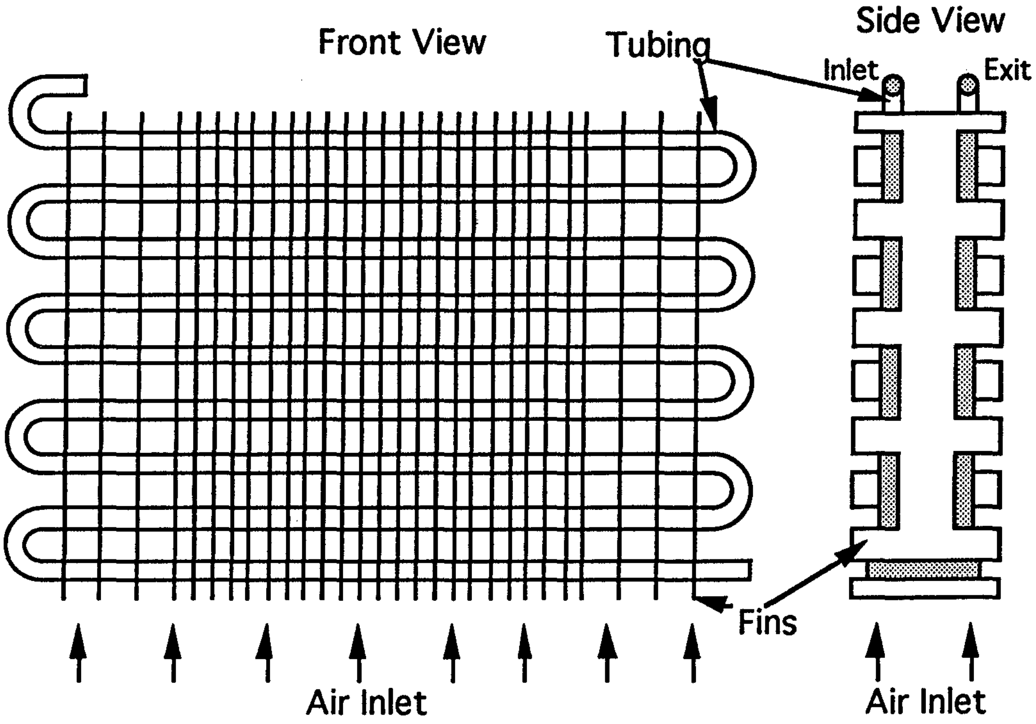

Figure D.1 Whirlpool evaporator geometry

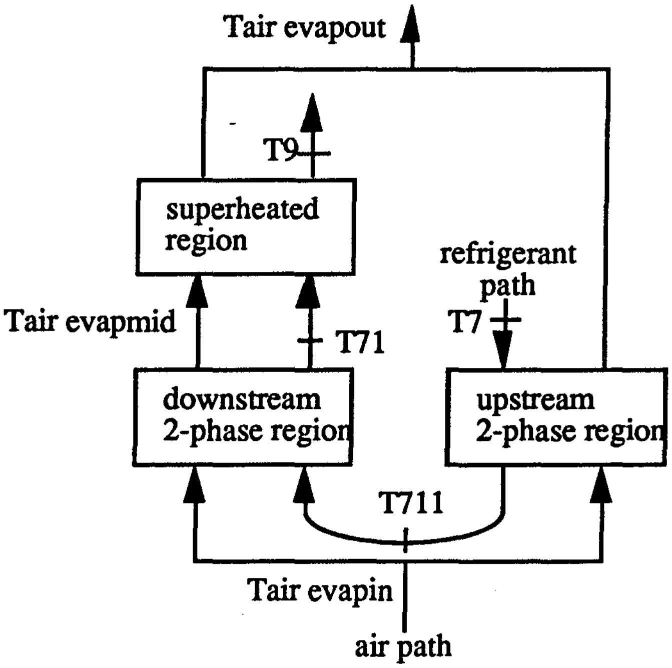

Figure D.2 Model configuration

D.1.1.2 Conductance equations

For the estimate of the air-side heat transfer coefficient, an overall UA for each of the three zones is calculated where only the air-side heat transfer coefficient and the refrigerant-side heat transfer coefficient are considered. The resistance due to the wall and fin-tube contact in the evaporator is considered negligible. Equations D.1 through D.3 show the conductance equations written for the three zones.

Upstream two-phase zone:

$$\frac{1}{U_{2pu}} = \frac{1}{h_{air\ evap}} + \frac{alpha_{evap}}{h_{ref\ 2pu}} \tag{D.1}$$

Downstream two-phase zone:

$$\frac{1}{U_{2pd}} = \frac{1}{h_{air\ evap}} + \frac{alpha_{evap}}{h_{ref\ 2pd}} \tag{D.2}$$

Superheated zone:

$$\frac{1}{U_{sup}} = \frac{1}{h_{air\ evap}} + \frac{alpha_{evap}}{h_{ref\ sup}} \tag{D.3}$$

For the refrigerant-side heat transfer coefficient, the two-phase zone is calculated using the correlation developed by Wattelet and Chato (1994) while the superheated zone uses the Gnielinski correlation (Incropera and DeWitt, 1990). The $alpha_{evap}$ term is the area ratio which represents the ratio of the outer to inner surface area.

D.1.1.3 Refrigerant-side energy balances and effectiveness rate equations

In addition to the conductance equations, refrigerant-side energy balances and effectiveness-NTU rate equations are written for all three zones. Equations D.4-15 show these equations for the evaporator being analyzed.

Upstream two-phase zone:

$$Q_{2pu} = w \cdot \left(h_{711} - h_7\right) \tag{D.4}$$

$$Q_{2pu} = \varepsilon_{2pu} \cdot C_{air} \cdot \left(T_{air,evapin} - T_7\right) \tag{D.5}$$

$$\varepsilon_{2pu} = f(U_{2pu}, A_{2pu}, C_{air}) \tag{D.6}$$

$$C_{air} = \frac{\dot{m}_{air} \cdot Cp_{air}}{2} \tag{D.7}$$

Downstream two-phase zone:

$$Q_{2pd} = w \cdot \left(h_{71} - h_{711}\right) \tag{D.8}$$

$$Q_{2pd} = \varepsilon_{2pd} \cdot C_{air} \cdot \left(T_{air,evapin} - T_{711}\right) \tag{D.9}$$

$$\varepsilon_{2pd} = f(U_{2pd}, A_{2pd}, C_{air}) \tag{D.10}$$

Superheated zone:

$$Q_{sup} = w \cdot \left(h_9 - h_{71}\right) \tag{D.11}$$

$$Q_{sup} = \varepsilon_{sup} \cdot C_{min} \cdot \left(T_{air,evapmid} - T_{71}\right) \tag{D.12}$$

$$\varepsilon_{sup} = f(U_{sup}, A_{sup}, C_{air}, C_{ref}) \tag{D.13}$$

System:

$$Q_{evap} = Q_{2pu} + Q_{2pd} + Q_{sup} \tag{D.14}$$

$$A_{evap} = A_{2pu} + A_{2pd} + A_{sup} \tag{D.15}$$

For the effectiveness-NTU equations, the minimum heat capacity rates must be used between the refrigerant and the air stream. For the two-phase zones, the heat capacity rate for the air is always the minimum when compared to the refrigerant side, therefore the air capacity rate is used in the effectiveness rate equations. For the superheated zone, this is not true and the heat capacity of both the refrigerant and air need to be compared to see which is the minimum. Also for the air heat capacity rate, the mass flow rate is divided by 2 since theoretically half of the air flows over the counterflow configuration and the other half flows over the parallel flow configuration.

D.1.1.4 Results

The estimation of the air side heat transfer coefficient minimized the error between the measured and calculated evaporator heat load. The measured evaporator load is known since both cabinet UA values are known along with the heat inputted from the two compartment heaters. The optimum value of the air side heat transfer coefficient was found to be 1.333 Btu/hr-ft^2-°F. This value produced a 95% confidence interval on the measured evaporator heat load of 87 Btu/hr or about 10% of the total. Figure D.3 shows a graph of the predicted and measured evaporator heat load.

Figure D.3 shows that there is a large scatter in the predicted and measured heat load. In order to see if our evaporator model was valid, the air side heat transfer coefficient was calculated at each data point and then plotted against the amount of superheat. In Figure D.4 there is a noticeable decrease in the air side heat transfer coefficient as the amount of superheat is increased. In total there were four sets of data taken which are separated by the four different symbols to show that this decrease in air side heat transfer coefficient occurs in all four sets. It is possible that frost formation on the evaporator fins could account for some of the decrease in the data. For each ambient temperature tested, the refrigerator was first shut off and the chamber was allowed to reach the set ambient temperature. Any frost on the evaporator fins would melt and the evaporator would start off being frost-free. The refrigerator would then be turned on and the first point would be set which corresponded to the lowest amount of superheat. As data was taken, the amount of superheat that the evaporator saw was increased and the data was repeated for the other ambient temperatures. Therefore, as frost formation increases the air side heat transfer coefficient will decrease which is the effect that is seen in the data. This is due to the fact that the formation of frost causes an increase in the air-side resistance.

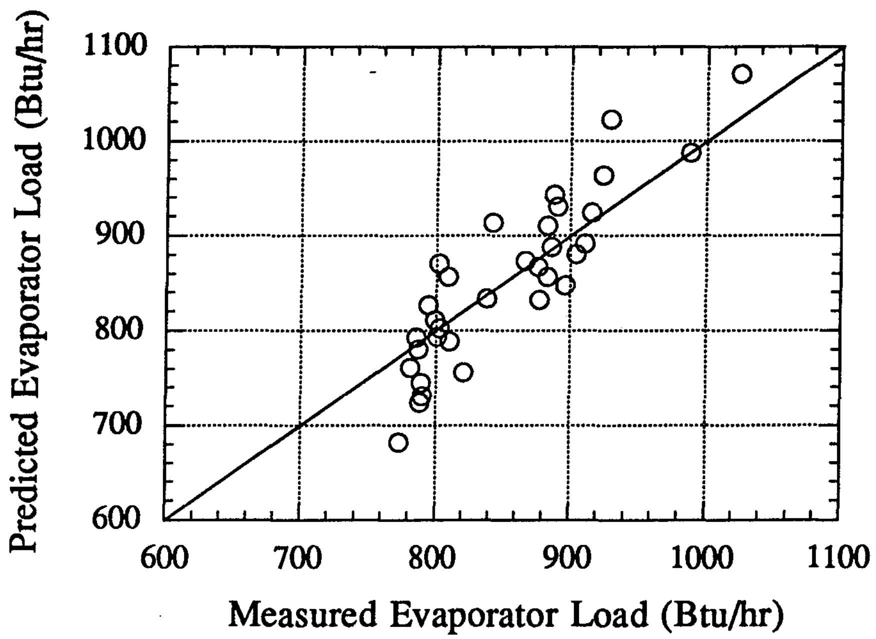

Figure D.3 Whirlpool air-side heat transfer estimation

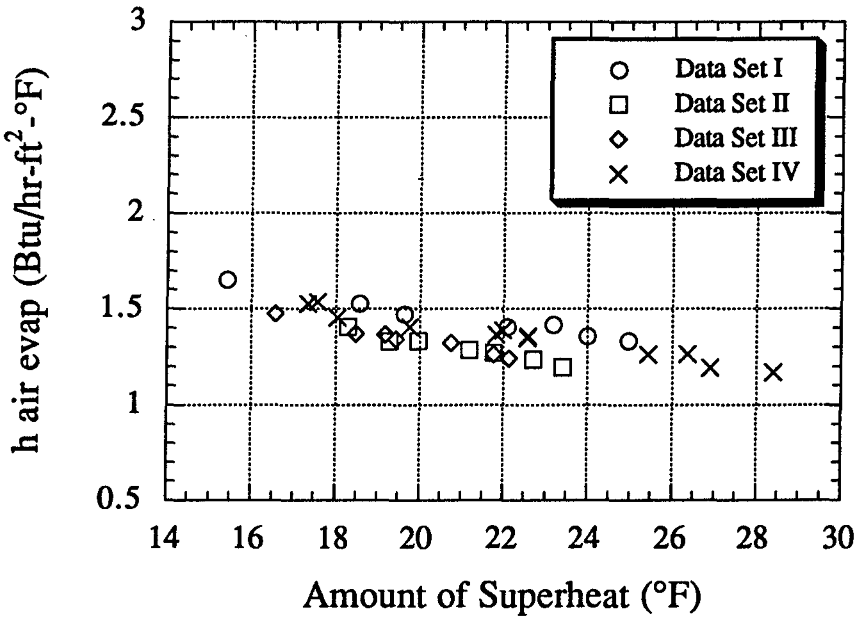

Figure D.4 Whirlpool air-side heat transfer coefficient (mixed inlet air)

To check to see if frost is accountable for the change in the data, the model was run again where a resistance variable that accounts for the frost is placed in the model and solved with a constant air side heat transfer coefficient of 1.60. Although it is known that there should be a slight change in the volumetric flow rate due to frost build-up, it is not quite known how to model this change and therefore the volumetric flow rate was still assumed to be constant. The results of this test showed that the calculated resistance due to frost is too high. Therefore it is possible that the change in the volumetric flow rate is what seriously degrades the air side heat transfer coefficient when frost forms and not the increase in resistance due to the frost. It is also possible that some other type of modeling error may exist.

D.1.1.5 Evaporator model using inlet air as two unmixed air streams

From looking at the evaporator model, it is assumed that the inlet of the evaporator is a mixed temperature of the fresh food and freezer air. The actual refrigerator geometry shows that perhaps this approach of a mixed temperature is invalid. The refrigerator geometry shows that the bulk freezer air flows over the majority of the evaporator while the air from the fresh food appears to flow over just a portion of the evaporator along the two edges. In order to model the refrigerator evaporator as seeing two air streams, a second model is written such that there is a freezer air stream and a fresh food air stream seeing the same refrigerant flow. The split air fraction is then used to divide the total length of the evaporator into a freezer length and a fresh food length. Since the length of each evaporator is known, the number of fins for each evaporator is known also and so the total surface area and the area ratio can be calculated. The assumption is then made that the freezer and fresh food zones do not interact with one another. Essentially, the conductance equations D.1-D.3 are used and equations D.4-D.15 would be re-modified such that the effectiveness-NTU rate equations were written twice to account for both evaporators as shown in equation D.16-D.41. When running the simulation program and considering all the above, Figure D.5 shows the results of the air side heat transfer coefficient at the different amounts of superheat levels.

Upstream two-phase zone:

$$Q_{2pu} = w \cdot \left(h_{711} - h_7\right) \tag{D.16}$$

$$Q_{2pu} = Q_{2pu,frez} + Q_{2pu,ff} \tag{D.17}$$

$$Q_{2pu,frez} = \varepsilon_{2pu,frez} \cdot 0.5 \cdot C_{p,air} \cdot \dot{m}_{frez} \cdot \left(T_{a,evapin,frez} - T_7\right) \tag{D.18}$$

$$\varepsilon_{2pu,frez} = f(U_{2pu}, A_{2pu,frez}, C_{p,air} \cdot \dot{m}_{frez} \cdot 0.5) \tag{D.19}$$

$$A_{2pu,frez} = f_z \cdot A_{2pu} \tag{D.20}$$

$$Q_{2pu,ff} = \varepsilon_{2pu,ff} \cdot 0.5 \cdot C_{p,air} \cdot \dot{m}_{ff} \cdot \left(T_{a,evapin,ff} - T_7\right) \tag{D.21}$$

$$\varepsilon_{2pu,ff} = f(U_{2pu}, A_{2pu,ff}, C_{p,air} \cdot \dot{m}_{ff} \cdot 0.5) \tag{D.22}$$

$$A_{2pu,ff} = (1 - f_z) \cdot A_{2pu} \tag{D.23}$$

Downstream two-phase zone:

$$Q_{2pd} = w \cdot (h_{71} - h_{711}) \tag{D.24}$$

$$Q_{2pd} = Q_{2pd,frez} + Q_{2pd,ff} \tag{D.25}$$

$$Q_{2pd,frez} = \varepsilon_{2pd,frez} \cdot 0.5 \cdot C_{p,air} \cdot \dot{m}_{frez} \cdot \left(T_{a,evapin,frez} - T_{711}\right) \tag{D.26}$$

$$\varepsilon_{2pd,frez} = f(U_{2pd}, A_{2pd,frez}, C_{p,air} \cdot \dot{m}_{frez} \cdot 0.5) \tag{D.27}$$

$$A_{2pd,frez} = f_z \cdot A_{2pd} \tag{D.28}$$

$$Q_{2pd,ff} = \varepsilon_{2pd,ff} \cdot 0.5 \cdot C_{p,air} \cdot \dot{m}_{ff} \cdot \left(T_{a,evapin,ff} - T_7\right) \tag{D.29}$$

$$\varepsilon_{2pd,ff} = f(U_{2pd}, A_{2pd,ff}, C_{p,air} \cdot \dot{m}_{ff} \cdot 0.5) \tag{D.30}$$

$$A_{2pd,ff} = (1 - f_z) \cdot A_{2pd} \tag{D.31}$$

Superheated zone:

$$Q_{sup} = w \cdot (h_9 - h_{71}) \tag{D.32}$$

$$Q_{sup} = Q_{sup,frez} + Q_{sup,ff} \tag{D.33}$$

$$Q_{sup,frez} = \varepsilon_{sup,frez} \cdot C_{min,frez} \cdot \left(T_{a,evapmid,frez} - T_{71}\right) \tag{D.34}$$

$$\varepsilon_{sup,frez} = f(U_{sup}, A_{sup,frez}, C_{min,sup}, C_{max,sup}) \tag{D.35}$$

$$A_{sup,frez} = f_z \cdot A_{sup} \tag{D.36}$$

$$Q_{sup,ff} = \varepsilon_{sup,ff} \cdot C_{min,ff} \cdot \left(T_{a,evapmid,ff} - T_{71}\right) \qquad (D.37)$$

$$\varepsilon_{sup,ff} = f(U_{sup}, A_{sup,ff}, C_{min,ff}, C_{max,ff}) \qquad (D.38)$$

$$A_{sup,ff} = (1 - f_z) \cdot A_{sup} \qquad (D.39)$$

System:

$$Q_{evap} = Q_{2pu} + Q_{2pd} + Q_{sup} \qquad (D.40)$$

$$A_{evap} = A_{2pu} + A_{2pd} + A_{sup} \qquad (D.41)$$

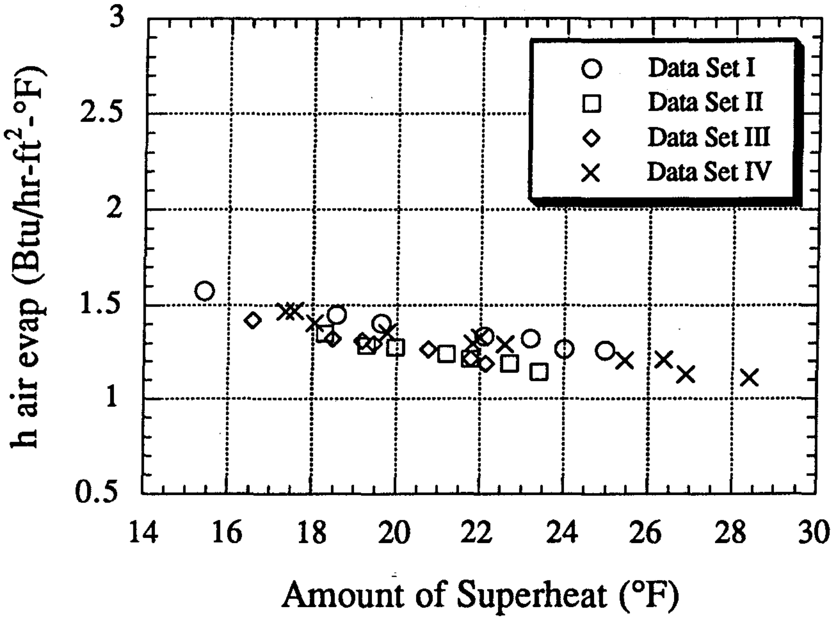

Figure D.5 Whirlpool air-side heat transfer coefficient (freezer & fresh food air streams)

Figure D.5 shows the same result as in Figure D.4 in that the air side heat transfer coefficient decreases with increasing superheat. In fact, the results show almost no change from when an inlet mixed air temperature was considered.

D.1.1.6 Evaporator model with mixed inlet air and fin conduction occurring

A third approach to modeling the evaporator was to assume that the evaporator fins are thick enough to allow heat transfer to occur by conduction along the fin. Appendix G showed us that for the side-by-side Amana evaporator, dryout at high superheat was occurring which attributed to a decline in the estimation of the air-side heat transfer coefficient. Although the same testing was not confirmed on the Whirlpool evaporator, it was shown that adding fin conduction in the Amana evaporator model did make the refrigerant flow predictions better. A rough calculation on the Whirlpool evaporator suggested that the fin efficiency (ignoring contact resistance) is about 0.95. Therefore it is possible for the cold fins in the counterflow half of the evaporator to conduct heat from the warmer superheated (parallel flow) half of the fin in order to approach some average temperature. To implement fin conduction into the evaporator model, the effectiveness-NTU rate equations for each of the three zones were rewritten now using an LMTD method. The equations representing the air to fin surface LMTD and the fin surface to refrigerant LMTD are shown below in Equation D.42 through D.58. For the refrigerant side energy balances, the conduction terms $Q_{sup\rightarrow 2pu}$, $Q_{sup\rightarrow 2pd}$, and $Q_{2pd\rightarrow 2pu}$ are added which represents the amount of heat being conducted from each of the three zones to one another.

Upstream two-phase zone:

$$Q_{2pu} + Q_{sup\rightarrow 2pu} + Q_{2pd\rightarrow 2pu} = w \cdot \left(h_{711} - h_7\right) \tag{D.42}$$

$$Q_{2pu} = h_{air,evap} \cdot A_{2pu} \cdot LMTD_{2pu,Air\rightarrow Surf} \tag{D.43}$$

$$LMTD_{2pu,Air\rightarrow Surf} = \frac{\left(T_{a,evapin} - T_{surf,2pu}\right) - \left(T_{a,evapout,2pu} - T_{surf,2pu}\right)}{\ln\left[\left(T_{a,evapin} - T_{surf,2pu}\right) \Big/ \left(T_{a,evapout,2pu} - T_{surf,2pu}\right)\right]} \tag{D.44}$$

$$Q_{2pu} + Q_{sup\rightarrow 2pu} + Q_{2pd\rightarrow 2pu} = \frac{h_{ref,evap,2pu}}{\alpha_{evap}} \cdot A_{2pu} \cdot LMTD_{2pu,Surf\rightarrow Ref} \tag{D.45}$$

$$LMTD_{2pu,Surf\rightarrow Ref} = \frac{\left(T_{surf,2pu} - T_{711}\right) - \left(T_{surf,2pu} - T_7\right)}{\ln\left[\left(T_{surf,2pu} - T_{711}\right) \Big/ \left(T_{surf,2pu} - T_7\right)\right]} \tag{D.46}$$

Downstream two-phase zone:

$$Q_{2pd} + Q_{sup\rightarrow 2pd} - Q_{2pd\rightarrow 2pu} = w \cdot \left(h_{71} - h_{711}\right) \tag{D.47}$$

$$Q_{2pd} = h_{air,evap} \cdot A_{2pd} \cdot LMTD_{2pd,Air\rightarrow Surf} \tag{D.48}$$

$$\mathrm{LMTD}_{2pd,Air\rightarrow Surf} = \frac{\left(T_{a,evapin} - T_{surf,2pd}\right) - \left(T_{a,evapmid} - T_{surf,2pd}\right)}{\ln\left[\left(T_{a,evapin} - T_{surf,2pd}\right) \middle/ \left(T_{a,evapmid} - T_{surf,2pd}\right)\right]} \quad \text{(D.49)}$$

$$Q_{2pd} + Q_{sup\rightarrow 2pd} - Q_{2pd\rightarrow 2pd} = {}^{-}h_{ref,evap,2pd} \big/ \alpha_{evap} \cdot A_{2pd} \cdot \mathrm{LMTD}_{2pd,Surf\rightarrow Ref}$$

(D.50)

$$\mathrm{LMTD}_{2pd,Surf\rightarrow Ref} = \frac{\left(T_{surf,2pd} - T_{71}\right) - \left(T_{surf,2pd} - T_{711}\right)}{\ln\left[\left(T_{surf,2pd} - T_{71}\right) \middle/ \left(T_{surf,2pd} - T_{711}\right)\right]} \quad \text{(D.51)}$$

Superheated zone:

$$Q_{sup} - Q_{sup\rightarrow 2pu} - Q_{sup\rightarrow 2pd} = w \cdot \left(h_9 - h_{71}\right) \quad \text{(D.52)}$$

$$Q_{sup} = h_{air,evap} \cdot A_{sup} \cdot \mathrm{LMTD}_{sup,Air\rightarrow Surf} \quad \text{(D.53)}$$

$$\mathrm{LMTD}_{sup,Air\rightarrow Surf} = \frac{\left(T_{a,evapmid} - T_{surf,sup}\right) - \left(T_{a,evapout,sup} - T_{surf,sup}\right)}{\ln\left[\left(T_{a,evapmid} - T_{surf,sup}\right) \middle/ \left(T_{a,evapout,sup} - T_{surf,sup}\right)\right]}$$

(D.54)

$$Q_{sup} - Q_{sup\rightarrow 2pu} - Q_{sup\rightarrow 2pd} = h_{ref,evap,sup} \big/ \alpha_{evap} \cdot A_{sup} \cdot \mathrm{LMTD}_{sup,Surf\rightarrow Ref}$$

(D.55)

$$\mathrm{LMTD}_{sup,Surf\rightarrow Ref} = \frac{\left(T_{surf,sup} - T_9\right) - \left(T_{surf,sup} - T_{71}\right)}{\ln\left[\left(T_{surf,sup} - T_9\right) \middle/ \left(T_{surf,sup} - T_{71}\right)\right]} \quad \text{(D.56)}$$

System:

$$Q_{evap} = Q_{2pu} + Q_{2pd} + Q_{sup} \quad \text{(D.57)}$$

$$A_{evap} = A_{2pu} + A_{2pd} + A_{sup} \quad \text{(D.58)}$$

The three heat conduction equations consider heat transfer from the superheat zone to the two two-phase zones, $Q_{sup\rightarrow 2pu}$ and $Q_{sup\rightarrow 2pd}$, and a heat conduction equation considering heat transfer between the two two-phase zones, $Q_{2pd\rightarrow 2pu}$. Since conduction along the fin is considered, the thermal conductivity of the evaporator fin needs to be known. However, it is not actually known if the evaporator fins are made from 100% aluminum or an aluminum alloy. The material considered will dictate the amount of heat conduction that will occur in the fin. It was assumed that the evaporator fins were made of an aluminum alloy. For the conduction equations, the perpendicular area needs to be known between the three zones. Although there is really a distance that exists between the fins, the perpendicular area was calculated considering that all 78 evaporator fins were stacked together and the perpendicular area calculated was based on this assumption. The fin conduction equations are shown below as Equation D.59 through D.61

Conduction Equations:

$$Q_{sup\rightarrow 2pu} = \frac{k_{Al} \cdot A_{\perp,sup\rightarrow 2pu}}{\ell_{sup\rightarrow 2pu}} \tag{D.59}$$

$$Q_{sup\rightarrow 2pd} = \frac{k_{Al} \cdot A_{\perp,sup\rightarrow 2pd}}{\ell_{sup\rightarrow 2pd}} \tag{D.60}$$

$$Q_{2pd\rightarrow 2pu} = \frac{k_{Al} \cdot A_{\perp,2pd\rightarrow 2pu}}{\ell_{2pd\rightarrow 2pu}} \tag{D.61}$$

The result of implementing the axial conduction in the evaporator model equations produced the graph shown in Figure D.6. It should be noted that not all of the data points would solve. For the data points in which there were more than 25 °F of superheat, the evaporator model did not solve because an assumption was violated: more than half of the evaporator wanted to be superheated vapor. There is a slight leveling of the graph, but not all of the data points would solve. Since typically the superheat region of the evaporator fin experiences the highest fin temperature, it is from the superheated region that most of the heat conduction occurs. Although the heat transfer from the fin surface to the refrigerant is small due to the small refrigerant side heat transfer coefficient when compared with the two-phase zone, the heat transfer from the air to the fin surface in the superheated zone is large because most of the heat can be transferred back to the two-phase zone through conduction in the fin. Data points with substantially large amounts of superheat would therefore not solve in the model because the heat transfer from the air to the surface fin in the superheated region was so large that the solution violated the assumption that half of the evaporator was two-phase; more than half of the evaporator wanted to be superheated.

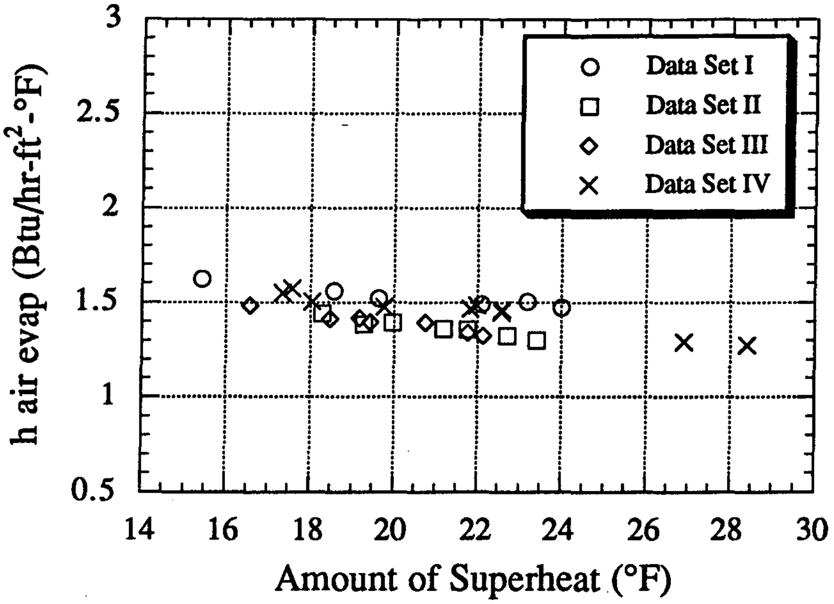

Figure D.6 Whirlpool air-side heat transfer coefficient (fin conduction)

It is possible that the evaporator is experiencing a dryout as seen in the Amana evaporator described in Appendix G. If dryout is the case then it is possible that this evaporator model, with fin conduction accounted for, is not correctly predicting the increasing rate of dryout as the superheating in the evaporator is increased. From the Amana evaporator, it was observed experimentally that after about 15 degrees of superheat, the saturated vapor point in the evaporator was already at the halfway point whereas the model predicted it to occur at around 40 degrees of superheat when fin conduction was occurring. For the Whirlpool evaporator model with fin conduction, the calculated amount of superheating needed to drive half the evaporator superheated vapor was around 25 degrees of superheating.

Based on the results of the three models, the optimized value of the air side heat transfer coefficient was obtained using the method of a mixed inlet evaporator air temperature. Since using a mixed air stream appeared to give the same results as an unmixed air stream, there appeared to be no reason to change the evaporator equations in the RFSIM model. As for the fin conduction, the results still showed that it was no better than when fin conduction was not considered.

D.2 Side-by-side Amana refrigerator

D.2.1 Evaporator heat transfer coefficient

D.2.1.1 Evaporator modeling

The evaporator located in the Amana refrigerator has nearly the same configuration as the Whirlpool refrigerator. The first half of the evaporator has a counterflow configuration with the refrigerant and air and the second half of the evaporator is in a parallel flow configuration. Figure D.7 shows a diagram of exactly how the evaporator looks sitting in the refrigerator.

For modeling the side-by-side Amana evaporator, it is noted that the inlet fresh food and freezer air do not mix before entering the evaporator. Therefore, it is necessary to model the evaporator where there are two different air streams which will eventually mix downstream after the evaporator fan. The same configuration of having 3 zones is used as in the Whirlpool refrigerator and is shown in Figure D.2. Equations used for modeling the side-by-side Amana evaporator are the same used to model the Whirlpool evaporator when two different air streams were considered. Equations D.16-D.41 were used for the Amana model along with the conductance equations shown as equation D.1-D.3. The assumption is made again that the fresh food and freezer air streams do not interact with one another while they flow over the evaporator.

D.2.1.2 Results

Solving equations D.1-D.3 and D.16-D.41 will allow us to estimate 3 parameters: air side heat transfer coefficient, split air fraction, and volumetric flow rate. Since the volumetric flow rate and split air fraction were estimated in another optimization program as described in Appendix B, it will be assumed that their values are fixed at 44.5 cfm and 0.82 respectively. From Appendix G, it is known that there will be a problem in estimating the air side heat transfer coefficient because of dryout occurring in the evaporator. To alleviate the problem, only steady-state data points with 15 degrees or less of superheat was used in the parameter estimation. This reduced the overall data set to just 7 data points.

The resulting optimization program estimated the air-side heat transfer coefficient by minimizing the error in the measured and calculated evaporator heat load. The evaporator heat load is experimentally measured through the calorimeter test where the total heater power inputted into the cabinets are known and the amount of heat leak through the cabinet walls are known because the cabinet conductances were previously estimated in Appendix B. The resulting optimization program calculated a value for the air side heat transfer coefficient of 1.56 Btu/hr-ft^2-°F. Figure D.8 shows a graph of the error in the measure and calculated heat load. The 95% confidence interval for this parameter estimation was around 55 Btu/hr-ft^2-°F or about 7% of the total evaporator load. This means that the estimated parameter can cause about a 7% error in the predicted evaporator load.

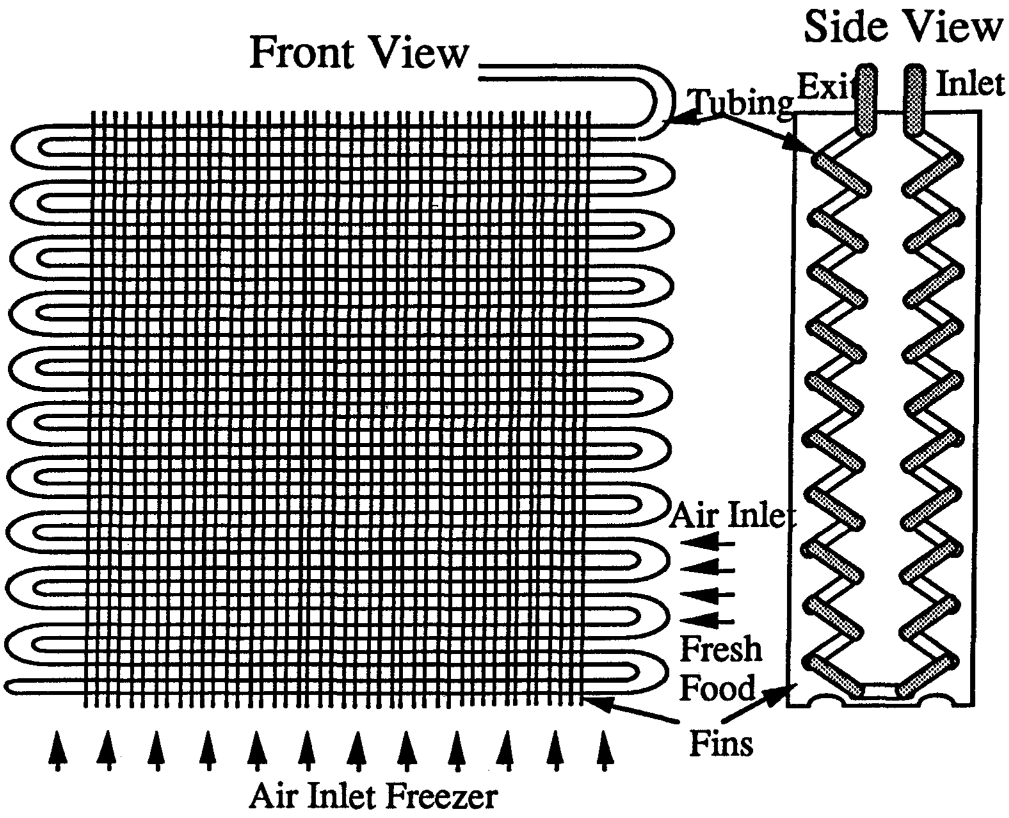

Figure D.7 Side-by-side Amana evaporator geometry

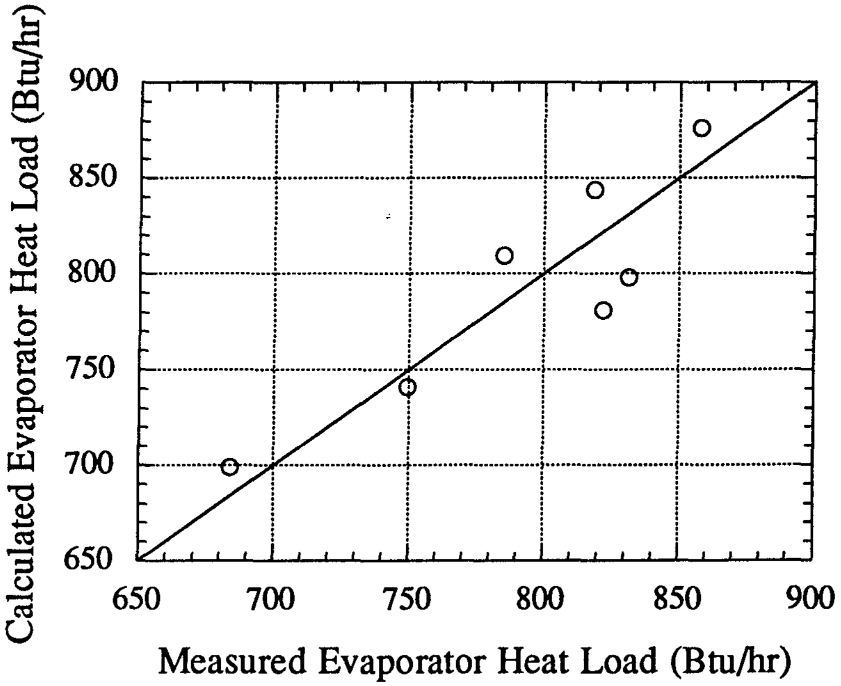

Figure D.8 Amana air-side heat transfer coefficient estimation (No Conduction)

Taking a look at air-side heat transfer coefficient solved point by point for all steady-state data shows the graph shown below in Figure D.9. Notice that the results seen up to 15 degree of superheat appear to be steady and constant and then afterwards there is a big drop-off in the air-side heat transfer coefficient which is where the evaporator model breaks down because of its inability to predict accurately the saturated vapor point in the evaporator.

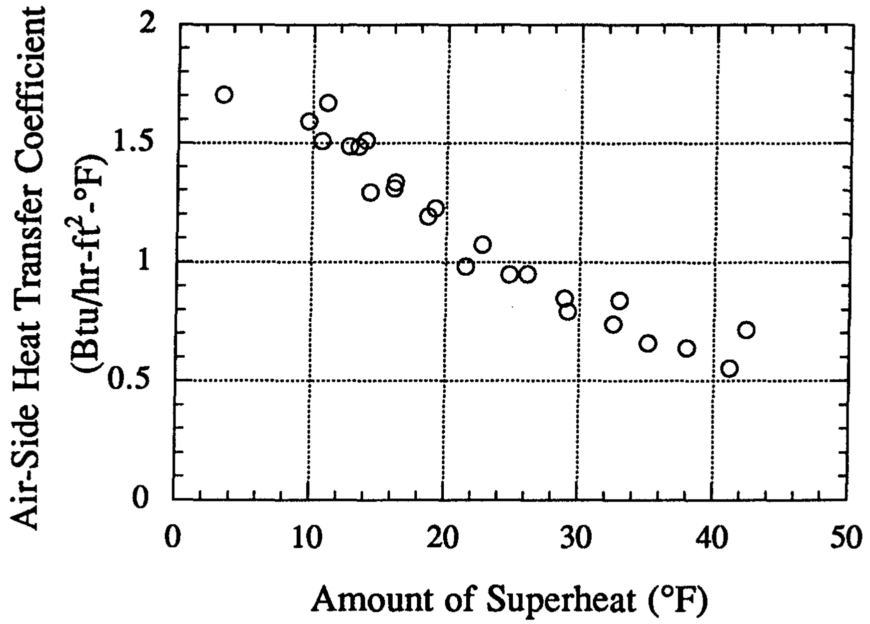

Figure D.9 Amana air-side heat transfer coefficient (freezer & fresh food air streams)

D.2.1.3 Evaporator model with two unmixed inlet air streams and fin conduction occurring

Appendix G showed that the Amana evaporator model is a little better in predicting the movement of the saturated vapor point when fin conduction was considered. The estimation of the air-side heat transfer coefficient was first performed without fin conduction which produced a 95% confidence interval of about 7% of the total evaporator load. The evaporator model was now rewritten again to see if our results would improve if fin conduction was considered in the evaporator model. First the effectiveness-NTU equations in the evaporator model had to be rewritten using a LMTD method such that we could solve for surface fin temperature. Since the evaporator is modeled as having a fresh food and freezer air stream, there are 4 LMTD equations written for each zone. A fresh food and freezer LMTD is written for the heat transfer from the air to the fin surface and then two more LMTD equations are written for the heat transfer from the fin surface to the refrigerant. For the refrigerant-side energy balance, there are now 6 different conduction variables which are added and subtracted from the three zones which account for the heat conduction between the three zones. The equations which represents the change from the effectiveness-NTU method to the LMTD method is shown below in equation D.62 through D.99.

Upstream two-phase zone:

$$Q_{2pu} + Q_{sup\rightarrow 2pu,frez} + Q_{sup\rightarrow 2pu,ff} + Q_{2pd\rightarrow 2pu,frez} + Q_{2pd\rightarrow 2pu,ff} = w\cdot\left(h_{711} - h_{7}\right) \tag{D.62}$$

$$Q_{2pu} = Q_{2pu,frez} + Q_{2pu,ff} \tag{D.63}$$

$$A_{2pu,frez} = f_{z}\cdot A_{2pu} \tag{D.64}$$

$$A_{2pu,ff} = \left(1 - f_{z}\right)\cdot A_{2pu} \tag{D.65}$$

$$Q_{2pu,frez} = h_{air,evap}\cdot A_{2pu,frez}\cdot LMTD_{2pu,Air\rightarrow Surf,frez} \tag{D.66}$$

$$LMTD_{2pu,Air\rightarrow Surf,frez} = \frac{\left(T_{a,evapin,frez} - T_{surf,2pu,frez}\right) - \left(T_{a,evapout,2pu,frez} - T_{surf,2pu,frez}\right)}{\ln\left[\left(T_{a,evapin,frez} - T_{surf,2pu,frez}\right)\Big/\left(T_{a,evapout,2pu,frez} - T_{surf,2pu,frez}\right)\right]} \tag{D.67}$$

$$Q_{2pu,ff} = h_{air,evap}\cdot A_{2pu,ff}\cdot LMTD_{2pu,Air\rightarrow Surf,ff} \tag{D.68}$$

$$LMTD_{2pu,Air\rightarrow Surf,ff} = \frac{\left(T_{a,evapin,ff} - T_{surf,2pu,ff}\right) - \left(T_{a,evapout,2pu,ff} - T_{surf,2pu,ff}\right)}{\ln\left[\left(T_{a,evapin,ff} - T_{surf,2pu,ff}\right)\Big/\left(T_{a,evapout,2pu,ff} - T_{surf,2pu,ff}\right)\right]} \tag{D.69}$$

$$Q_{2pu,frez} + Q_{sup\rightarrow 2pu,frez} + Q_{2pd\rightarrow 2pu,frez} = \frac{h_{ref,evap,2pu}}{\alpha_{evap}}\cdot A_{2pu,frez}\cdot LMTD_{2pu,Surf\rightarrow Ref,frez} \tag{D.70}$$

$$LMTD_{2pu,Surf\rightarrow Ref,frez} = \frac{\left(T_{surf,2pu,frez} - T_{711}\right) - \left(T_{surf,2pu,frez} - T_{7}\right)}{\ln\left[\left(T_{surf,2pu,frez} - T_{711}\right)\Big/\left(T_{surf,2pu,frez} - T_{7}\right)\right]} \tag{D.71}$$

$$Q_{2pu,ff} + Q_{sup\rightarrow 2pu,ff} + Q_{2pd\rightarrow 2pu,ff} = \frac{h_{ref,evap,2pu}}{\alpha_{evap}} \cdot A_{2pu,ff} \cdot LMTD_{2pu,Surf\rightarrow Ref,ff}$$

(D.72)

$$LMTD_{2pu,Surf\rightarrow Ref,ff} = \frac{\left(T_{surf,2pu,ff} - T_{711}\right) - \left(T_{surf,2pu,ff} - T_7\right)}{\ln\left[\left(T_{surf,2pu,ff} - T_{711}\right) \Big/ \left(T_{surf,2pu,ff} - T_7\right)\right]} \quad \text{(D.73)}$$

Downstream two-phase zone:

$$Q_{2pd} + Q_{sup\rightarrow 2pd,frez} + Q_{sup\rightarrow 2pd,ff} - Q_{2pd\rightarrow 2pu,frez} - Q_{2pd\rightarrow 2pu,ff} = w \cdot \left(h_{71} - h_{711}\right)$$

(D.74)

$$Q_{2pu} = Q_{2pu,frez} + Q_{2pu,ff} \quad \text{(D.75)}$$

$$A_{2pu,frez} = f_z \cdot A_{2pu} \quad \text{(D.76)}$$

$$A_{2pu,ff} = \left(1 - f_z\right) \cdot A_{2pu} \quad \text{(D.77)}$$

$$Q_{2pd,frez} = h_{air,evap} \cdot A_{2pd,frez} \cdot LMTD_{2pd,Air\rightarrow Surf,frez} \quad \text{(D.78)}$$

$$LMTD_{2pd,Air\rightarrow Surf,frez} = \frac{\left(T_{a,evapin,frez} - T_{surf,2pd,frez}\right) - \left(T_{a,evapmid,frez} - T_{surf,2pd,frez}\right)}{\ln\left[\left(T_{a,evapin,frez} - T_{surf,2pd,frez}\right) \Big/ \left(T_{a,evapmid,frez} - T_{surf,2pd,frez}\right)\right]}$$

(D.79)

$$Q_{2pd,ff} = h_{air,evap} \cdot A_{2pd,ff} \cdot LMTD_{2pd,Air\rightarrow Surf,ff} \quad \text{(D.80)}$$

$$LMTD_{2pd,Air\rightarrow Surf,ff} = \frac{\left(T_{a,evapin,ff} - T_{surf,2pd,ff}\right) - \left(T_{a,evapmid,ff} - T_{surf,2pd,ff}\right)}{\ln\left[\left(T_{a,evapin,ff} - T_{surf,2pd,ff}\right) \Big/ \left(T_{a,evapmid,ff} - T_{surf,2pd,ff}\right)\right]}$$

(D.81)

$$Q_{2pd,frez} + Q_{sup\rightarrow 2pd,frez} - Q_{2pd\rightarrow 2pd,frez} = \frac{h_{ref,evap,2pd}}{\alpha_{evap}} \cdot A_{2pd,frez} \cdot LMTD_{2pd,Surf\rightarrow Ref,frez}$$

(D.82)

$$\mathrm{LMTD}_{2pd,Surf\rightarrow Ref,frez} = \frac{\left(T_{surf,2pd,frez} - T_{71}\right) - \left(T_{surf,2pd,frez} - T_{711}\right)}{\ln\left[\left(T_{surf,2pd,frez} - T_{71}\right) \big/ \left(T_{surf,2pd,frez} - T_{711}\right)\right]} \quad (D.83)$$

$$Q_{2pd,ff} + Q_{sup\rightarrow 2pd,ff} - Q_{2pd\rightarrow 2pd,ff} = \frac{h_{ref,evap,2pd}}{\alpha_{evap}} \cdot A_{2pd,ff} \cdot \mathrm{LMTD}_{2pd,Surf\rightarrow Ref,ff}$$

(D.84)

$$\mathrm{LMTD}_{2pd,Surf\rightarrow Ref,ff} = \frac{\left(T_{surf,2pd,ff} - T_{71}\right) - \left(T_{surf,2pd,ff} - T_{711}\right)}{\ln\left[\left(T_{surf,2pd,ff} - T_{71}\right) \big/ \left(T_{surf,2pd,ff} - T_{711}\right)\right]} \quad (D.85)$$

Superheated zone:

$$Q_{sup} - Q_{sup\rightarrow 2pu,frez} - Q_{sup\rightarrow 2pu,ff} - Q_{sup\rightarrow 2pd,frez} - Q_{sup\rightarrow 2pd,ff} = w \cdot \left(h_9 - h_{71}\right)$$

(D.86)

$$Q_{sup} = Q_{sup,frez} + Q_{sup,ff} \quad (D.87)$$

$$A_{sup,frez} = f_z \cdot A_{sup} \quad (D.88)$$

$$A_{sup,ff} = \left(1 - f_z\right) \cdot A_{sup} \quad (D.89)$$

$$Q_{sup,frez} = h_{air,evap} \cdot A_{sup,frez} \cdot \mathrm{LMTD}_{sup,Air\rightarrow Surf,frez} \quad (D.90)$$

$$\mathrm{LMTD}_{sup,Air\rightarrow Surf,frez} = \frac{\left(T_{a,evapmid,frez} - T_{surf,sup,frez}\right) - \left(T_{a,evapout,sup,frez} - T_{surf,sup,frez}\right)}{\ln\left[\left(T_{a,evapmid,frez} - T_{surf,sup,frez}\right) \big/ \left(T_{a,evapout,sup,frez} - T_{surf,sup,frez}\right)\right]}$$

(D.91)

$$Q_{sup,ff} = h_{air,evap} \cdot A_{sup,ff} \cdot \mathrm{LMTD}_{sup,Air\rightarrow Surf,ff} \quad (D.92)$$

$$\mathrm{LMTD}_{sup,Air\rightarrow Surf,ff} = \frac{\left(T_{a,evapmid,ff} - T_{surf,sup,ff}\right) - \left(T_{a,evapout,sup,ff} - T_{surf,sup,ff}\right)}{\ln\left[\left(T_{a,evapmid,ff} - T_{surf,sup,ff}\right) \big/ \left(T_{a,evapout,sup,ff} - T_{surf,sup,ff}\right)\right]}$$

(D.93)

$$Q_{sup,frez} - Q_{sup\rightarrow 2pu,frez} + Q_{sup\rightarrow 2pd,frez} = \frac{h_{ref,evap,sup}}{\alpha_{evap}} \cdot A_{sup,frez} \cdot LMTD_{sup,Surf\rightarrow Ref,frez}$$

(D.94)

$$LMTD_{sup,Surf\rightarrow Ref,frez} = \frac{\left(T_{surf,sup,frez} - T_9\right) - \left(T_{surf,sup,frez} - T_{71}\right)}{\ln\left[\left(T_{surf,sup,frez} - T_9\right) \Big/ \left(T_{surf,sup,frez} - T_{71}\right)\right]} \quad \text{(D.95)}$$

$$Q_{sup,ff} - Q_{sup\rightarrow 2pu,ff} + Q_{sup\rightarrow 2pd,ff} = \frac{h_{ref,evap,sup}}{\alpha_{evap}} \cdot A_{sup,ff} \cdot LMTD_{sup,Surf\rightarrow Ref,ff}$$

(D.96)

$$LMTD_{sup,Surf\rightarrow Ref,ff} = \frac{\left(T_{surf,sup,ff} - T_9\right) - \left(T_{surf,sup,ff} - T_{71}\right)}{\ln\left[\left(T_{surf,sup,ff} - T_9\right) \Big/ \left(T_{surf,sup,ff} - T_{71}\right)\right]} \quad \text{(D.97)}$$

System:

$$Q_{evap} = Q_{2pu} + Q_{2pd} + Q_{sup} \quad \text{(D.98)}$$

$$A_{evap} = A_{2pu} + A_{2pd} + A_{sup} \quad \text{(D.99)}$$

Together there are 6 conduction variables meaning 6 conduction equations which characterize the evaporator. There are three zones considered in the evaporator and two different air streams. Since the two air streams are modeled such that they do not interact which one another, there is no interaction between the fin temperature of one air stream with the fin temperature of the other air stream. Therefore for the freezer air stream, there are 3 equations which represent the conduction between the superheated zone and the two two-phase zones and 3 more equations for the fresh food air stream. Again the assumption is made that the evaporator fins are made of an aluminum alloy. Together there are 43 fins on the Amana evaporator. The assumption is then made that the split-air fraction will dictate what percentage of the evaporator fins are in contact with the freezer air stream and what percentage is in contact with the fresh food air stream. Finally, the perpendicular area needed in writing the conduction equations assume that the fins are stacked together and act as one big mass instead of 43 different fins acting separately. The model equations are shown as equation D.100 to D105.

Conduction Equations:

$$Q_{sup\rightarrow 2pu,frez} = \frac{k_{Al} \cdot A_{\perp,sup\rightarrow 2pu,frez}}{\ell_{sup\rightarrow 2pu}} \qquad (D.100)$$

$$Q_{sup\rightarrow 2pd,frez} = \frac{k_{Al} \cdot A_{\perp,sup\rightarrow 2pd,frez}}{\ell_{sup\rightarrow 2pd}} \qquad (D.101)$$

$$Q_{2pd\rightarrow 2pu,frez} = \frac{k_{Al} \cdot A_{\perp,2pd\rightarrow 2pu,frez}}{\ell_{2pd\rightarrow 2pu}} \qquad (D.102)$$

$$Q_{sup\rightarrow 2pu,ff} = \frac{k_{Al} \cdot A_{\perp,sup\rightarrow 2pu,ff}}{\ell_{sup\rightarrow 2pu}} \qquad (D.103)$$

$$Q_{sup\rightarrow 2pd,ff} = \frac{k_{Al} \cdot A_{\perp,sup\rightarrow 2pd,ff}}{\ell_{sup\rightarrow 2pd}} \qquad (D.104)$$

$$Q_{2pd\rightarrow 2pu,ff} = \frac{k_{Al} \cdot A_{\perp,2pd\rightarrow 2pu,ff}}{\ell_{2pd\rightarrow 2pu}} \qquad (D.105)$$

D.2.1.4 Results

The above equations were used to estimate the air-side heat transfer coefficient for only the steady-state data points with 15 degrees or less of superheat. The program again minimized the error in the measured and calculated evaporator heat load. The result of the optimization program are shown below in Figure D.10. The estimated air-side heat transfer coefficient was 1.58 Btu/hr-ft^2-°F which had a 95% confidence interval on the estimated evaporator heat load of 52 Btu/hr or about 7% of the error.

The air side heat transfer coefficient was then solved and plotted for all of the steady-state data points and shown below in Figure D.11. Here the same results are seen where the air-side heat transfer decreases with increasing quality. It appears that with 15 degrees of superheating or less, it does not matter in the evaporator model whether fin conduction is considered or not since the results will be the same. What fin conduction does do however is increase the amount of area that the superheated zone of the evaporator does see which is more consistent with the experimental data.

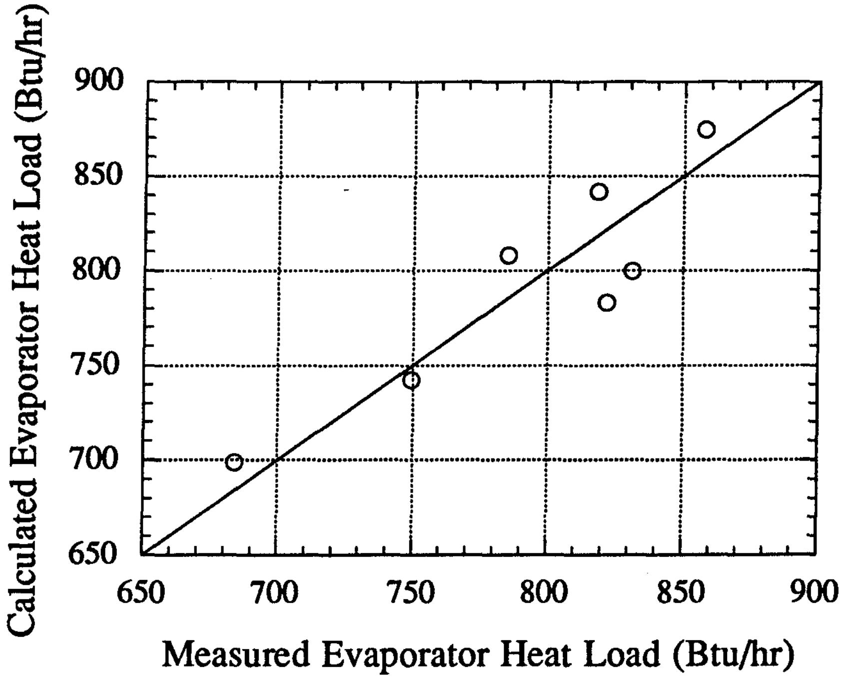

Figure D.10 Amana air-side heat transfer coefficient estimation (fin conduction)

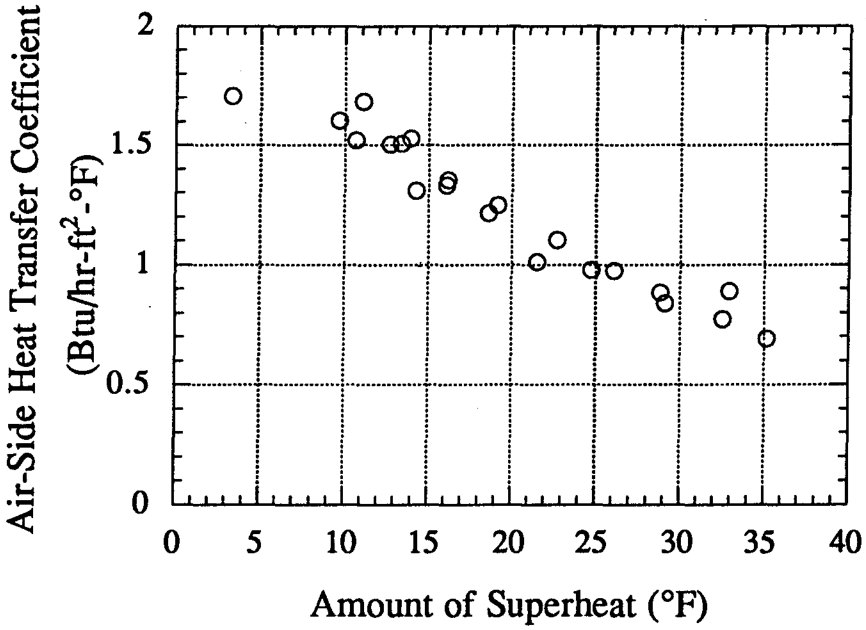

Figure D.11 Amana air-side heat transfer coefficient (fin conduction)

D.3 Conclusions

For both evaporators tested, there was noticeable decrease in the air-side heat transfer coefficient as superheat was increased. Both evaporators saw a constant volumetric flow rate and therefore almost a constant velocity. This suggest that perhaps the evaporator model is too general and a more detailed model needs to be examined. Section G.4 of Appendix G gives some new insights as to what might possibly be occurring for the side-by-side Amana evaporator. The addition of thermocouples on the evaporator fins has aided in the understanding of the evaporator. After 15 °F of superheat, more than half of the evaporator would become superheated vapor and the parallel flow section of the evaporator acted as a desuperheating region. The reason why the evaporator model was unable to see this occurring at 15 °F of superheat was due mainly to the fin conduction equations being incorrect and to the possibility of contact resistance occurring between the fins and tubes. An analysis explained in Appendix G has determined that the true air-side heat transfer coefficient could be estimated with data containing low superheat. At low superheat, the evaporator is already almost all 2-phase and therefore the fin conduction occurring in the evaporator is small. Some of the reasons why a larger drop in the air-side heat transfer coefficient is seen in the Amana model than in the Whirlpool model might have to do with their different geometry. Both evaporators had the same depth, but the Whirlpool evaporator was designed for a top mount refrigerator, such that its length is about three times the height. The Amana evaporator was designed for a side-by-side, such that the height is about one and a half times the length. Actual measurements show that the overall tube length of the two evaporators are about the same, but the height of the Amana evaporator is about double of the Whirlpool height. Therefore, this additional height might be the cause for larger errors in the Amana model.

Appendix E

Compressor Parameter Estimations

E.1 Introduction

The Appendix documents the results of our in-situ calorimetry and how it compares to the generic mass flow and power data maps provided by compressor manufacturers. The estimated value of the compressor shell heat transfer coefficient is important for accurate simulation of compressor discharge temperature and hence compressor performance

E.2 Whirlpool high-side rotary compressor

E.2.1 Compressor heat loss

The compressor is one of the most difficult components of the system to model because of its complicated flow and heat transfer processes. Together there are three parameters from the compressor which need to be analyzed. The three parameters are the compressor heat loss, the refrigerant mass flow rate, and the compressor power. Performance maps such as the compressor power map and the refrigerant mass flow map have been generated by the manufacturer in order to provide a simplified way of calculating these two parameters. Typically, these maps use the inlet and outlet saturation temperatures in a bi-quadratic curve fit in order to estimate these parameters. The compressor maps, however, do not provide any information about the heat loss seen in the compressor. Numerous papers (Davis and Scott, 1978) have proposed detailed compressor models which account for compressor parameters like clearance volume, compressor speed, and heat loss, but these models only add complexity to the system model (Kirby and Bullard, 1997). In this appendix, an air-side heat transfer coefficient for the compressor will be estimated which can then be used to predict the compressor heat loss in the simulation model.

Knowing the temperature at the inlet of the condenser and at the exit of the condenser fan along with the power of the fan, an energy balance can be performed to estimate the amount of heat lost by the compressor. This heat loss is then used to estimate an overall conductance from the shell surface to the air. Figure E.1 shows a schematic of where air temperature readings were taken and equations E.1 through E.5 shows how hA_{comp} is calculated.

$$\dot{m}_r = \frac{\dot{Q}_{evap,load}}{h_{compin} - h_{condout}} \tag{E.1}$$

$$W_{comp} = (SysPower - W_{evap\,fan} - W_{cond\,fan}) \tag{E.2}$$

$$-Q_{comp} + W_{comp} = w \cdot (h_{compout} - h_{compin}) \tag{E.3}$$

$$\dot{Q}_{comp} = hA_{comp} \cdot (T_{shell} - T_{a,condout}) \tag{E.4}$$

$$T_{shell} = 0.88355 \cdot T_{compout} - 3.4407 \tag{E.5}$$

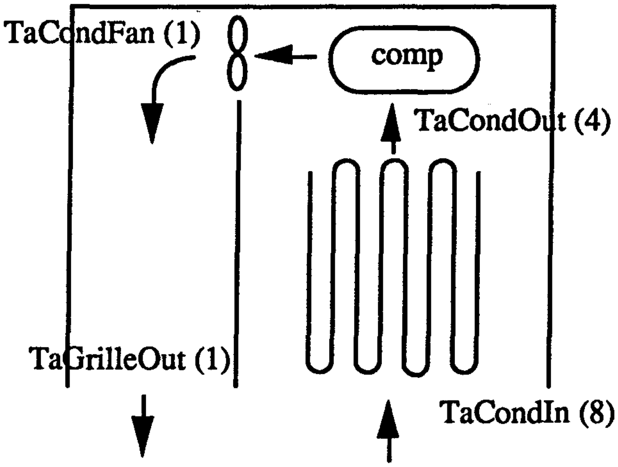

Figure E.1 Temperature readings for the estimation of $(hA)_{comp}$

The compressor shell temperature is not directly calculated in the simulation model, but observations of our data revealed a linear relationship between the compressor shell temperature and the discharge temperature as shown in Equation E.5. Therefore, the compressor shell temperature can be calculated from the discharge temperature. Using this curve fit, the shell temperature could be predicted within a confidence interval of 0.8 °F. The measurements showed that the compressor shell temperature varied from 150 to 190 °F for ambient temperatures of 60 to 100 °F.

The conductance of the compressor was estimated using 33 data points, all of which had subcooled condenser exits. The estimated parameter minimized the error between the measured and predicted compressor heat loss. The estimations resulted in an average hA_{comp} of 5.17 Btu/hr-°F as shown in Figure E.2. This produced a 95% confidence interval for the predicted compressor heat loss of about 13 Btu/hr, or about 3.8% of the average heat loss.

E.2.2 Compressor mass flow and power prediction

The mass flow through the compressor is calculated using bi-quadratic curve fit of the manufacturer's compressor calorimeter data for a typical compressor of this model. They express mass flow and power as functions of the saturation temperatures at the inlet and exit of the compressor. These curve fits do not produce very accurate predictions, however, because the manufacturer's data hold the suction gas inlet temperature constant at 90°F to the compressor. The temperature of the suction gas at the accumulator inlet may be as low as 60°F during actual operating conditions, which means that the specific volume of the gas may differ substantially from that used by the manufacturer to create the maps. The specific volume of the gas is inversely proportional to mass flow through the compressor; we therefore use equation E.6 to correct the map (Fisher and Rice, 1983).

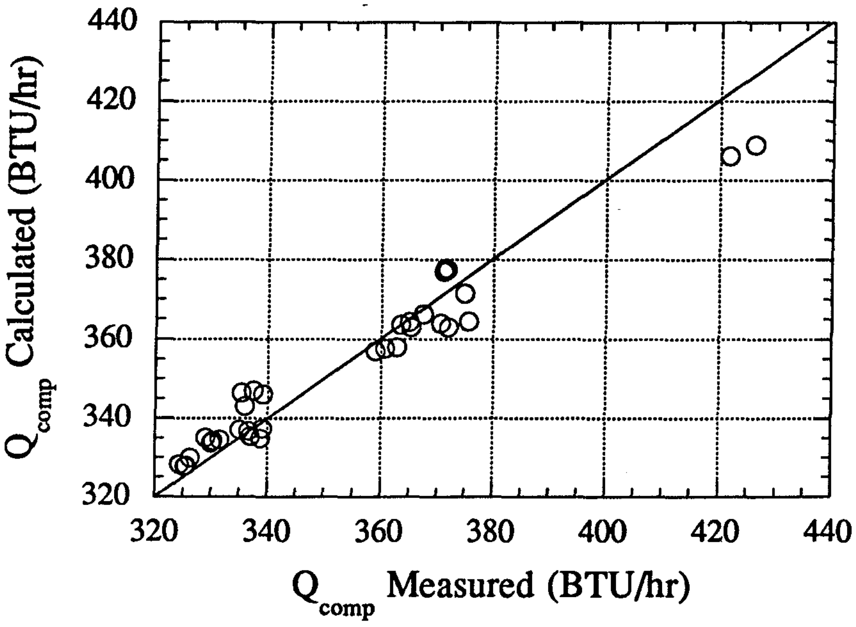

Figure E.2 Calculated and measured compressor heat rejection

$$\dot{m}_{actual} = \frac{\upsilon_{map}}{\upsilon_{actual}} \dot{m}_{map} \tag{E.6}$$

When the mass flow predictions from the corrected and uncorrected map are compared with the mass flow calculated from an energy balance across the evaporator, it appears that the corrected map does not do a significantly better job at predicting mass flow rate. Therefore, a new bi-quadratic compressor map was created that used our existing data along with the 9 data points from the compressor manufacturer. When this new map was compared to our measured mass flow, the new map appears to predict the mass flow rate fairly accurately. A graph of the predicted mass flow vs. measured mass flow is presented in Figure E.3 for the three different cases.

The uncorrected map had a bias error of 2.2 lbm/hr, while the corrected map performed no better with a bias error of 2.1 lbm/hr. Making a new map using the existing data along with the nine points from the manufacturer produced a better map with a bias error of 0.1 lbm/hr.

Fischer and Rice also proposed a correction to the power map, which takes the form of equation E.7.

$$\dot{W}_{actual} = \left(\frac{\dot{m}_{actual}}{\dot{m}_{map}}\right)\left(\frac{\Delta h_{isen,actual}}{\Delta h_{isen,map}}\right)\dot{W}_{map} \tag{E.7}$$

However, for a rotary compressor, this equation yields values for $\dot{W}_{actual}$ that are equal to $\dot{W}_{map}$. This occurs because the volumetric efficiency of the compressor is extremely close to 1. Equation E.7 implies that the work of isentropic compression from one pressure to another is nearly independent of the temperature of the gas, which is a direct result of our assumptions. For a reciprocating compressor, however, this factor would provide a correction, because the volumetric efficiency term would not be near a value of 1. The power map did not do a very good job of predicting compressor power, as Figure E.4 shows.

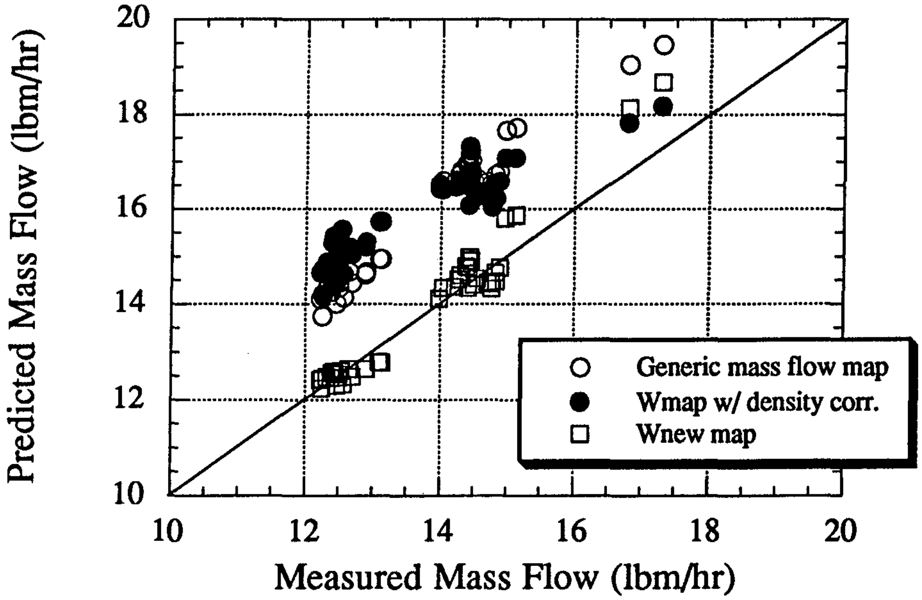

Figure E.3 Comparison of predicted vs. measured mass flow

A new power map was created that used the existing power data along with the power data from the manufacturer. As a result, the power error was reduced from having a bias error of -4.8 W to having a bias error of 0.3 W.

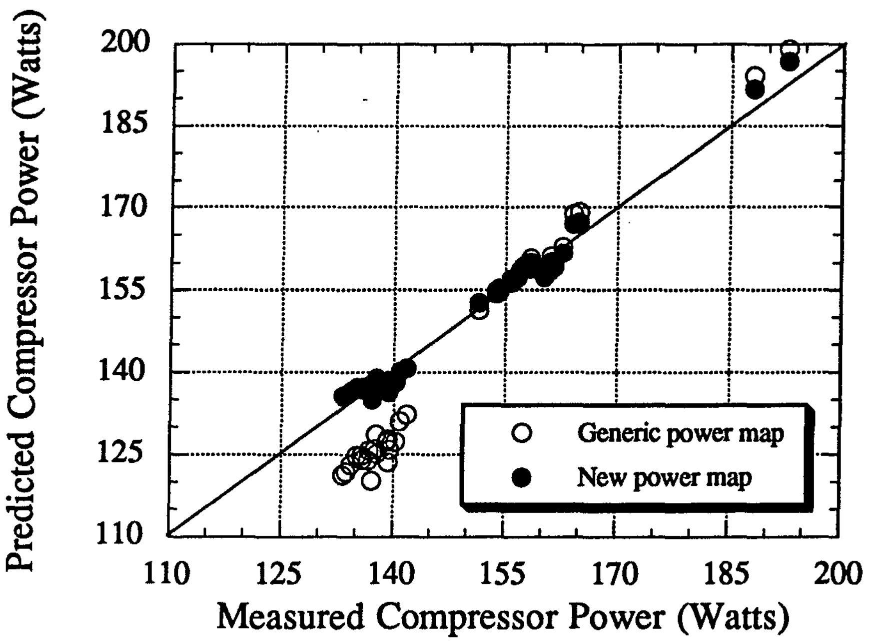

Figure E.4 Comparison of predicted vs. measured compressor power

E.3 Side-by-side Amana low-side reciprocating compressor

E.3.1 Compressor heat loss

The side-by-side Amana refrigerator has the configuration shown below in Figure E.5 for the placement of the air thermocouples. The model for the estimation of the condenser air-side heat transfer coefficient uses the same equations as those used in the Whirlpool model. In the Amana refrigerator, air thermocouples were not placed at the condenser exit so an air-side energy balance was written across the condenser to solve for the exit condenser air temperature (shown in Equation E.12). Also, another linear curve fit was performed so that the compressor shell temperature could be estimated from the compressor discharge temperature (shown in Equation E.13). The equations used in the parameter estimation are shown below in equations E.8 through E.13.

$$w = \frac{\dot{Q}_{evap,load}}{h_{compin} - h_{condout}} \tag{E.8}$$

$$W_{comp} = (SysPower - W_{evap\,fan} - W_{cond\,fan}) \tag{E.9}$$

$$-Q_{comp} + W_{comp} = w \cdot (h_{compout} - h_{compin}) \tag{E.10}$$

$$\dot{Q}_{comp} = hA_{comp} \cdot (T_{shell} - T_{a,condout}) \tag{E.11}$$

$$Q_{cond} = \dot{m}_{cond\ air} \cdot C_{p,air} \cdot \left(T_{a,GrilleIn} - T_{a,CondOut}\right) \tag{E.12}$$

$$T_{shell} = 0.83541 \cdot T_{compout} + 7.8596 \tag{E.13}$$

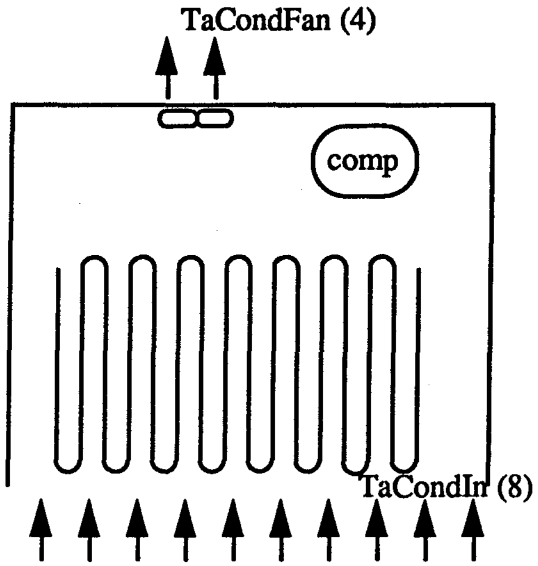

Figure E.5 Side-by-side Amana refrigerator configuration

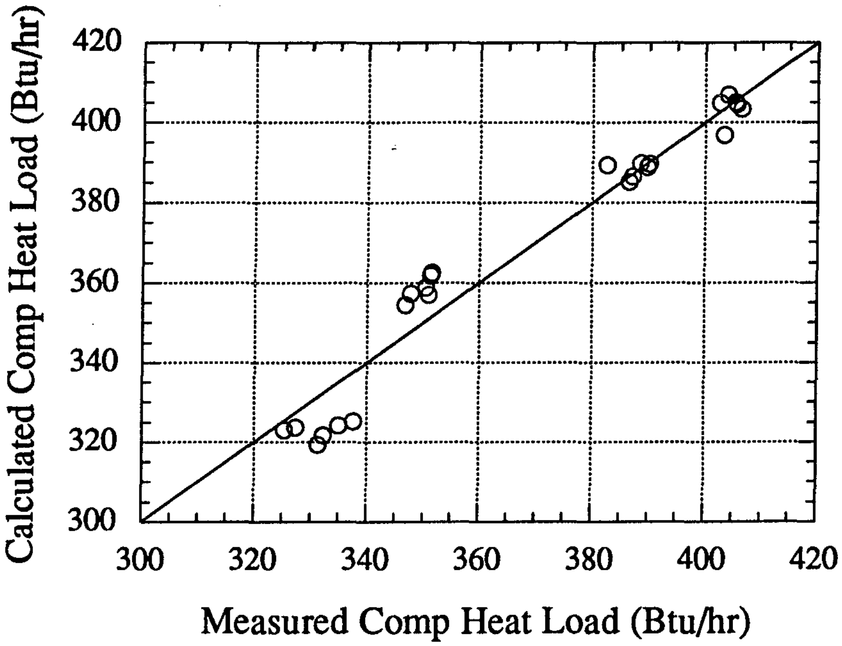

Figure E.6 Side-by-side Amana compressor hA estimation

Together there were 24 steady state data points used in the parameter estimation taken at 4 different ambient temperature. A compressor heat transfer value, hA_{comp}, of 5.50 Btu/hr-°F minimized the error in the measured and calculated compressor heat load. The 95% confidence interval for the compressor heat load was 15 Btu/hr or about 4% of the compressor heat load. Figure E.6 below shows the measured and calculated heat load for all 24 data points.

E.3.2 Compressor mass flow and power map

The compressor map for this particular compressor was obtained from the manufacturer and used to compare the mass flow which was calculated from in situ calorimeter data experimental obtained. Compressor maps furnished by the manufacturer use a bi-quadratic equation to curve fit the mass flow with the evaporating and condensing temperature. As mentioned earlier, compressor maps are typically made with data such that the suction gas entering the compressor is held constant at 90 °F. Correction factors for the suction inlet gas have been made as shown in equation E.5. In addition, refrigeration operation at low ambient temperatures will have condensing temperatures below 90 °F which require extrapolation from the manufacturer's map. Therefore, a new compressor map was produced from experimental data and data provided by the manufacturer. Figure E.7 shows how well the mass flow compares with the compressor map. Performing the suction gas density correction showed not to improve the results significantly. Overall, the compressor map is about 10% off from our calculated value. Typically, compressor maps can be anywhere from 5 to 10% off so this error falls within their uncertainty.

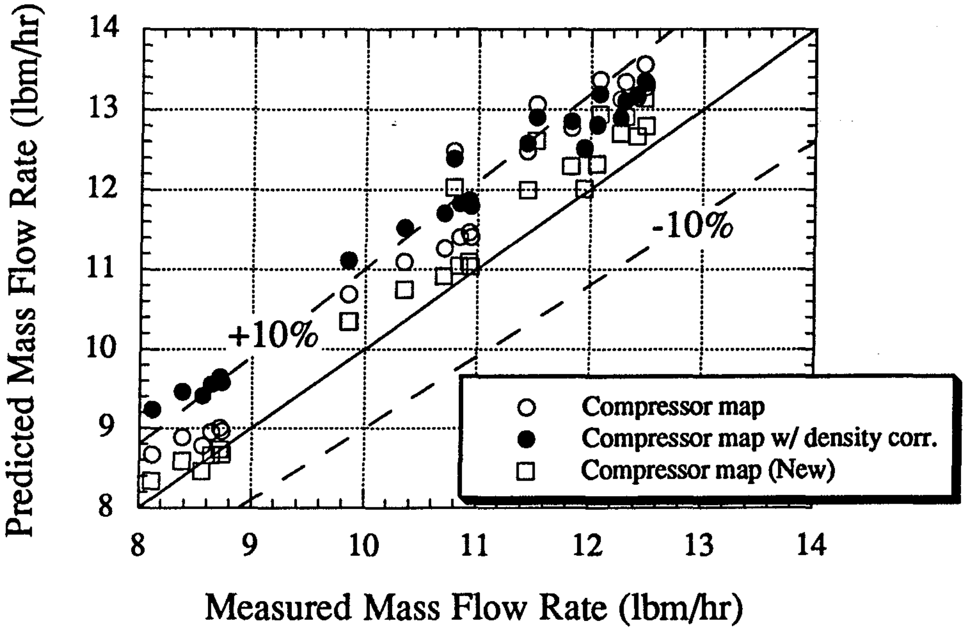

Figure E.7 Side-by-side Amana compressor map comparison

The power map produced by the manufacturer also uses a bi-quadratic curve fit as is done with the mass flow map for the condensing and evaporating temperature. Since a new mass flow map was produced using existing data along with the manufacturer's data, a new power map was also produced. For the experimental refrigerator, a watt transducer is used to measure the power consumed by the compressor. Figure E.8 shows for the 24 steady state data points, the measured power from the watt transducer as compared with the power predicted with the power maps. Figure E.8 shows that there is a good agreement with both maps in predicting compressor power.

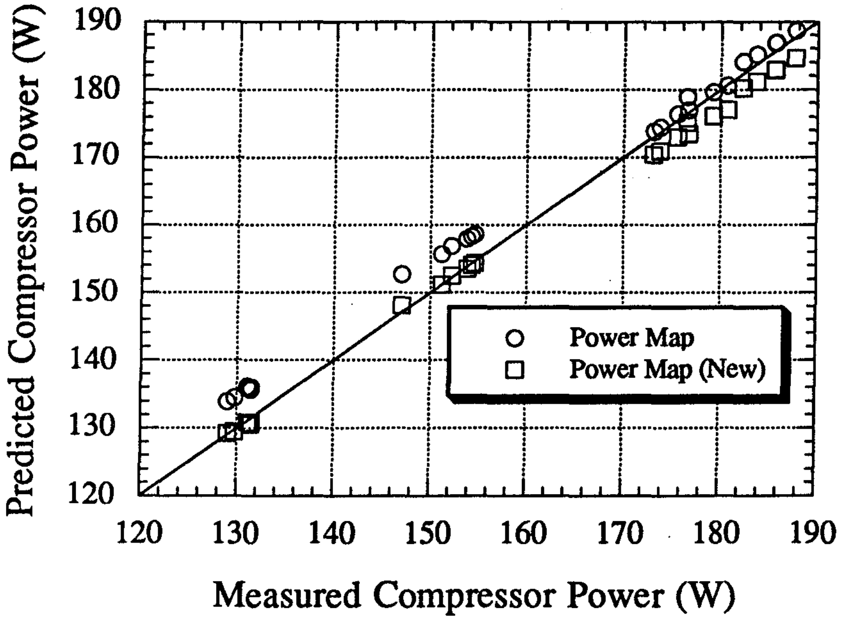

Figure E.8 Side-by-side Amana power map comparison

Appendix F

Post Condenser Loop UA Parameter Estimation

F.1 Post condenser loop

The post condenser loop, an extension of the liquid line, provides removal of the moisture on the freezer and fresh food door. This has added another 14 ft to the length, but more importantly it has added complexity to the model as now there is heat transfer coming off the liquid line. For this heat transfer, a simple UA parameter will be estimated based on assumptions about what temperature difference drives this heat transfer.

F.2 Post condenser loop model

For the post condenser loop, there are three different types of scenarios which can occur:

1) subcooled condenser outlet; refrigerant remains subcooled until capillary tube inlet
2) 2-phase condenser outlet; refrigerant becomes subcooled at capillary tube inlet
3) 2-phase condenser outlet; refrigerant remains 2-phase until capillary tube inlet

Currently the first scenario can be used in estimating a UA parameter because the enthalpy at both the inlet and outlet of the liquid line can be determined through pressure and temperature measurements. From cabinet load calorimetry, the refrigerant mass flow rate can be determined in order for a refrigerant side heat transfer equation to be used to calculated the total heat transfer from the liquid line. For scenarios two and three, a quality state exists and therefore the measured heat transfer from the liquid line would not be known. The UA parameter estimated from scenario one, however, should apply to all 3 cases because almost all of the resistance should be on the air-side and the foam insulation, and not on the refrigerant-side. At the mass flow rates in our experiments, the refrigerant side heat transfer coefficient is about 50 Btu/hr-ft^2-°F for subcooled liquid and about 360 Btu/hr-ft^2-°F for the 2-phase refrigerant.

Figure F.1 shows a schematic of the post condenser loop and the heat transfer from the post condenser loop to the two compartments denoted as $Q_{liqline\_ff}$ and $Q_{liqline\_fz}$. Since there are two heat transfer terms, it was necessary to solve for state 3M which is located at the top section dividing the fresh food and freezer compartment. Equation F.1 through F.7 shows the equations used for estimating the UA value.

$$Q_{liqline} = w \cdot (h_3 - h_4) \tag{F.1}$$

$$Q_{liqline\_ff} = w \cdot (h_3 - h_{3M}) \tag{F.2}$$

$$Q_{liqline\_ff} = UA_{liqline} \cdot (LMTD_{liqline\_ff}) \tag{F.3}$$

$$\mathrm{LMTD}_{\mathrm{liqline\_ff}} = \frac{(\mathrm{T3} - \mathrm{TaFreshF}) - (\mathrm{T3M} - \mathrm{TaFreshF})}{\ln\left[(\mathrm{T3} - \mathrm{TaFreshF}) \big/ (\mathrm{T3M} - \mathrm{TaFreshF})\right]} \qquad (\mathrm{F.4})$$

$$Q_{\mathrm{liqline\_fz}} = w \cdot \left(h_{3M} - h_4\right) \qquad (\mathrm{F.5})$$

$$Q_{\mathrm{liqline\_fz}} = \mathrm{UA}_{\mathrm{liqline}} \cdot \left(\mathrm{LMTD}_{\mathrm{liqline\_fz}}\right) \qquad (\mathrm{F.6})$$

$$\mathrm{LMTD}_{\mathrm{liqline\_fz}} = \frac{(\mathrm{T3M} - \mathrm{TaFrez}) - (\mathrm{T4} - \mathrm{TaFrez})}{\ln\left[(\mathrm{T3M} - \mathrm{TaFrez}) \big/ (\mathrm{T4} - \mathrm{TaFrez})\right]} \qquad (\mathrm{F.7})$$

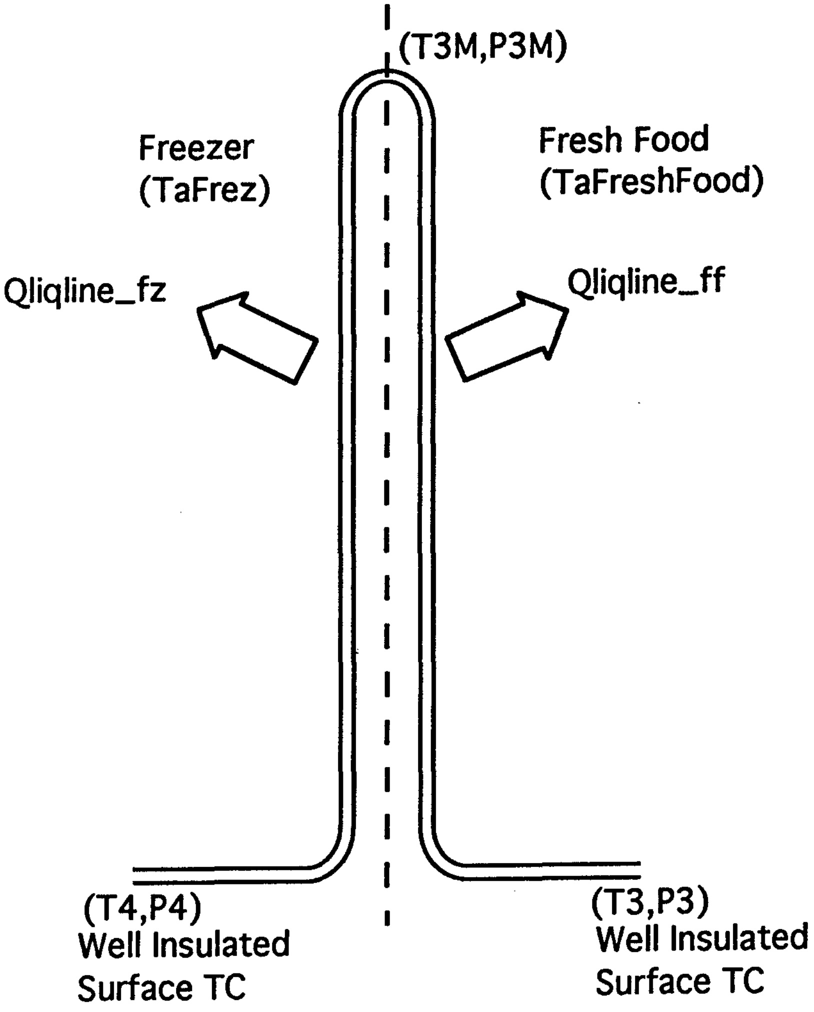

Figure F.1 Post condenser loop model

When this model is used to estimate a $\mathrm{UA}_{\mathrm{liqline}}$ for each data point, the graph shown in Figure F.2 is obtained.

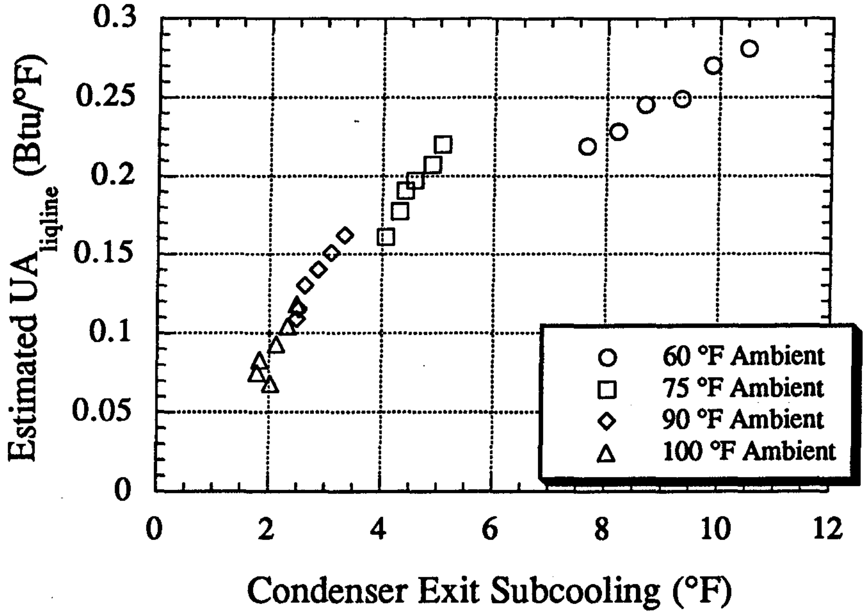

Figure F.2 Estimated $UA_{liqline}$ vs. condenser subcooling

The graph shows a large decrease in the estimated UA as subcooling decreases. An estimate on radiation effects was performed, but was seen to be insignificant for the data taken. One possibility is that at the low condenser subcooling, the refrigerant might not be completely subcooled. Tiny bubbles could still exist. This would cause an underprediction in the liquid line heat transfer for the low subcooling cases which is what is seen in the data. The graph suggests that perhaps as condenser subcooling is increased, the curve will flatten out at a value of around 0.25 Btu/°F. Because of the possible errors in measuring subcooling at the 75, 90, and 100 °F data, the UA parameter was estimated using only the 60 °F ambient data since that data set showed us the highest amount of subcooling coming from the condenser outlet.

F.3 Results

Equations F.1 through F.7 were then rewritten so that the $UA_{liqline}$ parameter could be estimated by minimizing the error between the measured and calculated values of the post condenser loop heat transfer. The results showed that the $UA_{liqline}$ is around 0.242 Btu/hr-°F with a 95% confidence interval on the post condenser loop heat transfer of 2.8 Btu/hr or around 15% of the total. Although the associated error in the $UA_{liqline}$ parameter produces about a 15% error in the heat transfer, the post condenser loop heat transfer itself is only around 3% of the total evaporator load so the combined results show that the estimated parameter will cause a 0.5% error in the calculated evaporator heat load. Figure F.3 shows the measured and calculated post condenser loop heat transfer using the $UA_{liqline}$ value of 0.242 Btu/hr-°F

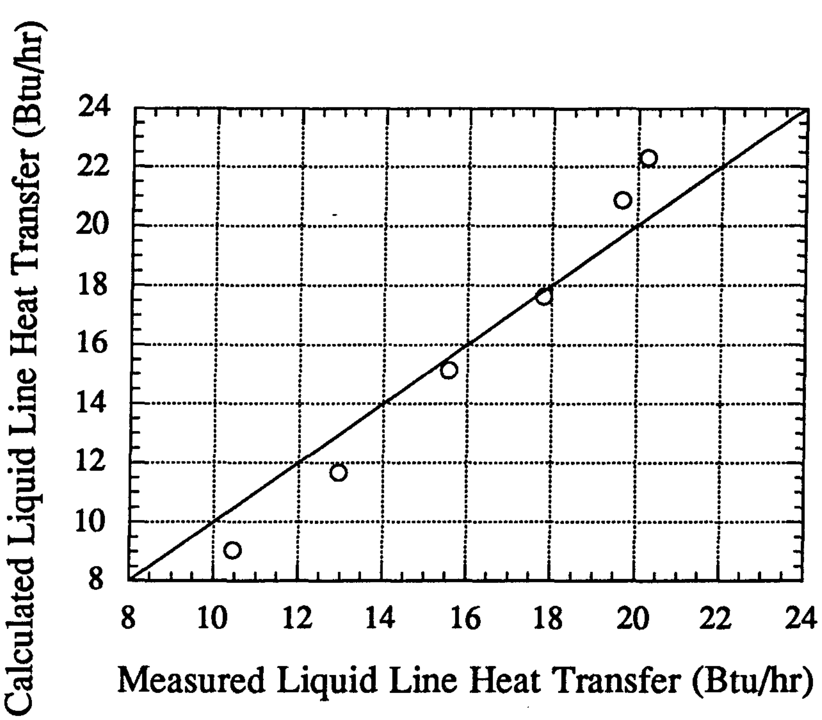

Figure F.3 Liquid line heat transfer estimation

F.4 Verification of assumptions made

For the parameter estimation, only data where subcooling existed at both the inlet and exit of the liquid line was used since this allowed for a refrigerant-side energy balance to be used in calculating the experimentally measured amount of heat transfer occurring. Now with the $UA_{liqline}$ parameter estimated, an analysis will show that almost all of the resistance occurs on both the air-side and through the foam insulation. Therefore the results can be used for any state occurring on the refrigerant side which will be either subcooled liquid or 2-phase refrigerant. Results in the condenser Appendix have already shown that the resistance due to the copper tube wall is negligible and can be ignored.

The total outer surface area for the post condenser loop, which has an outer diameter of 0.1875 in. and a length of 15 ft, is calculated to be around 0.736 ft^2. This means the overall heat transfer coefficient for the liquid line is estimated at around 0.329 Btu/hr-ft^2-°F. The heat transfer coefficient of both subcooled liquid and two-phase has been seen to be around 50 Btu/hr-ft^2-°F and 360 Btu/hr-ft^2-°F respectively. Therefore the resistance of the subcooled liquid and the two-phase refrigerant is less than 1 % of the total resistance. This essentially proves that almost all of the resistance does occur on the air-side and through the foam insulation. Thus the $UA_{liqline}$ parameter estimated should still be valid for the other two cases where there is a two-phase inlet into the post condenser loop and either a two-phase exit or subcooled exit.

Appendix G

Evaporator Dryout At High Superheat

G.1 Introduction

The evaporator seen in most modern refrigerators, including the side-by-side Amana refrigerator used for testing, is a configuration where the inlet refrigerant comes down in a counterflow configuration with the air and then bends upwards and becomes parallel flow with the air. Some of the problems seen with this type of evaporator is its tendency to dry out more than half of the evaporator at high compartment temperatures where the evaporator is experiencing a large degree of superheat.

G.2 Experimental data

Suspicion of a dryout occurring in the evaporator first became known when the air-side heat transfer coefficient of the Amana refrigerator was first estimated. It was seen in the air-side heat transfer estimation that there was a drop-off as superheating was increased which leads to the conclusion that there is less heat being removed than what the model wants to predict. It was then discovered through experimental data that at the high degree of superheating, the evaporator was drying out more than half of its area, while the model would still predict that a two-phase flow mixture existed over half of the evaporator. This is consistent with what was seen in the air-side heat transfer estimation because at the high degree of superheating, more than half of the evaporator is experiencing vapor-to-vapor heat transfer which has a low heat transfer rate. On the other hand, the model sees more than half of the evaporator as a two-phase flow with a relatively high refrigerant-side heat transfer coefficient. Therefore in order for the evaporator load to balance, the model must make the air-side heat transfer coefficient lower and lower as superheating is increased.

G.2.1 Thermocouples on evaporator fin

Experimental data confirming that the evaporator was drying out at high superheating was obtained by placing surface thermocouples on the evaporator fin. A total of 8 thermocouples were used on the evaporator: 4 thermocouples on the tenth fin counting from the right side and 4 on the tenth fin counting from the left side of the evaporator. Since the warmer fresh food air enters on the right side of the evaporator, the thermocouples placed on the tenth fin from the right side will be known as the fresh food fin temperature and the 4 thermocouples placed on the tenth fin counting from the left will be known as the freezer fin temperature. The precise placement of the four thermocouples on each fin is shown below in Figure G.1. In order to get an accurate reading of the surface temperature of the fin, it was necessary to run the thermocouple wire down the fin and glue the wire directly to the fin. Therefore, the thermocouple beads located at the top of the evaporator fin would have a wire that ran down the length of the fin and then back up. The thermocouple beads located near the bottom of the evaporator simply had a wire running upwards to the top. Since the fin spacing between the consecutive fins was just 0.1875 in, no type of insulation wrap was placed to cover the thermocouple bead. It was believed that by running the thermocouple wire down the length of the fin, the thermocouple bead would essentially read the fin temperature.

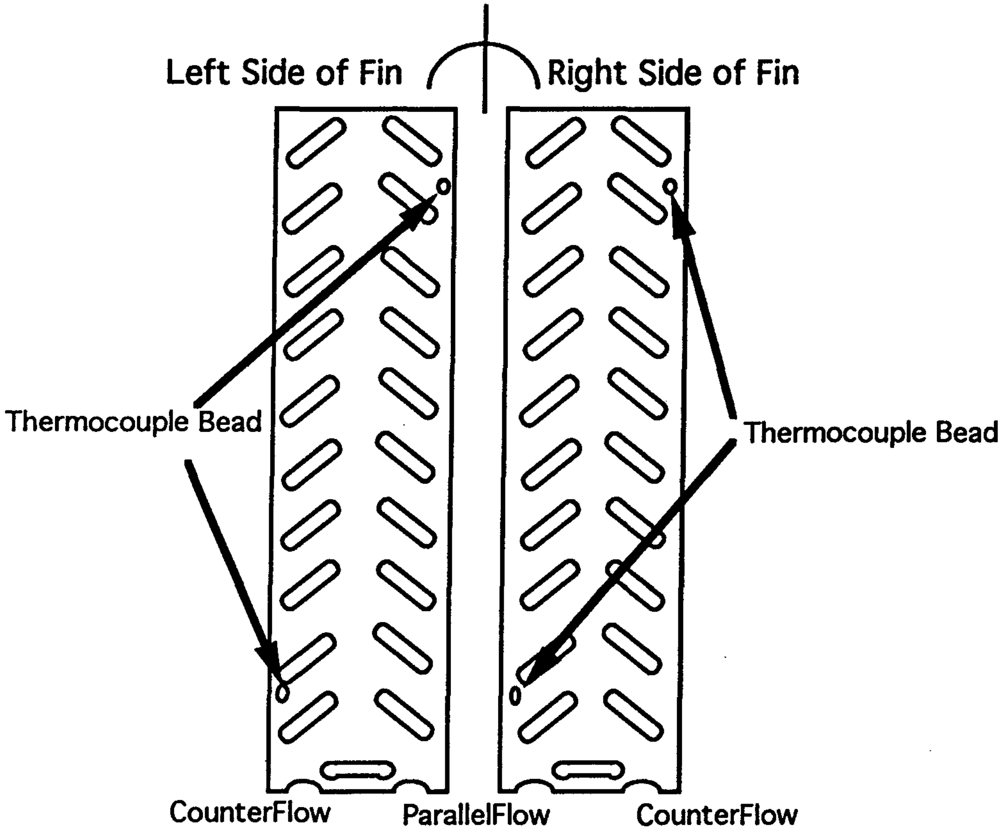

Figure G.1 Thermocouple placement on evaporator fin

G.2.2 Quasi-steady data

For detecting where dryout occurs within the evaporator, a quasi-steady data collecting approach was taken where initially the evaporator is run with a two-phase exit. Data collecting is started and the cabinet temperatures within the fresh food and freezer are increased slowly such that the thermal capacitance of the evaporator can be neglected. By increasing the fresh food and freezer cabinet, the superheat within the evaporator is increased. The results of the quasi-steady testing are shown in Figure G.2 and Figure G.3 where the surface fin temperature is plotted verses the amount of superheat seen in the evaporator.

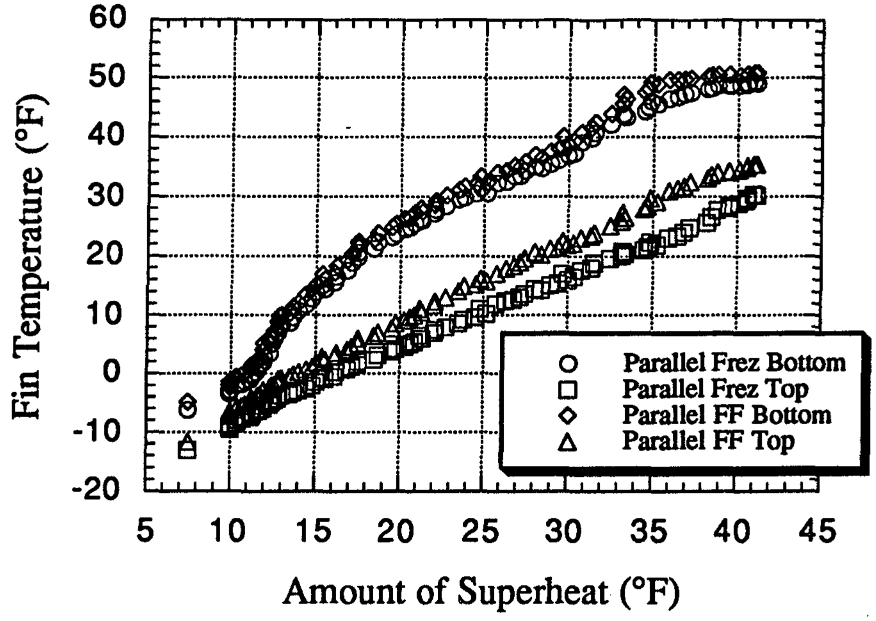

Figure G.2 Quasi-steady fin temperature on parallel side of evaporator

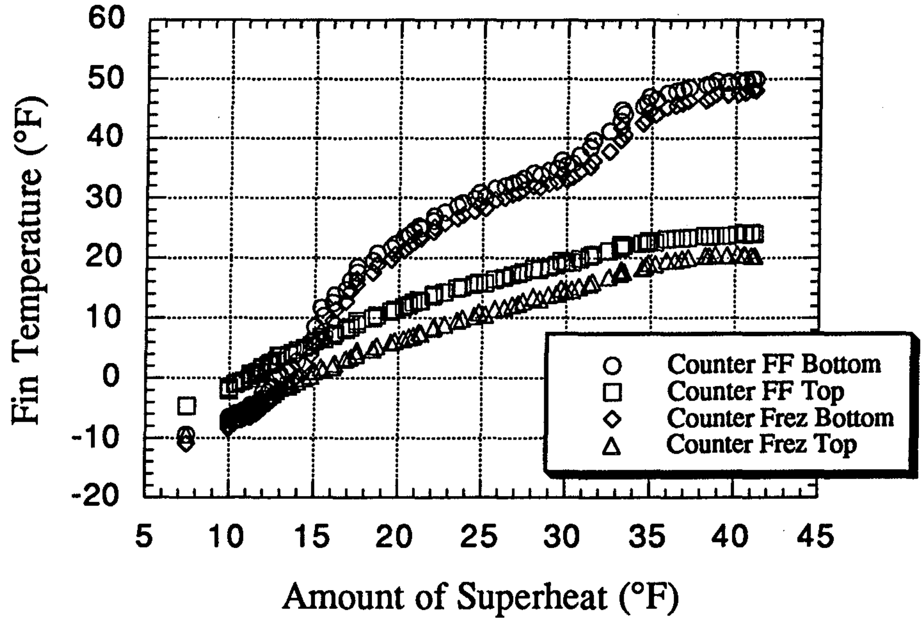

Figure G.3 Quasi-steady fin temperature on counterflow side of evaporator

The graphs above give good detail as to where dryout of the evaporator is occurring. From Figure G.2 which shows the bottom thermocouples on the parallel side, it can be seen that at about 12 degrees of superheat, the two thermocouples on the bottom start to experience a sudden increase in fin temperature as it starts to break away from the temperature readings of the top part of the evaporator. This suggests that already about 45% of the evaporator tube walls are "dry", seeing either superheated vapor or misty two-phase flow. From Figure G.3, it can be seen that the two bottom thermocouples on the counterflow side break away at around 15 degrees of superheat suggesting that already about 55% of the evaporator tubes are seeing misty or superheated flow.

G.3 Addition of fin conduction in evaporator model

In order to try to correct the model, the first model approach was to add fin conduction equations in the model to take account of the fact that the fins will try to approach a constant temperature. With fin conduction occurring, although the superheated portion of the evaporator has a small refrigerant-side convective heat transfer coefficient, the convective heat transfer from the air to surface in the superheated portion of the evaporator can remain large and the heat can then be transferred through conduction to the two-phase portion of the evaporator. Therefore, the refrigerant will evaporate faster in the two-phase section, and become superheated sooner. By adding fin conduction in the model, the superheated portion of the evaporator should grow at a larger rate, the same phenomenon observed qualitatively in the experiment. Figure G.4 shows the calculated superheated area fraction for steady state data taken at 4 different ambient conditions. As can be seen, fin conduction did allow the superheated area to grow faster as superheat was increased. From looking at the graph, at around 40 degrees of superheat is where half the evaporator becomes superheated vapor. This however does not correspond quantitatively with the experimental data. Apparently, the warming of the fins, observed above 15 °F of superheat, must result from dryout in the high quality regime. Another possible explanation is that the flow remains stratified at quality above 0.5, but the aluminum tube wall thickness is not adequate to overcome the effects of the greater than 90% void fraction. Recall that Chato and Wattelet's (1994) experiments were conducted in thicker copper tubes.

G.3.1 Refrigerant-side heat transfer correlation

To understand why the experimental data does not correlate well with the model results, we considered the possible impact of inaccuracies in the two-phase refrigerant heat transfer correlation.

The mass flux seen in the experimental refrigerator was anywhere from 20 - 30 klbm/ft^2-hr with a heat flux of about 300 Btu/ft^2-hr. Based on the mass flux seen in the evaporator, there should be a wavy or wavy-stratified flow occurring. Wattelet noted that he initially thought his correlation tended to overpredict the heat transfer coefficient at low mass flux because of loss of turbulence in the flow. Later he found out that it was not a loss of turbulence, but an effect of the stratification which caused a lower heat transfer coefficient which he tried to correct with a

Froude number dependent term. Looking at the data that Wattelet used to generate his correlation, it is apparent that none of his data points are close to the operating conditions that are seen in our experimental refrigerator. The lowest mass flux that Wattelet tested was at 38 klbm/ft^2-hr with a heat flux of 640 Btu/ft^2-hr and a saturation temperature of 41°F. Essentially we are extrapolating off of his correlation which might already be incorrectly predicting our heat transfer coefficient.

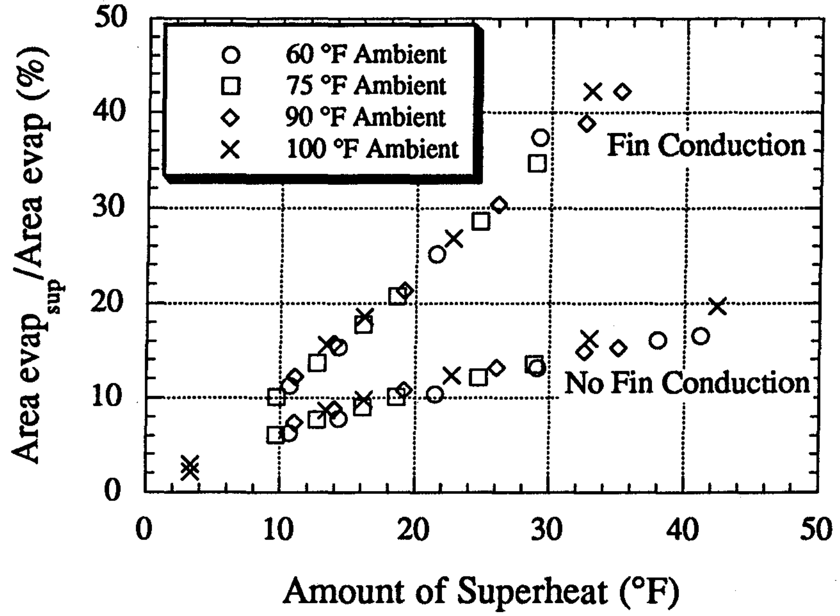

Figure G.4 Calculated superheated area fraction

If the two-phase refrigerant side heat transfer coefficient is overpredicted, then the model would overpredict the 2-phase area of the evaporator. Therefore, this would cause the model to incorrectly predict when half of the evaporator became superheated vapor.

A graph of Wattelet's correlation for a typical operating condition of 60°F ambient and 0°F and 40°F in the freezer and fresh food was analyzed in Figure G.5 over the evaporator quality range. As can be seen in the graph, the refrigerant-side heat transfer coefficient appears to increase by about 50 Btu/hr-ft^2-°F as the quality moves from 0.2 to 1. In Wattelet's thesis, his data of the heat transfer coefficient for his lowest mass flux (38 klbm/hr-ft^2) is seen to be flat and not sloped as his correlation yields in Figure G.6. Another approximation seen in Wattelet's correlation is when the refrigerant approaches quality 1. At quality of 1, the refrigerant is at a saturated vapor; therefore the heat transfer coefficient is small because there is now vapor-to-vapor heat transfer. In Wattelet's experimental results, he only had data up to a quality of 0.85. In order to smooth out the heat transfer coefficient as it transitions with the vapor heat transfer coefficient, the correlation is used only up to 0.95 quality. After 0.95 quality, a linear interpolation to the Gnielinski correlation (Incropera and DeWitt, 1990) for vapor-to-vapor heat transfer is used to get from quality 0.95 to 1.

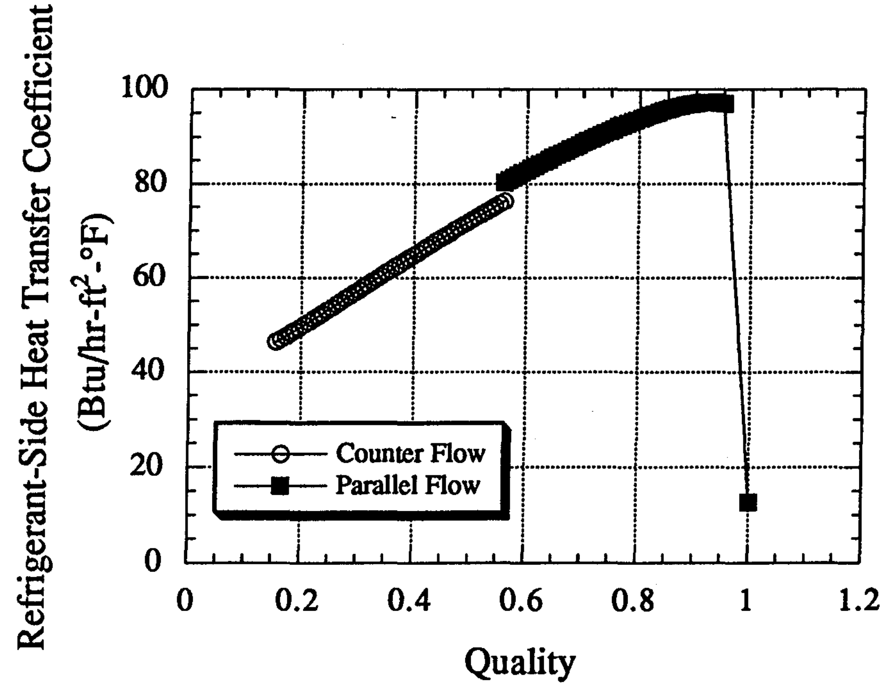

Figure G.5 Wattelet's correlation plotted for a typical evaporator running condition

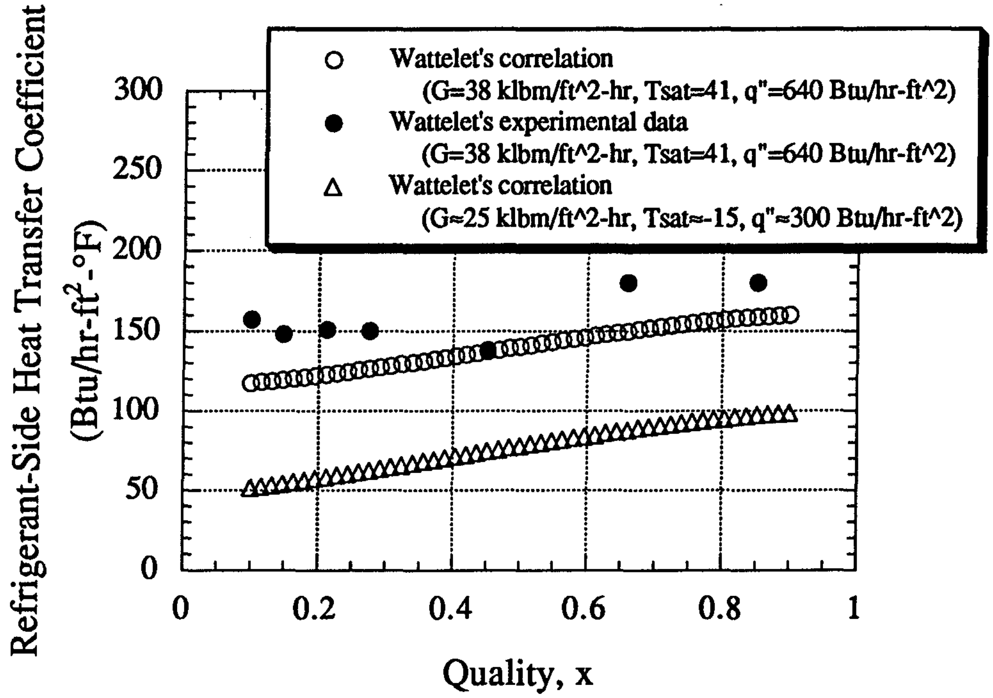

Figure G.6 Wattelet's experimental data and correlation result for lowest mass flux

G.3.2 Calculated temperature profile of evaporator

Additional temperature profiles were calculated for the evaporator when both fin conduction and no fin conduction was considered. For each of the three zones in the evaporator, a one-dimensional heat transfer gradient is set up so only the surface temperature at the midpoints of the three zones could be calculated. Also, the refrigerant-side heat transfer coefficient for the three zones is an average value where the value obtained in the two-phase zone is calculated from a correlation developed by Wattelet and Chato (1994) and the average refrigerant-side heat transfer coefficient in the superheated zone is calculated using Gnielinski correlation (Incropera and DeWitt, 1990). Looking at two different superheating values, Figure G.7-G.12 show the calculated temperature profile with and without fin conduction and the actual fin temperature profile as seen from experimental data. The data are plotted against the area of the evaporator, so for the two air streams which start at the middle of the evaporator, there is both a counterflow and a parallel flow configuration with the refrigerant. The graph showing the actual fin temperatures shows that there appears to be a desuperheating region occurring in the parallel flow section of the heat exchanger.

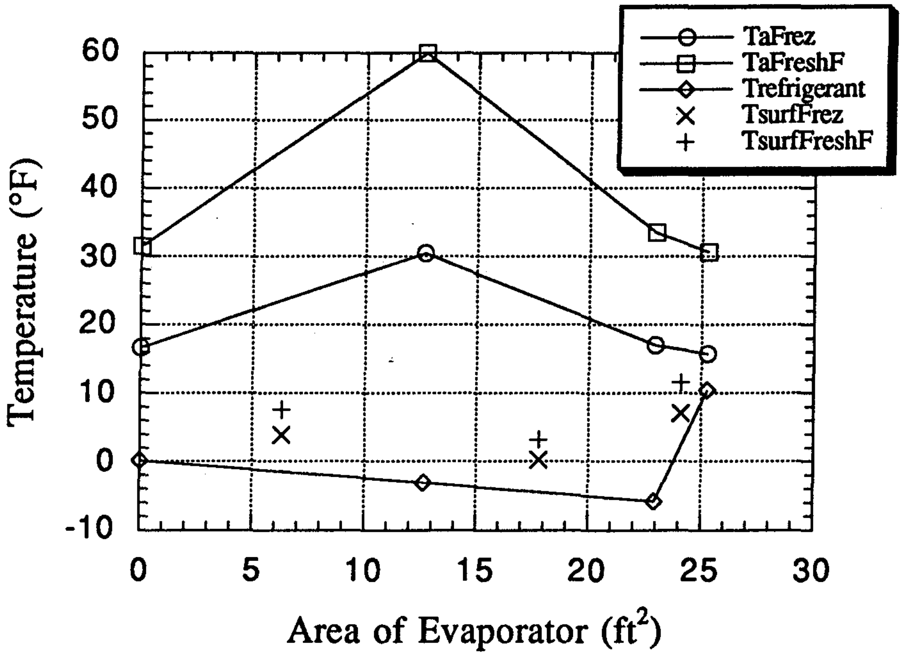

Figure G.7 Ambient temperature 100°F with 16 °F superheat (no fin conduction)

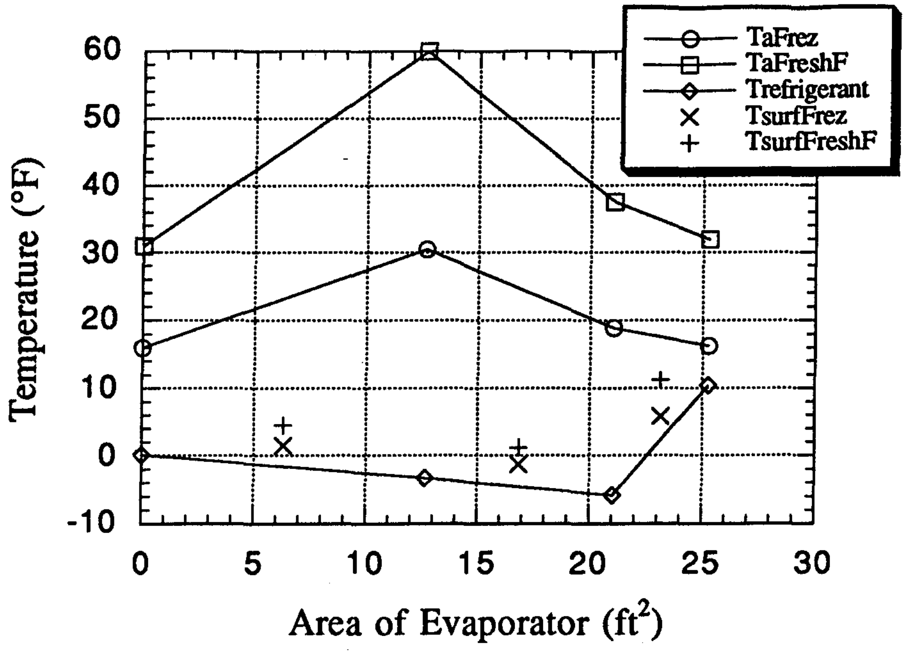

Figure G.8 Ambient temperature 100°F with 16 °F superheat (fin conduction)

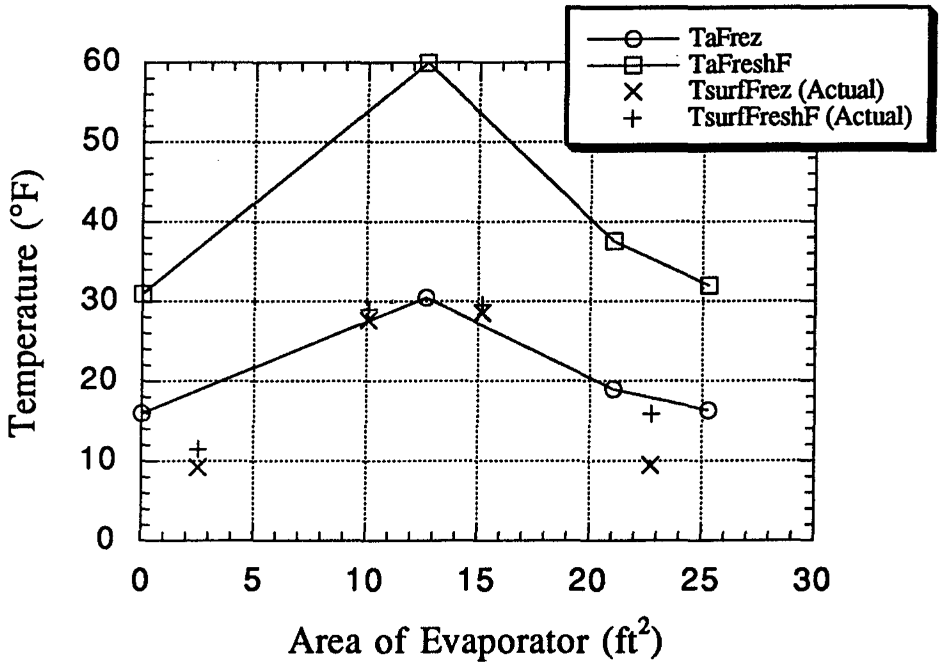

Figure G.9 Ambient temperature 100°F with 16 °F superheat (actual fin temp.)

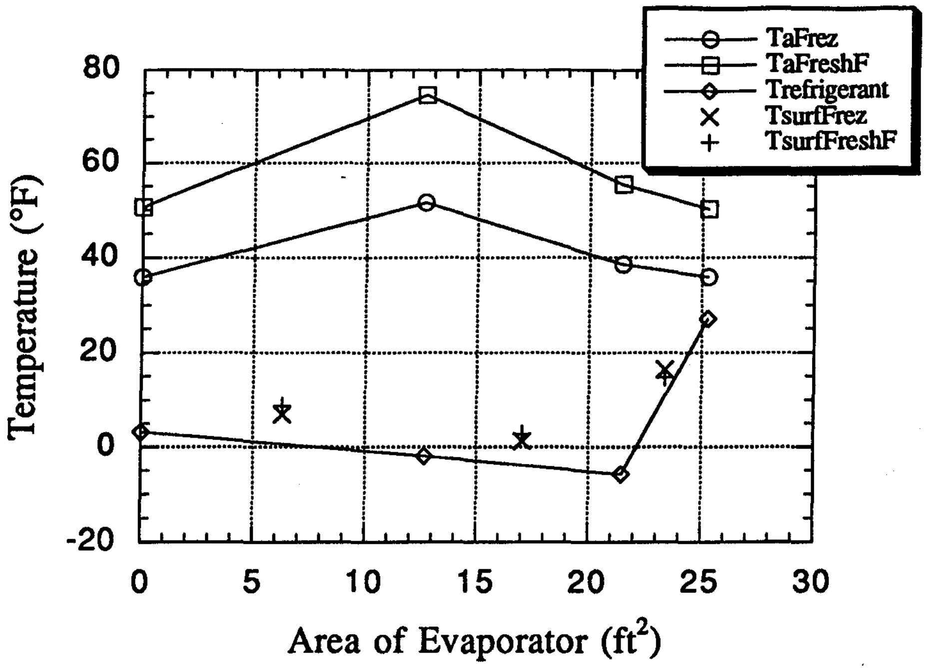

Figure G.10 Ambient temperature 100°F with 33 °F superheat (no fin conduction)

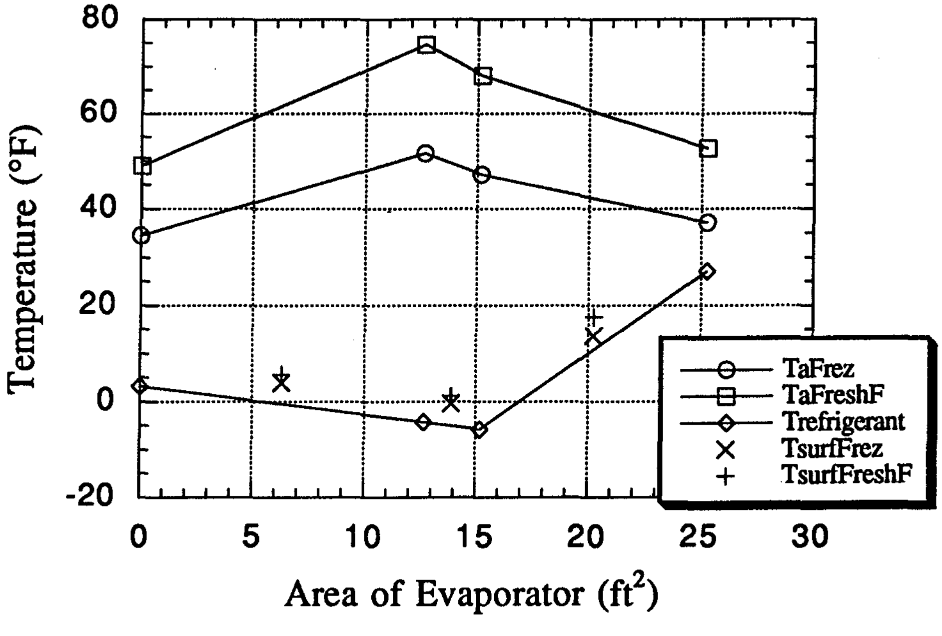

Figure G.11 Ambient temperature 100°F with 33 °F superheat (fin conduction)

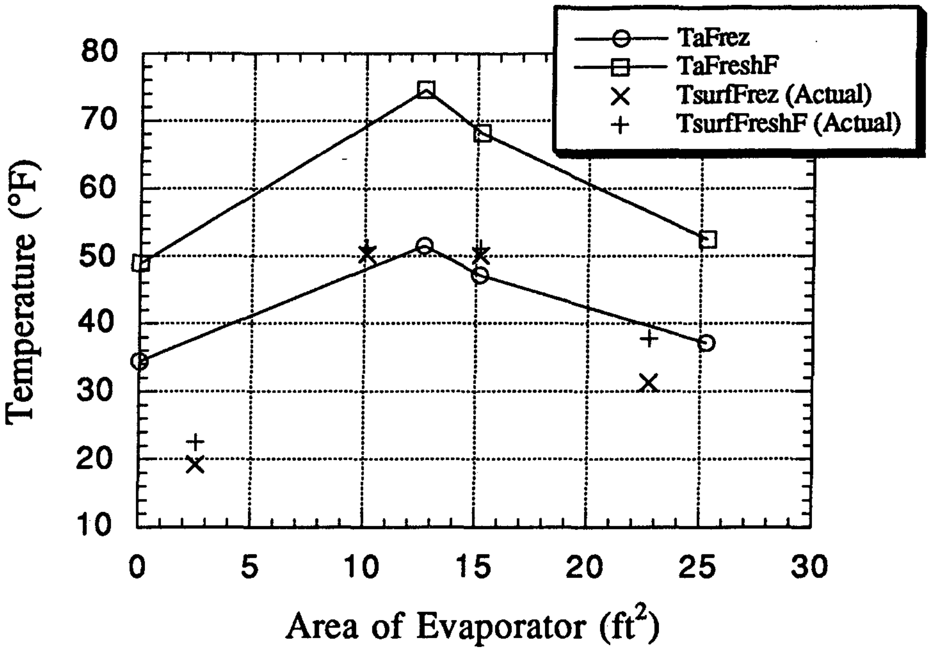

Figure G.12 Ambient temperature 100°F with 33 °F superheat (actual fin temp.)

G.3.3 Analytical model of fin conduction

Currently it appears that the evaporator model might be too crude and therefore cannot predict the correct performance of the experimental evaporator. A more complex model for the evaporator would be to write the log mean temperature difference between the air temperature, fin surface temperature, and refrigerant temperature for each tube separately. This would require the evaporator model to be divided into 42 zones which would require about 252 simultaneous equations to solve. A simpler analysis was first performed on a typical evaporator fin to see if the measured amount of heat removed could be achieved if only half of the tubes (the counterflow region) experienced 2-phase flow. As shown in section G.3.2, the experimental data showed 15 degrees of superheat in cases where about half the evaporator was 2-phase and half the evaporator was superheated. This analysis (of fins only) assumed that the refrigerant exits as saturated vapor at the bottom of the evaporator. The parallel flow tubes of the evaporator are removed and the fin is divided into 21 zones as shown below in Figure G.13.

Since the two-phase zone is at a constant temperature, it is assumed that the dashed vertical line in the figure above represents the point on the fin where the temperature is at the saturation temperature of the refrigerant. This assumption assumes that the contact resistance between the fin and tube is small, and that refrigerant-side resistance is negligible in the 2-phase region. Starting with the evaporator inlet air, the heat transfer rate equations and air side energy balances are then solved 21 times for the 21 zones for two data points where there was 16 °F and

33 °F of superheat. A calculated fin efficiency of 69% was used along with a constant air-side heat transfer coefficient of 1.58 Btu/hr-ft^2-°F which was estimated in Appendix D.

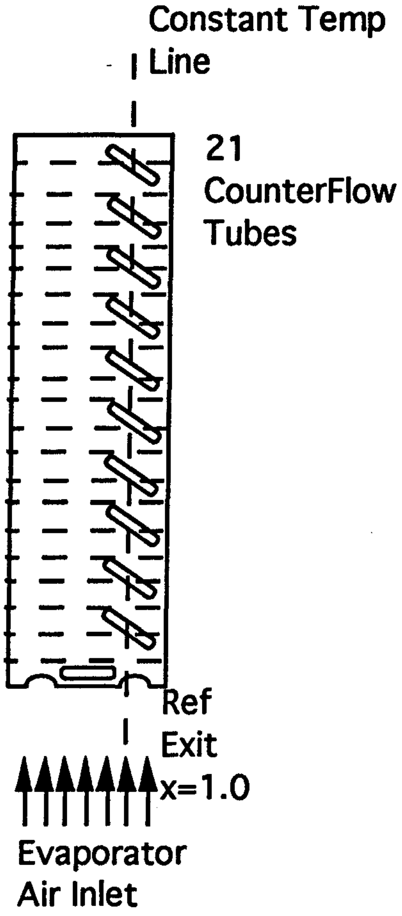

Figure G.13 Schematic of evaporator fin model

For the 16 °F superheat, evaporator capacity was 856 Btu/hr. Evaporator capacity was determined from knowing the amount of heat leak into the refrigerator compartment and measuring the amount of heat dissipated by the compartment heaters. Solving the evaporator fin model described above showed that the fins alone were able to remove 836 Btu/hr, with no assistance from the tubes in the parallel-flow region. This result is consistent with the evaporator experiments which suggested that the saturated vapor point can exist at half the evaporator when the superheat is around 15 °F. Although the fin model did not consider the superheated zone of the evaporator, results show that the superheat zone of the evaporator only removes around 20 to 30 Btu/hr of heat. This result added to the evaporator fin model result shows that the evaporator should be able to perform with half of the tubes missing.

For the case of 33 °F superheat, evaporator capacity was 878 Btu/hr. Solving the fin model above showed that the evaporator was capable of removing 1289 Btu/hr if the counterflow half of the evaporator was all two-phase. Repeated solution of the model showed that the counterflow section of the evaporator could be "shortened" by 8 zones, and that the remaining 13 zones were able to remove 864 Btu/hr of heat. This is approximately equal to the measured evaporator capacity of 878 Btu/hr. This suggests that the bottom 1/3 of the evaporator could be unused and ineffective, which is consistent with measurements discussed in Section G.3.2 when thermocouples were mounted on the bottom of the evaporator fin. A summary of the results are shown in Table G.1.

Table G.1 Results of evaporator fin model

	16°F Superheat	33°F Superheat	33°F Superheat (minus 8 tubes)
Qevap measured	856 Btu/hr	878 Btu/hr	878 Btu/hr
Qevap from fins	839 Btu/hr	1289 Btu/hr	864 Btu/hr

This approach to modeling the evaporator suggests that the refrigerant becomes superheated in the counterflow section, which is consistent with the data. Maximum superheat would occur at the 50% point in the tubes, near the leading edge of the fins. Then the refrigerant would desuperheat as it progressed along the parallel flow path and passed by the coldest fins. Since the measured superheat is actually the "desuperheated value", it gave misleading results in the preceding three-zone model. A graphical description is shown in Figure G.14 below.

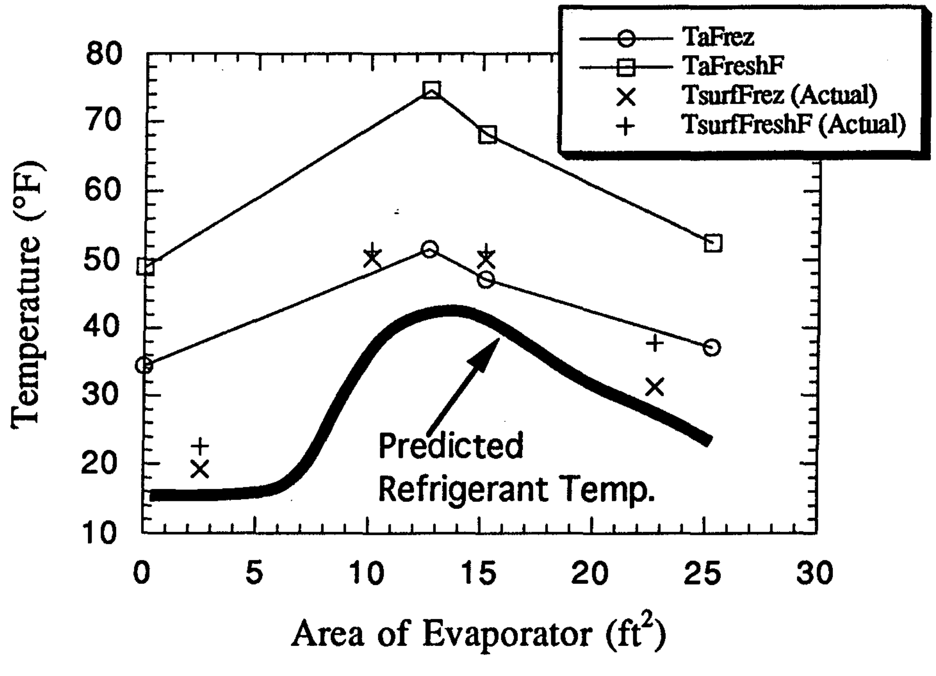

Figure G.14 Predicted refrigerant path through evaporator at high superheat

G.4 Four-zone model

The graph of the measured fin temperatures show for having 15 °F of superheat, half of the evaporator exists as superheated vapor. This experimental result suggests that the three-zone modeling performed in the evaporator parameter study might be inadequate and a four-zone model needs to be used for the high superheat cases. The four zones for the heat exchanger would consist of one 2-phase zone and 3 superheated zones as shown in Figure G.15. The 2-phase refrigerant would evaporate completely in the downward (counterflow) section of the heat exchanger. Starting at zone 2, the refrigerant would begin superheating and continue through zone 3. Starting at zone 4, there will be a desuperheating region as fin conduction occurs with the colder 2-phase zone to cool the refrigerant before it exits the heat exchanger. The four-zone model was written in the same manner as the three-zone model explained in Appendix D. For the four-zone model, fin conduction can occur between zone 1 and 2, zone 1 and 4, zone 3 and 2, and zone 3 and 4.

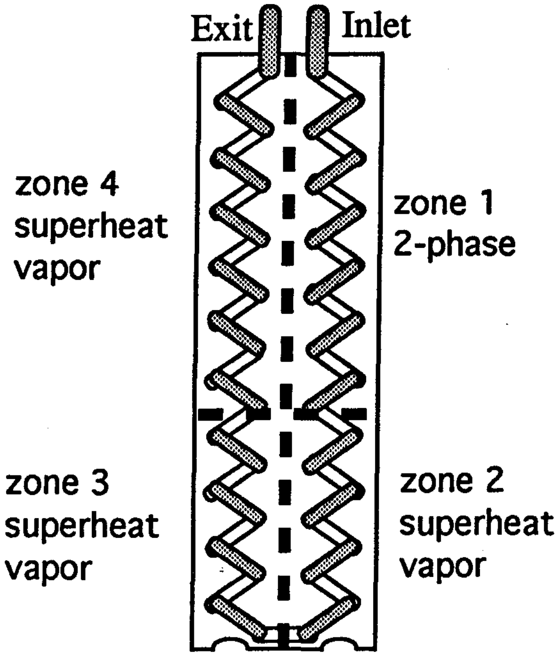

Figure G.15 Four-zone modeling schematic

G.4.1 Air-side heat transfer coefficient

Testing of similar Brazeway evaporators in the ACRC was performed by Korte (1997) for condensate retention. Analysis of his data for face velocities similar to what is seen in the experimental refrigerator show that his calculated air-side heat transfer coefficient is close to 1.6 Btu/hr-ft^2-°F. This result helps support the conclusion drawn in Appendix D using data having less than 15 degrees of measured superheat in the evaporator air-side heat transfer estimation.

The three-zone model used for this parameter estimation is not expected to be reliable for data having more than 15 °F of superheat.

G.4.2 Influences of free convection

One possible cause of the observed degradation in the air-side heat transfer coefficient (in highly superheated cases) is due to interaction between forced and free convection. The driving force for free convection is the maximum temperature difference between the fin surface temperature and the air temperature, which increases as superheat in the evaporator increases. Therefore, if free convection was a factor in the evaporator, then it would be expected that the air-side heat transfer coefficient would decrease as the maximum temperature difference between the air and fin surface temperature increased which is what is seen in the data. The fin surface in the 2-phase zone is approximately the same temperature as the refrigerant and the resulting downward buoyancy force may interfere with the upward forced convection. A quick analysis of the Grashoff number based on fin spacing divided by the Reynolds number square based on fin spacing shows that the ratio is close to 0.006. Since this ratio is much less than 1, there is no interaction of free convection and the evaporator is dominated by forced convection only.

G.4.3 Contact resistance and fin conductivity

The three-zone and four-zone evaporator models were analyzed together. Since it has been confirmed that the air-side resistance is around 1.6 Btu/hr-ft^2-°F, this information was input into the model and the exit refrigerant temperature was calculated and compared with the measured data. The results showed that the three-zone model breaks down after 15 degrees of measured superheat exists in the evaporator. At 15 degrees of measured superheat, the saturated vapor point has been pushed up above the mid-point of the evaporator. At this point, the new four-zone model was implemented. The remaining data of higher superheat was calculated using the four-zone model. Comparison of the calculated and measured exit refrigerant temperature showed that the three-zone model tended to overpredict the amount of superheat at the evaporator exit while the four-zone model tended to underpredict the amount of superheat.

The fin conduction equations in the evaporator model are known to be incorrect. In the evaporator model, the fin conduction equations are written implicitly assuming a linear distribution between the nodal points of each zone. In reality, there is actually less heat conduction occurring between the fins than what is calculated because the temperature distribution is flattened by the heat transfer from the air to the fin between the zones. Therefore the temperature remains flat in the higher temperature zone and then falls off suddenly as it approaches the tube on the colder side of the fin. Another possible error in the evaporator model is the assumption that no contact resistance is occurring between the evaporator fin and the refrigerant tubing. Results from Davis, Jacobi, and Hrnjak (1996) had found that the contact resistance in a similarly circuited Peerless evaporator was about 20% of the total resistance.

Davis was able to make some conclusions about contact resistance since she had two similar plain fin evaporators with one having fins brazed to the tubing. However, other research cited by Davis found contact resistance to be relatively very small and negligible.

The evaporator model was re-examined to see whether lowering fin conduction and adding contact resistance could improve estimates of exit superheat in the three and four-zone model. For the three-zone model, it was already seen that using a constant air-side heat transfer coefficient of 1.6 Btu/hr-ft^2-°F causes the model to "break-down" after 15 degrees of measured superheat. This is the same result seen experimentally when thermocouples were mounted on the evaporator fin. What the model also shows is that the predicted superheat at the evaporator exit is higher than that measured. The effects of adding contact resistance causes the surface temperatures of the fins to become warmer. Since the fin temperatures are warmer, the 2-phase area in the evaporator must increase causing a reduction in the superheated area and a reduction in the amount of superheat. Lowering the amount of fin conduction occurring showed to cause less heat to be transferred from the warmer superheated section to the colder 2-phase section. Since less heat is being transferred out of the superheated fin, that heat must be transferred to the refrigerant which causes an increase in the superheat. While the addition of contact resistance and lowering the fin conduction appear to have the opposite effect on the prediction of the superheat, it is seen that the addition of contact resistance has the dominant effect and so a combination of the two will ultimately cause the predicted amount of superheat to decrease. This would improve the prediction of the three-zone model since it overpredicts the amount of superheat.

For the four-zone model, the amount of superheat predicted by the model is less than what is actually measured. Increasing contact resistance and reducing the amount of fin conduction showed to increase the fin surface temperatures in both cases. The warmer fin temperature causes less desuperheating to occur in zone 4 resulting in a increase in predicted superheat which tends to improve the model's predictions

G.5 Conclusion

For the evaporator model used in the RFSIM model and in the parameter estimation of the air side heat transfer coefficient, it was noted that at high degrees of superheat the model predicts poorly the location of the saturated vapor point. At around 12 to 15 degrees superheat, the dryout point is somewhere close to half of the evaporator, as indicated by thermocouples attached to fins. However the three-zone model, even accounting for inter-zone conduction through the fins, predicts that half the evaporator will not become superheated until the exit superheat is 40 °F. Using the fin model described in Section G.3.3, it was shown that indeed half of the evaporator could conceivably be superheated vapor after 15 degrees of superheat, due to horizontal conduction through the fins. This is consistent with the results seen using thermocouples on the evaporator fin.

The addition of contact resistance and a correction on the fin conduction equation has been shown to improve the evaporator model's prediction of an air-side heat transfer coefficient close to 1.6 Btu/hr-ft^2-°F. A three-zone evaporator model is valid up to 15 °F of superheat, and the four-zone model is appropriate for the more highly superheated data points. All predict an air-side heat transfer coefficient near 1.6 Btu/hr-ft^2-°F. This has verified our earlier assumption that the correct air-side heat transfer coefficient can be estimated from a three-zone model for the low superheat data where less than 15 degrees of superheat is seen in the evaporator.

Additional error in the evaporator model might have occurred from the refrigerant-side heat transfer coefficient correlation used in the model. The operating conditions seen in the experimental refrigerator have less mass flux and heat flux than the data used to develop the correlation. Therefore, an extrapolation error might be occurring. Finally, there is also a question about the magnitude of refrigerant-side heat transfer coefficient as a quality of one is approached. In the data that Wattelet used to devop his correlation, all of his data points had qualities less than 0.90.

Appendix H

Clogging of Capillary Tube and Diameter Measurement

H.1 Verification of capillary tube clogging

After installing refrigerant-side instrumentation in the Amana experimental refrigerator, it was noticed that evaporator capacity had declined from pre-instrumentation experiments. For a typical operating condition of 5°F in the freezer and 45°F in the fresh food, pre-instrumentation showed that a total heater power of about 160 W needed to be inputted into the cabinets in order for steady state to be achieved. After instrumentation, it was noted that only about 130 W was now needed. To understand what could possibly have happened, it was noted that a reduction in evaporator capacity could be caused by a reduction of the refrigerant mass flow occurring somewhere in the refrigerant tubing.

Steady state data was taken at 60 and 75 degree ambient conditions where it was known that the condenser and evaporator had subcooling and superheat. From the data taken, rough parameter estimates were done for both volumetric flow rates and air side heat transfer coefficients of the evaporator and condenser. A UA value was estimated for the post condenser loop and the compressor shell. With rough parameter estimates performed, the RFSIM model was used to see if the model could predict the same behavior as the actual data. Results of running the RFSIM model showed no agreement with the actual data. An analysis of the RFSIM results showed that the calculated mass flow rate of the refrigerant was about 5 lbm/hr higher than what the data indicated. Since the capillary tube-suction line heat exchanger model could be run separately, an analysis was first done on the ct-slhx to see if there were any problems with that subsystem. From actual data, inlet pressure and temperature to the capillary tube were measured so those results could be inputted into the ct-slhx model along with the inlet conditions of the suction line. From the cabinet load calorimetry, the mass flow rate of the refrigerant was known and could be compared with the mass flow rate calculated from the ct-slhx model. The results of the ct-slhx model showed that the predicted mass flow rate was about double from what was measured experimentally, as shown below in Figure H.1.

It was already known that the capillary tube model underpredicts the mass flow rate as shown by Liu and Bullard (1997), but these results showed an overprediction. One possible error in the model is in the nominal diameter of the capillary tube which was 0.038 in. as stated by Amana. Previous analysis has shown that the ct-slhx model is very sensitive to the capillary tube diameter (Woodall and Bullard, 1997 and Liu and Bullard, 1997). Since the ct-slhx model uses the ACRC Newton-Raphson solver, the ct-slhx model supports parameter swapping as described by Goodson and Bullard (1994). Therefore, the model could be rerun to solve for the diameter, given the mass flow rate. Decreasing the diameter of the capillary tube would ultimately lower the mass flow, but the results showed that the diameter needed to be around 0.024 in. instead of

0.038 in. When the capillary diameter is changed to around 0.024 in. in the RFSIM model, the predictions for the pressure and temperatures in the model start to approach the results seen in the actual data.

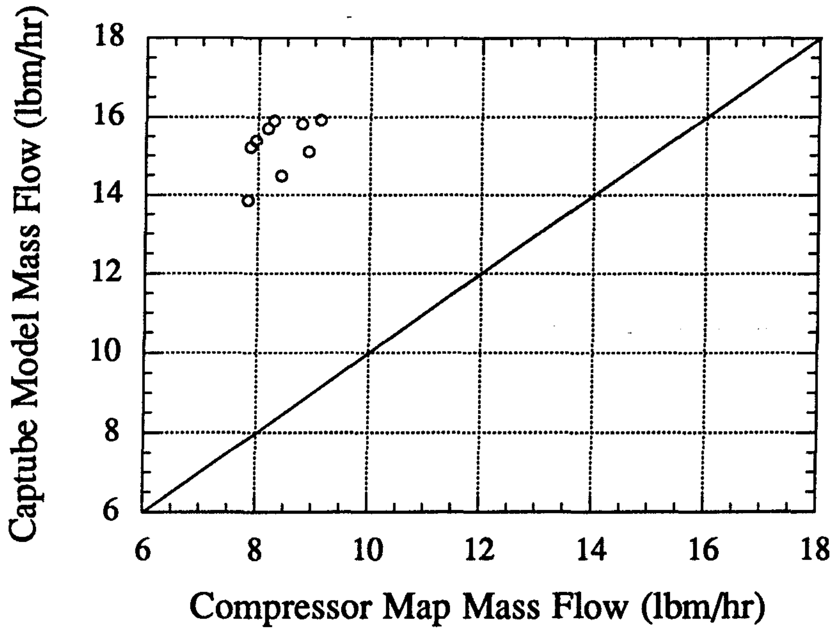

Figure H.1 Mass flow rate calculated by CTSLHX model

It is very unlikely that a manufacturing error could have caused the diameter of the capillary to error by 37%, so these results confirmed that the capillary tube was clogged. The question that needs to be answered now is where and how the clog occurred. Figure H.2 shows a temperature profile for one of the data point conditions as predicted by the ct-slhx model in which only the inlet temperatures and pressures are specified for both the capillary tube and suction line. From looking at the data, nothing could be said for the prediction of the capillary tube temperature because the exit temperature measured on the experimental refrigerator is really in the evaporator inlet, downstream of the capillary tube exit. At the capillary tube exit, there is an additional temperature drop from what the ct-slhx model predicts for the capillary tube exit (due to the expansion of the refrigerant from the capillary tube diameter to the evaporator diameter). There can, however, be an analysis made on the suction line temperature since this temperature is measured on the experimental refrigerator. The model as shown below predicts the exit of the suction line to be about 10 degrees colder than the inlet temperature of the capillary tube. Results from the experimental refrigerator showed that the measured suction line exit temperature approaches the same temperature as the inlet capillary tube temperature.

From the graph below, the model predicts that the flash point is occurring near the inlet of the heat exchanger region. However the experimental data suggests that the flash point must occur at some point farther downstream. If this were true, the capillary tube temperature in the liquid region downstream of the heat exchanger inlet will be higher than what the model predicts. This would create a larger delta T between the capillary tube and suction line, allowing the suction line temperature to approach the same temperature as the capillary tube inlet.

Obviously this result shows that the clogging in the capillary tube must have occurred towards the exit of the capillary tube and not near the inlet. If the capillary tube were clogged at the inlet, the flash point would have occurred in the inlet section of the capillary tube and therefore the actual exit temperature of the suction line should be colder than what is predicted by the ct-slhx model.

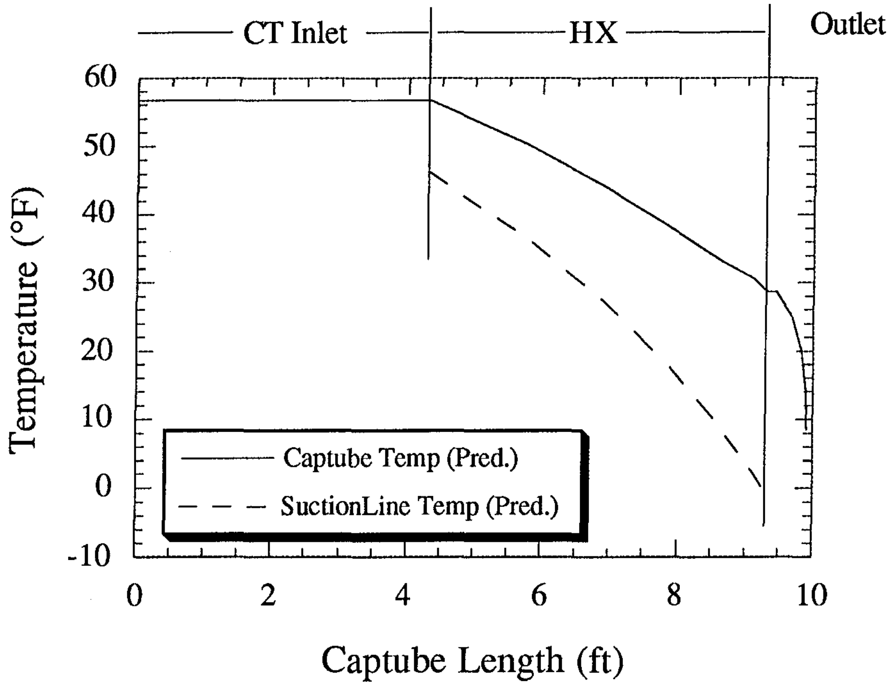

Figure H.2 Capillary tube-suction line heat exchanger model temperature profile

Now that it is known where the capillary tube exit is clogged, a question as to why and how the clogging occurred needed to be answered. Research into the literature of polyol ester oil shows that polyol ester oil is more hygroscopic than mineral oil (Sanvordenker, 1991). To be hygroscopic means to have the ability to absorb moisture from the atmosphere. Apparently during the refrigerator instrumentation procedure, the refrigerant tubing line was cut for the installation of immersion thermocouples and pressure transducers, and the system was open for roughly one month. Since the refrigerant tubing was not adequately sealed to prevent air from entering; tape only was used to prevent dirt from entering the tube. Since the compressor was not totally sealed from the atmospheric air, moisture from the air dissolved in the polyol ester oil. Once instrumentation was completed, the filter dryer was apparently unable to remove the water trapped in the oil which then froze in the capillary tube as the temperature dropped to below freezing temperatures. This is consistent in our conclusion that the capillary tube was clogged near the exit where the temperature is the coldest.

H.2 Replacement of capillary tube-suction line heat exchanger

Once it was known that the capillary tube is indeed clogged, a replacement ct-slhx had to be installed into the system and the oil removed from the compressor. Since removing all of the oil from the compressor would be a long time-consuming process, it was decided that the installation of a new compressor would be easier. Before a new ct-slhx was to be installed, testing was performed to determine the actual diameter of the new capillary tube since it is known that small error in the capillary tube diameter can greatly affect the results of the simulation model. Water flow tests as described by Liu and Bullard (1997) were performed at 3 different head heights. The diameter was determined from the laminar pressure drop equations. The diameter was determined to be 0.0366 in. with Figure H.3 showing the calculated and measured water mass at the estimated capillary tube diameter.

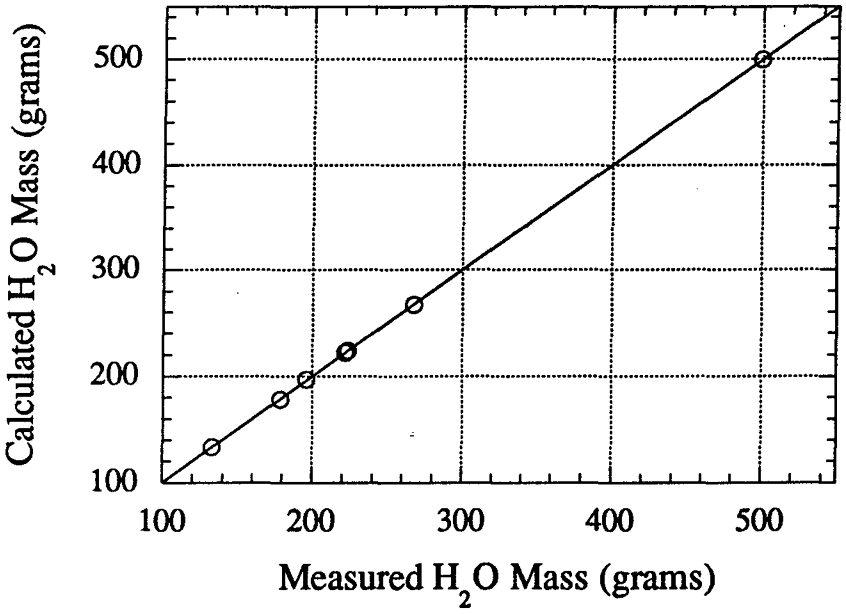

Figure H.3 Water flow test for determining capillary tube diameter

H.3 Conclusions

Whenever the refrigerator system is cut open, great care needs to be taken to seal the compressor away from the atmospheric air. Previous refrigerators used a mineral oil which, not hygroscopic means there is no need to seal the compressor. The replacement of the capillary tube has also allowed us to calculate more accurately the actual diameter which will be important when the simulation model is run. By accurately knowing the diameter of the capillary tube, one possible mode of error in the simulation model has been reduced.

Appendix I

2-Speed Compressor Calorimetry

I.1 Introduction

The RV800 two-speed compressor from Americold came supplied with no compressor maps to characterize how the mass flow and power varied with the evaporating and condensing temperature. It was also unknown at what speed the compressor operated and how the control box switched between two different speeds. The first step after installing the new compressor into the current Amana refrigerator was to generate accurate compressor maps. Compressor maps currently used in the RFSIM model employ a bi-quadratic curve fit of nine parameters with the condensing and evaporating temperature. Once compressor maps were generated, testing was performed with accelerometers mounted on the compressor shell to measure the compressor speed. Setting different cabinet temperatures and ambient temperatures for the refrigerator allowed for a wide variety of different loading conditions.

I.2 Compressor and power map

I.2.1 Measuring mass flow rate and power

Power transducers measured power supplied to each heat exchanger fan and to the total system for different condensing and evaporating temperatures. Mass flow measurements, however, were not easily obtainable since there are no mass flow meters connected to the refrigerator system. In order to determine the refrigerant mass flow, an energy balance was performed across the system boundary defined by the compressor inlet and the capillary tube inlet. Since the heat transfer occurring between the capillary tube-suction line heat exchanger is internal in this control volume, the change in energy between these two points is equal to the evaporating capacity. Evaporating capacity can be calculated since cabinet conductances for the freezer and fresh food compartments have been estimated (see Appendix B) and the exact amount of steady state heating power is measured. However, this energy balance for calculating mass flow rate does require that the refrigerant state at the compressor inlet and capillary tube inlet be known. Since the compressor inlet is always vapor, its pressure and temperature is easily measured. The condenser exit can be running either two-phase or liquid which means the capillary tube inlet runs either two-phase or subcooled. The mass flow calculation requires that the capillary tube inlet be subcooled. However, a subcooled condenser exit or a subcooled capillary tube inlet could not be achieved at normal operating conditions. One of the reasons why the refrigerator might have been designed for a two-phase condenser exit is due to the extraordinarily long liquid line known as the post condenser loop. The post condenser loop is used to prevent moisture build-up on the gasket closing by running the hot refrigerant from the condenser outlet to the front of the refrigerator before entering the capillary tube. The current liquid line is about 14 feet longer than one without a post condenser loop. If the condenser were subcooled during typical loading conditions, then there would be liquid running throughout the post condenser loop which might end up starving other parts of the system from refrigerant.

I.2.2 Obtaining capillary tube inlet subcooling

In order to get sufficient capillary tube inlet subcooling in the experimental refrigerator for the calculation of the mass flow rate, it was necessary to over-charge the system. A balance had to be achieved in overcharging the system. If too much refrigerant were added to the system, then the evaporator would overfill and start pushing two-phase refrigerant into the compressor. This is harmful to the compressor since there is no accumulator located to prevent liquid from entering the compressor. This would also make our energy balance ineffective since the enthalpy state at the compressor inlet needs to be known through temperature and pressure measurements. Since not enough subcooling could be achieved by overcharging the system, an additional fan was added at the condenser in order to increase its air-side heat transfer coefficient. Compressor inlet vapor and capillary tube inlet subcooling was finally achieved after the system was overcharged and an additional condenser fan was used. Since the compartment temperatures for the subcooled points were relatively high when compared with the ambient temperature, data logging was very limited due to power constraints of the compartment heaters.

A total of 16 data points were obtained for the compressor at each speed at the four ambient temperature of 50 °F, 60 °F, 75 °F, and 90 °F. Re-analyzing the data shows that the condensing and evaporating temperatures do not change much as the compartment temperatures are changed for a given ambient temperature. Therefore the actual 16 data points look like 4 data points at the four ambient temperature since the data points overlap each other. These points yield a bi-quadratic curve fit that accurately characterized the mass flow and power in the range that the data was obtained. However, extrapolating the polynomial was very inaccurate at normal operating conditions where the evaporating temperature is lower than those at which the overcharged system operated.

I.3.3 Using ideal compressor model

In order to get more mass flow data in the condensing and evaporating temperature range seen when the refrigerator operates with the factory recommended charge, the mass flow calculation for an ideal compressor was examined (Stoecker and Jones, 1986). A factor, C, was placed on the mass flow calculation to account for the inefficiency of the real compressor as shown in Equation I.1. Note that C = 1 corresponds to the mass flow that the ideal compressor would pump in the absence of leakage or blow-by losses.

$$\dot{m} = C \cdot \frac{V_{disp}}{\upsilon_{suc}} \left[1 - \frac{m}{100} \left(\frac{\upsilon_{suc}}{\upsilon_{dis}} - 1 \right) \right] \qquad (I.1)$$

For the current subcooled data taken where the actual mass flow is known, equation I.1 was used to estimate the value of C and m for both the 2400 and 3600 rpm speed. Once these parameters are known, they are applied to actual data taken on the factory charged system. This will enable more mass flow data to be obtained which can then be used to produce the mass flow map. Since the power of the compressor is measured directly from the power transducer, the power map parameters could easily be resolved with data taken from the overcharged and factory charged system.

Altogether there were 25 and 27 data points used in making the mass flow and power map for the 2400 rpm and 3600 rpm speed respectively. The limits of condensing and evaporating temperatures for the compressor maps will be 70 - 120 °F condensing and -25 - 5 °F evaporating for the 2400 rpm speed and 70 - 120 °F condensing and -30 - 0 °F evaporating for the 3600 rpm speed. Figure I.1 through I.4 show the mass flow and power maps for the 2400 and 3600 rpm compressor.

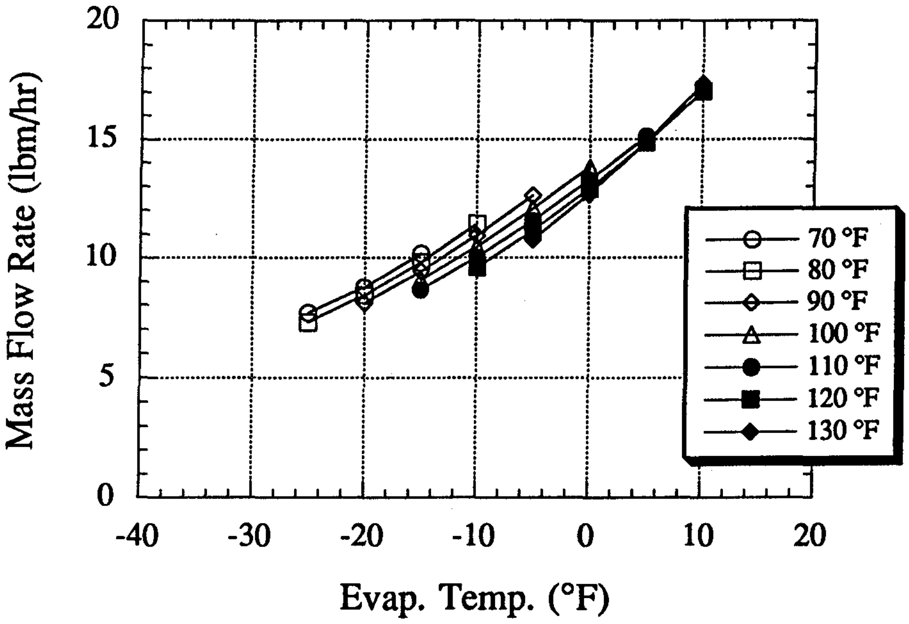

Figure I.1 2400 rpm mass flow map

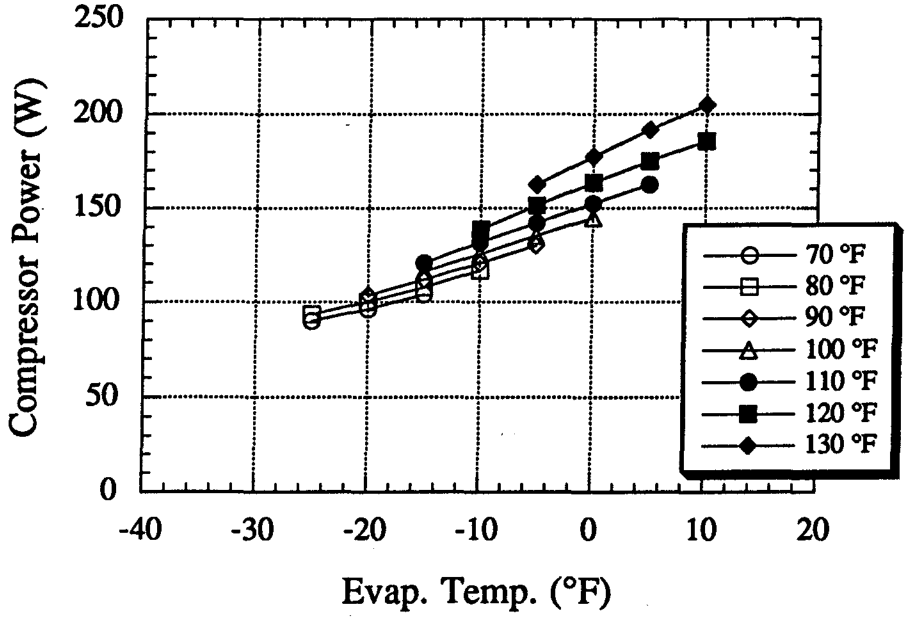

Figure I.2 2400 rpm power map

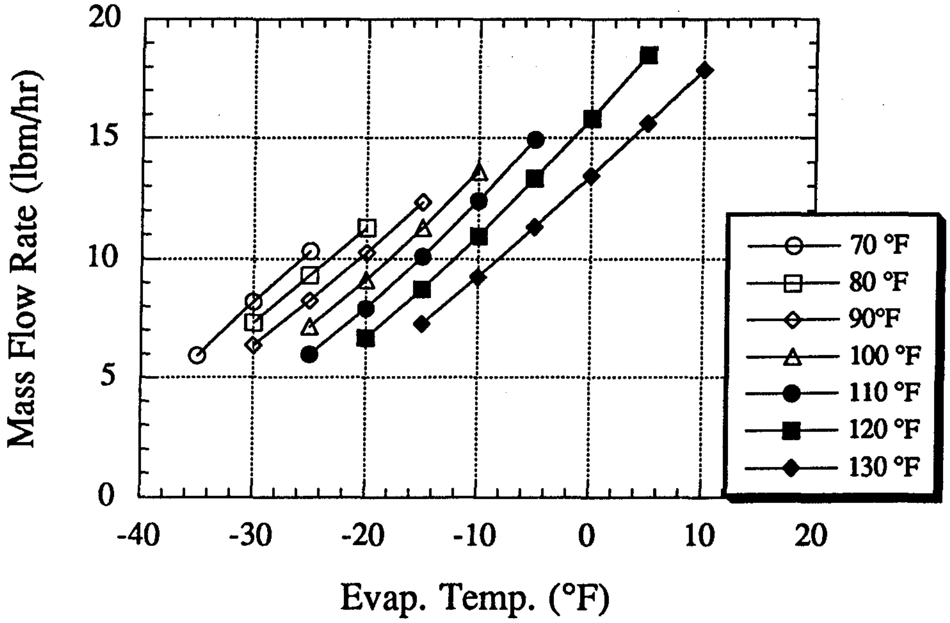

Figure I.3 3600 rpm mass flow map

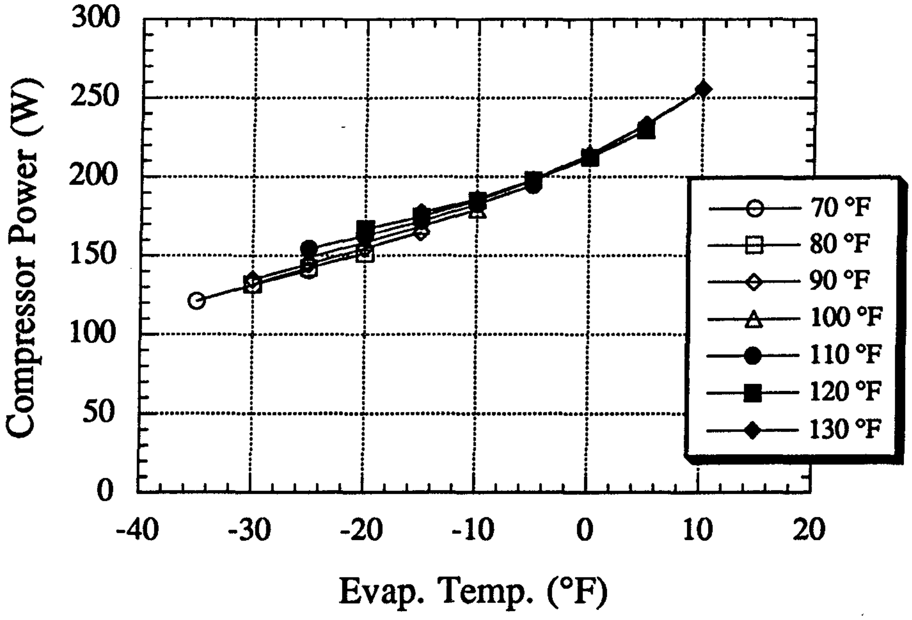

Figure I.4 3600 rpm power map

I.3 Compressor speed

The 2-speed Americold compressor model RV800 uses a 3-phase motor and a control box to change between two speeds (nominally 2400 and 3600 rpm). In order to validate the two speeds and to get a measure of the slip in the compressor motor, testing was performed with accelerometers mounted on the compressor shell to measure the compressor speed. Accelerometers measure the g forces exerted by the compressor motor. By analyzing the frequency of the piston cylinder moving back and forth, it is possible to get an ideal as to what the speed of the compressor is. In addition to mounting the accelerometers, an isolation amplifier was used on one data point to measure the exact frequency that was input to the compressor motor. Although the design details of the 3-phase motor is unknown, it is believed that the speed is changed by changing the incoming frequency to the motor. The use of the isolation amplifier enables the current and voltage signal from the control box to be isolated so that they can be analyzed on a signal analyzer. Steady state testing was performed at four ambient temperatures of 60 °F, 75 °F, 90 °F, and 100 °F. For each ambient temperature, the freezer and fresh food temperatures were varied from normal operating conditions of 0 °F and 40 °F respectively to extremely high cabinet temperatures that were close to the ambient temperature. This was believed to give a wide range of loading for which to test the compressor.

I.4 Compressor speed results

I.4.1 2400 rpm results

The first set of results are specific from a test in which the ambient temperature was at 90 °F and the freezer and fresh food temperatures were at 25 °F and 60 °F respectively. The isolation amplifier mentioned above was used on this data point. Figure I.5 shows the input frequency supplied to the motor from the control box at the low speed. For the frequency graphs, the data was sampled over 10 measurements and the resolution for the graphs is 0.0625 Hz. There is a very strong peak occurring at 41 Hz which represents the input frequency to the motor. There is also another peak occurring at 60 Hz which can be ignored because this is due to the power supply used for the isolation amplifier. Figure I.6 shows the resulting frequency of vibration as picked up by the accelerometer. Again we see another strong peak occurring at a frequency of 41 Hz. Already this tells us that the 3-phase motor must contain 2 poles since the compressor motor is spinning at the same frequency as the incoming signal. What this also tells us is that there is almost no slip occurring in the motor at 41*60 = 2460 rpm.

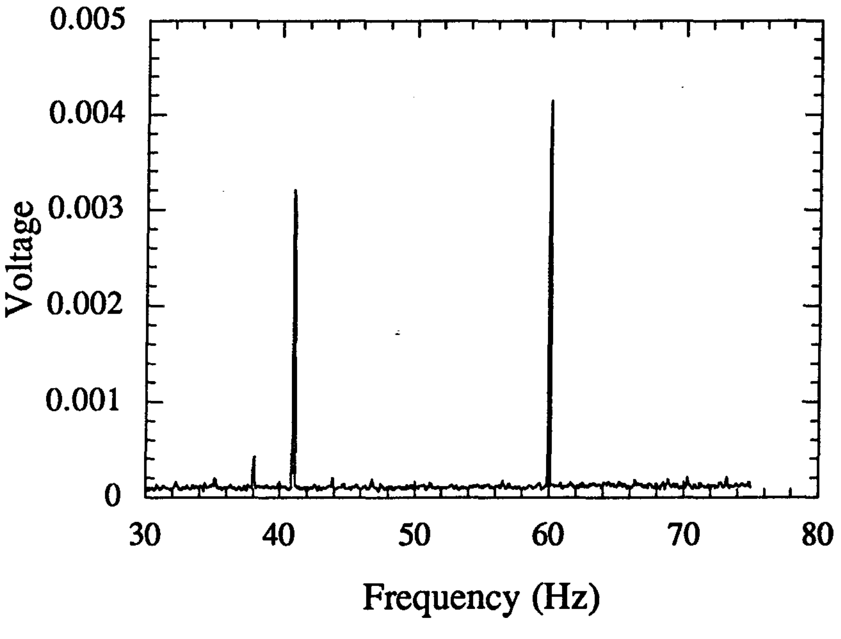

Figure I.5 Input frequency to compressor running at low speed

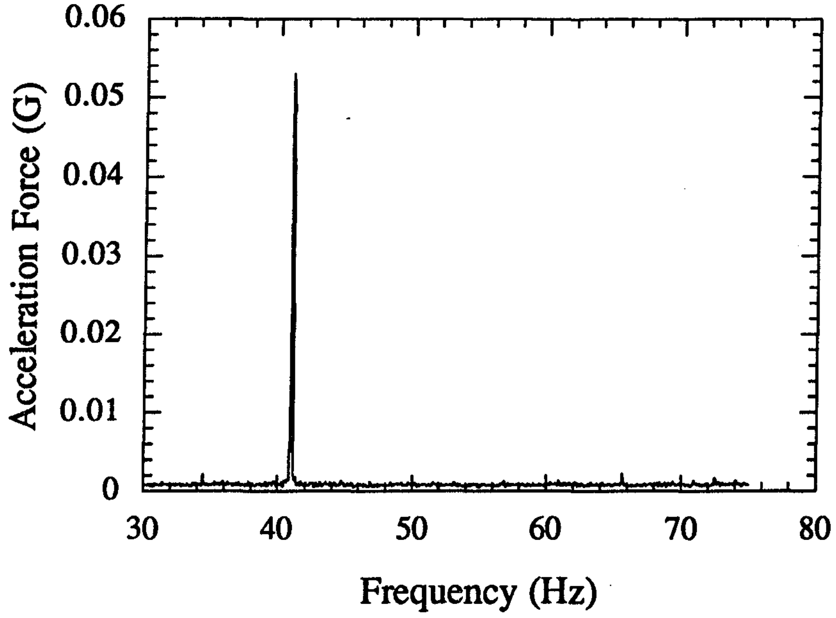

Figure I.6 Speed frequency as measured by the accelerometer at low speed

I.4.2 3600 rpm results

Now running the compressor at the high speed for the same ambient and compartment temperatures as above, we see a result that differs slightly from what we saw at the low speed. For the high speed (nominally 3600 rpm), Figure I.7 below shows the input frequency to the compressor as measured by the isolation amplifier. What Figure I.7 shows is that there is not simply one strong peak occurring, but actually a frequency span of 3 Hz from which the input frequency is being supplied around 69 Hz. This shows that the input frequency is not constant but is moving around this 3 Hz span. Our tentative conclusion is that the control box is taking 60 Hz Single Phase voltage and converting it to DC and then back to 3-Phase AC at a frequency around 69 Hz. Since, capacitors, resistors, and integrated circuits are being used, it is possible that one of these components is causing the signal to be unsteady at the high speed but not at the low speed. The compressor speed measured by the accelerometer is shown in Figure I.8 which shows that the compressor is running at a speed of 63 Hz or 3780 rpm. Even though the input frequency spans around a 3 Hz signal, the resulting compressor speed is not significantly affected by it due to the fact that there is slip occurring in the motor. The slip in the motor appears to cause the compressor motor to spin around 6 Hz slower than the input frequency.

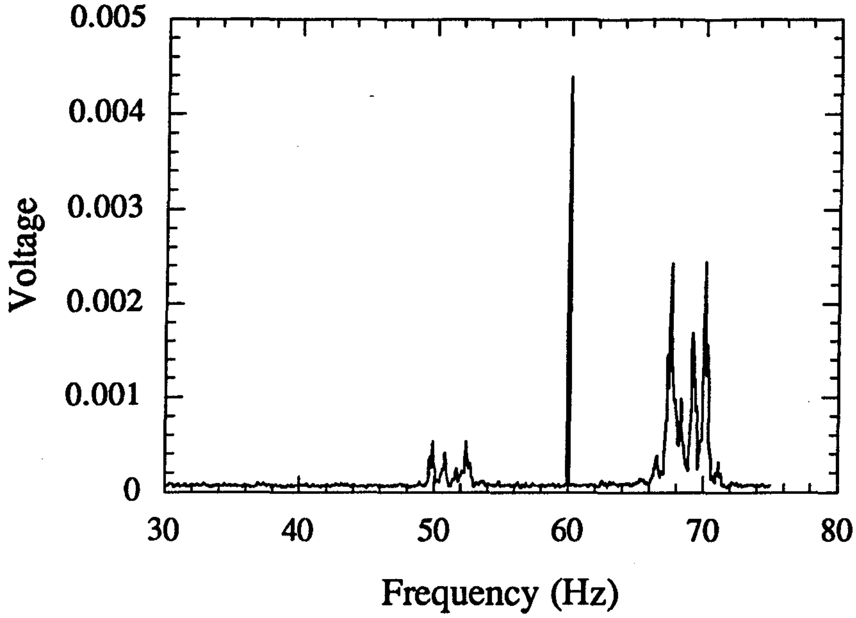

Figure I.7 Input frequency to compressor running at high speed

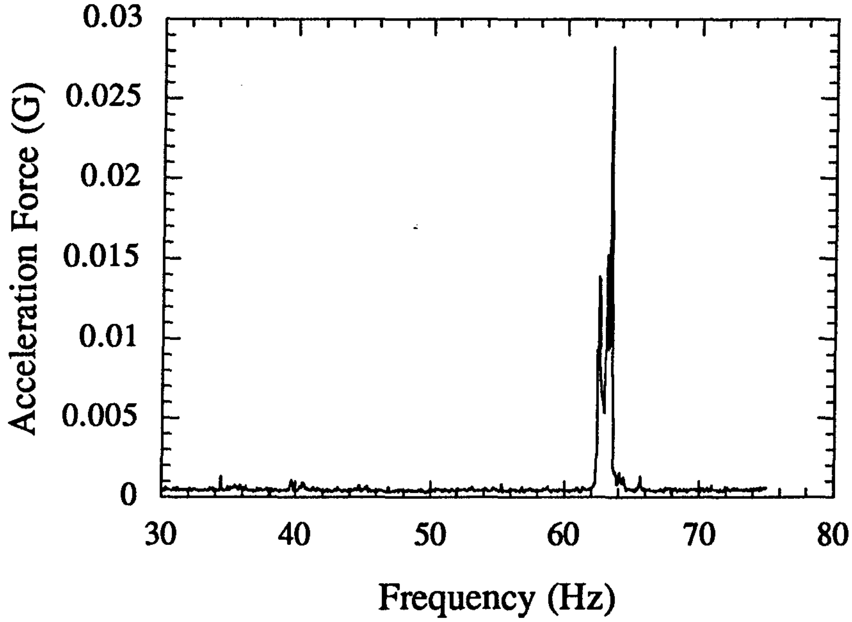

Figure I.8 Speed frequency as measured by the accelerometer at high speed

I.4.3 Compressor speed versus torque

With testing complete, the changes in compressor speed verses torque loading was examined for the entire data set which includes data points at the two speeds. For the high speed, the compressor speed was plotted versus the compressor torque, using equation I.2 to calculate the compressor torque T.

$$\text{Power}_{\text{comp}} = T \cdot \omega \qquad \text{(I.2)}$$

Figure I.9 and I.10 shows the results of the compressor speed versus compressor torque for the two speeds. From Figure I.9, it is seen that the scatter is random and the compressor speed does not fall as expected when the torque increases. Some explanation for this could be in the 3 Hz uncertainty in the input frequency at the high speed. This would translate to a 180 rpm uncertainty in the compressor speed which is about the range at which the compressor speed varies for the high speed. Also, it appears that the compressor torque does not change significantly when the refrigerator loading is increased. Possibly, the refrigerator for all of our loading conditions is operating in a range for which the slip is about the same and therefore the compressor speed should remain almost constant.

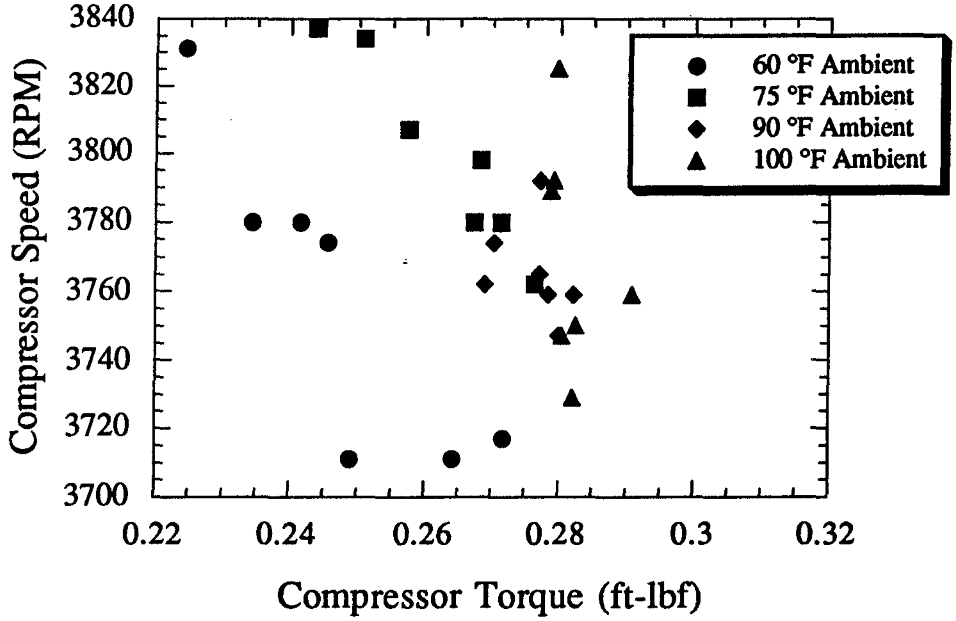

Figure I.9 High speed versus compressor torque

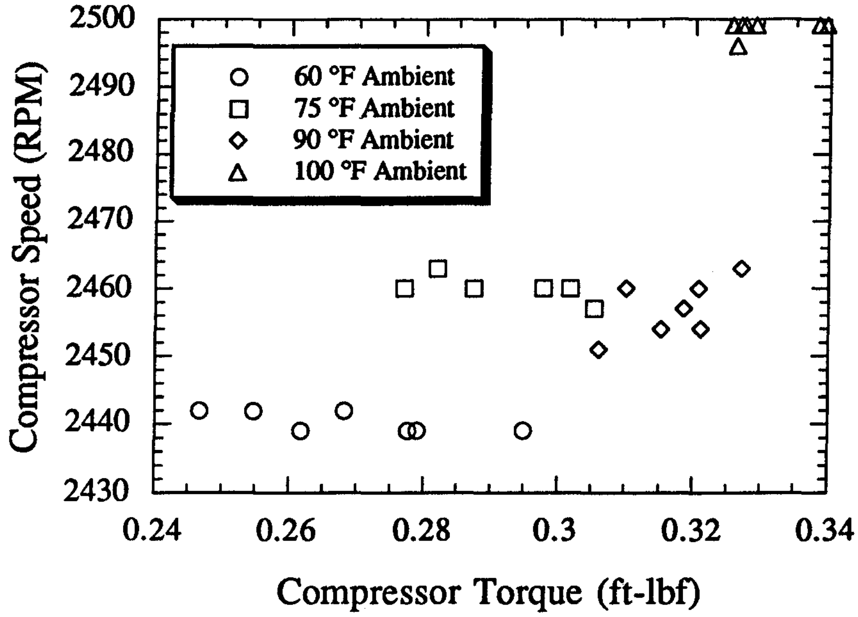

Figure I.10 Low speed versus compressor torque

For the low speed, instead of the compressor speed falling with an increase in torque, the compressor actually increases in speed with increasing torque. The data is plotted showing the four ambient temperatures taken. As shown earlier in Figure I.5 and I.6, there is almost no slip occurring at the low speed for the data point tested. Possibly there is no slip at all occurring in the compressor motor for all the loading conditions performed, in which case we would mean that we would expect Figure I.10 to show us a straight horizontal line with respect to torque. We see this occurring but not on one straight line. The 60 °F ambient temperature falls on one line close to a speed of 2440 rpm, the 75 °F and 90 °F falls on another line close to 2460 rpm, and finally the 100 °F data falls on another line close to 2500 rpm. Since there is almost no slip occurring at the low speed setting, these results suggest that the input frequency given to the motor is changing as the ambient temperature is changing. Some of the reasons why this is occurring might have to do with the capacitors and resistors located in the control box. During testing of the refrigerator at the 4 ambient temperatures, the control box was placed in the isothermal chamber along with the refrigerator. It is possible that the properties of the resistors and capacitors changed with the swing in ambient temperature. If the resistors and capacitors are designed to hold their properties at around room temperature of 77 °F, it could explain why the 75 °F and 90 °F data fall on the same line. As the temperature is decreased to 60 °F or increased to 100 °F, it is possible that the resistance of the resistors is changing along with the capacitance of the capacitors. This result might also be occurring at the high speed but is not discernible in the data because of the 3 Hz uncertainty swing in the incoming frequency. One way to check to see if this is the cause of error would be to increase the wire length and have the box sit outside of the chamber in nearly constant room temperature. Such future experiments could determine whether our resistors and capacitors are changing from their specifications or not. For purposes of our experiments, however, it is not critical that the compressor speed be known with greater accuracy.

I.5 Compressor heat transfer coefficient

With a new compressor installed in the system, it was necessary to re-estimate a compressor heat transfer coefficient. The procedure is exactly the same as outlined in Appendix E. A curve-fit for the compressor shell temperature based on the exit refrigerant temperature was performed and shown below in Equation I.3.

$$T_{shell} = 0.91117 \cdot T_{compout} - 10.2 \qquad (I.3)$$

Data obtained at both the low and high compressor speed was used in the estimation. The resulting optimization showed that the compressor heat transfer coefficient is 6.586 Btu/hr-°F with a 95% confidence interval of 35.68 Btu/hr or 10% of the compressor heat transfer. Figure I.11 shows the comparison of the predicted compressor heat transfer with the experimentally measured.

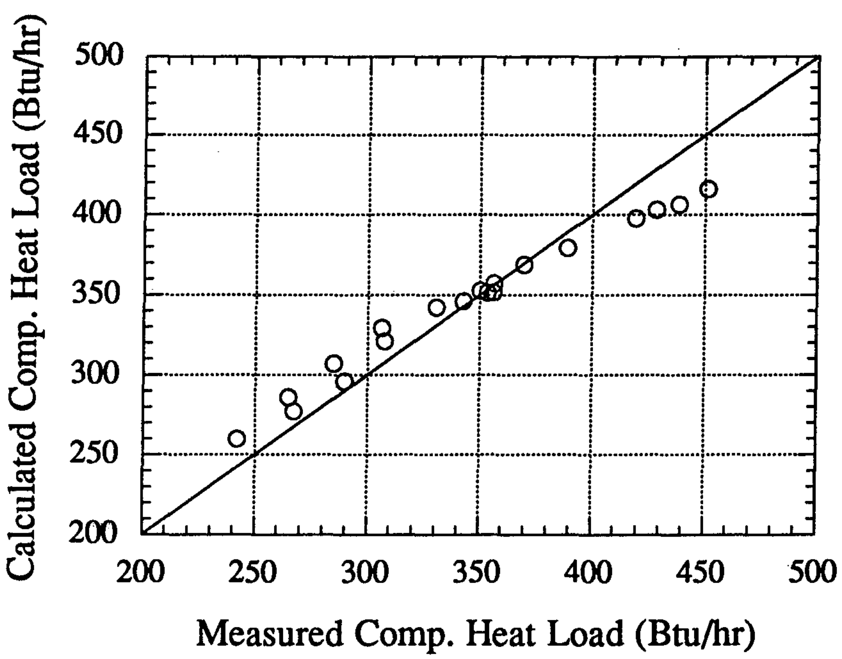

Figure I.11 Calculated and measured compressor heat rejection (Americold)

I.6 Evaporator volumetric flow rate and split-air fraction

When the two-speed compressor was installed into the refrigerator system, a new capillary tube-suction line heat exchanger was also installed. Since this required removing the evaporator fan, another estimation of the split-air fraction and volumetric flow rate was needed when the system was put back together. Altogether, 24 steady state data points were taken at ambient temperatures of 60 °F, 75 °F, 90 °F, and 100 °F. In order to get a good estimate of the volumetric flow rate, only 20 data points were used out of the 24. Currently, 4 thermocouples measure the outlet evaporator air temperature (see Appendix A). The maximum temperature difference of the 4 thermocouples were examined in respect to the temperature difference seen across the evaporator. Of the 24 data points used, 4 had a greater than 5 % error so they were eliminated in the parameter estimation of volumetric flow rate. For the split-air fraction estimation, all 24 data points were used. The same equations are used as described in Appendix B for estimating the two parameters. Since the two parameters were being estimated from two different data sets, it was necessary to perform an iterative process to arrive at a split-air and volumetric flow rate that minimized the error in the measured and calculated exit evaporator air temperature. The split-air fraction was estimated at 0.909 and the volumetric flow rate at 48.3 cfm. These values produced a 95% confidence interval of 1.4 °F on the exit evaporator air temperature.

Appendix J

Effects of Varying Condenser Fan Speed

J.1 Introduction

Previous results by Woodall and Bullard (1997) have looked at the effects of varying the heat exchanger fan speeds in a refrigerator/freezer system. Results were obtained by running simulations with a validated RFSIM model. Woodall found that no benefit could be achieved by reducing the evaporator fan speed. Increasing the evaporator fan speed produced an increase in evaporator capacity due to a higher air-side heat transfer coefficient, but the fan power plus the compressor power required to remove the fan-generated heat will ultimately increase at a faster rate. In the case of reducing the evaporator fan speed, the reduction in the evaporator capacity due to a lower air-side heat transfer coefficient was greater than the savings obtained by reducing the evaporator fan power.

The model showed that energy savings could be achieved under some conditions when the condenser fan is decreased. When the condenser is decreased in speed, the air-side heat transfer of the condenser will decrease, raising the condensing temperature, and reducing the amount of subcooling in the condenser. The extra charge then migrates to the evaporator where it reduces the amount of superheat causing more of the evaporator area to have a higher UA. Therefore, the evaporator capacity will increase. The opposite effect was observed when the condenser fan speed and power were increased.

J.2 Testing results

Since modeling efforts have shown that energy benefits could be achieved by reducing the condenser fan speed, the condenser fan in the side-by-side Amana test unit was tested by reducing its speed. The condenser fan located is an AC permanent split capacitor (PSC) Morrill motor having a rated efficiency of 40%. Specifications for the condenser fan show are shown in Table J.1 below:

Table J.1 Morrill PSC motor specification

Rated Output [W]	Nominal Speed [RPM]	Voltage [AC]	Current [A]	Class
2.3	1300 CW (facing lead end)	115	0.05	B

Although the fan speed is rated at 1300 rpm, measurements with a strobe light indicate that the actual speed in the refrigerator is around 1640 rpm. The higher speed could indicate that the motor is operating with less pressure drop than it was designed for. For reducing the speed of the condenser, a frequency controller was used. The frequency controller uses a function generator to generate the AC sine wave along with an amplifier to bring the amplitude up to 120 V. A more detailed description of the actual circuit is described by Cavallaro and Bullard (1995). Using the frequency controller, the condenser fan speed was reduced to about 50% of its nominal speed in a 90 °F and 60 °F ambient environment where the cabinet temperatures were set to 5 °F and 45 °F in the freezer and fresh food compartments. All testing was done at the low 2400 RPM compressor speed since this is the speed at which the refrigerator will run for the majority of the time. Results of changing the condenser fan speed are shown below in Figure J.1:

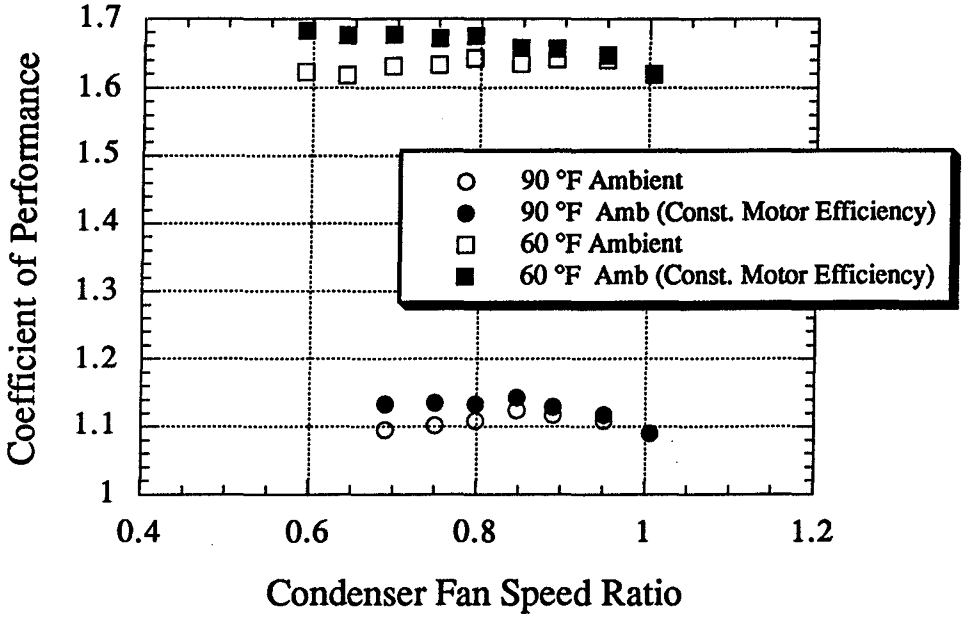

Figure J.1 Condenser fan speed ratio vs. ambient temperature

The ratio of the condenser fan speed represents the amount of reduction from the original fan speed of 1640 RPM. The open symbol shows the results of calculating the system COP using the condenser fan power as measured by the watt transducer. It is already known that as the condenser motor is reduced, its efficiency drops. To show the true energy savings possible, the closed symbols are plotted which represents the maximum increase in COP achievable by having a constant efficiency condenser fan. An explanation on the motor efficiency is discussed in a later section. The open symbols show that the measured COP increase is only 1.4% at 60 °F ambient and 3.1% at 90 °F ambient. For the 60 °F ambient case, the maximum COP occurs when the speed is reduced to 80% of its original speed. For the 90 °F ambient case, the maximum COP occurs when the speed is reduced to 85% of its original speed.

There are two possible effects on the refrigerator system if the condenser fan speed is reduced. First, reducing the condenser fan speed means a reduction in its power and therefore an overall reduction in the total system power. Second, reducing the condenser fan speed will increase condensing temperature as condenser UA declines. It is not clear whether evaporating temperature will increase enough to produce a net increase in compressor EER as predicted in a compressor simulation by Woodall and Bullard (1997) for a 20 cu. ft. top mount refrigerator. To see what effects reducing the condenser fan speed has on compressor EER, the compressor EER map was plotted for the 90 °F ambient data as shown below in Figure J.2. The solid circles show how the compressor EER changes when the condenser fan speed is reduced by increments of 5%. The graph shows that the compressor EER does not increase, but remains constant and then starts to fall. This indicates that the initial increase in the system COP when the condenser fan speed is reduced is a direct result of the reduction in the condenser fan power. As the condenser speed is reduced further, the system COP starts to drop due to operating at a lower compressor COP.

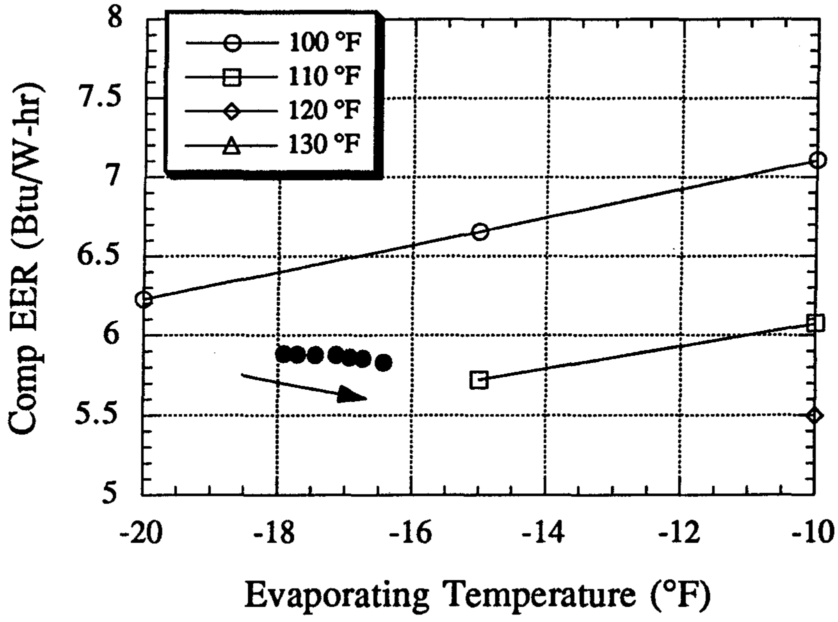

Figure J.2 Compressor EER map

J.3 Charge migration

The increase in system COP may be small due to an inexistence of subcooling at the capillary tube inlet. For both ambient temperatures tested, the capillary tube inlet existed as 2-phase. Reducing the condenser fan speed did show an increase in both the condensing and evaporating temperatures, but the amount of reduction in superheat was not large. This is due to having little charge migrate to the evaporator from the condenser. A check on the density of R-

134a shows that 2-phase refrigerant at a quality of 5% is 50% less dense than liquid refrigerant. Had the capillary tube inlet been subcooled, twice as much refrigerant would have migrated to the evaporator increasing the size of the 2-phase zone enough to raise the evaporating temperature to produce a net increase in compressor EER. Figure J.3 shows how the superheat level in the evaporator changed as the condenser fan was reduced.

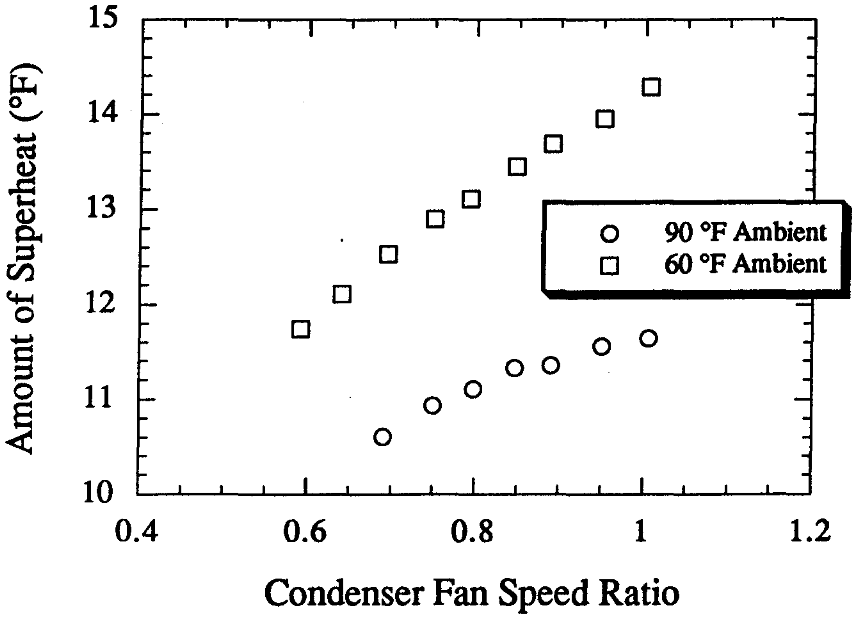

Figure J.3 Amount of superheat vs. condenser fan speed ratio

J.4 Motor efficiency

Reducing the condenser fan speed significantly reduced the efficiency of our PSC condenser motor due to the fact that the AC motor was not designed for variable speed operation. If the motor efficiency had remained constant as in the case of many motors specifically designed for variable speed operation, then the power reduction would have dropped as the cube of the speed reduction as shown in Equation J.1:

$$\frac{\text{Power}_{\text{new}}}{\text{Power}_{\text{nominal}}} = \left(\frac{N_{\text{new}}}{N_{\text{nominal}}}\right)^3 \qquad \text{(J.1)}$$

Data taken on the condenser fan was analyzed to calculate its efficiency at the different speed ratio. The efficiency for the motor drops off gradually as the condenser speed is reduced. As stated earlier, the condenser fan is rated at an efficiency of 40%. With the current setup of the refrigerator, the condenser fan appears to run at a speed greater than the nominal with a higher efficiency of around 55%. Figure J.4 shows the efficiency for the different speed ratio.

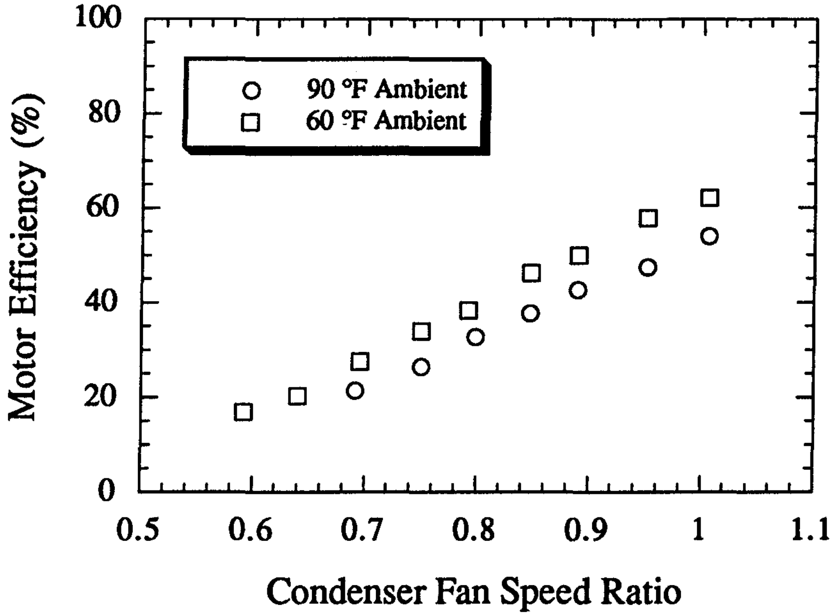

Figure J.4 Motor efficiency vs. condenser fan speed ratio

J.5 Conclusion

Small energy savings could be achieved by slowing down the condenser fan speed. Two causes for the small increase have been identified and examined. First, the non-existence of subcooling existing at the capillary tube inlet can cause about 50% less charge to migrate to the evaporator. Had more charge been able to migrate, it is possible that an increase in the compressor EER could be achieved which would result in higher system COP. Another factor contributing to a small increase in the system COP is due to the condenser motor efficiency. Had a constant efficiency motor been used, about a 5% increase in system COP could be achieved.

Appendix K

Two-Speed Compressor Operation

K.1 Introduction

While manufacturers strive to design a system that is both energy efficient with a fast pull-down capacity, multi-speed compressors are one option that is under consideration. Multi-speed compressors have a huge benefit in allowing the loading conditions on a refrigerator to be better matched. Typical refrigerators with a single speed compressor have to compromise between pull-down capacity and energy efficiency in their design. Refrigerators designed for energy efficiency will have a very poor pull-down performance and therefore cannot handle a large load. Refrigerators designed for a fast pull-down capacity, however, will tend to cycle more frequently which results in high cycling losses (Krause and Bullard, 1996 and Coulter and Bullard, 1995). A two-speed compressor is currently being analyzed which will allow manufacturers to design refrigerator systems that are energy efficient with a fast pull-down capability.

Operation of a two-speed compressor will allow refrigerators to operate at a low speed for the majority of the time. The low speed will allow the refrigerator to operate more efficiently while still having the ability to switch to a high speed whenever a fast pull-down is needed. A fast pull-down would be needed if ever there are frequent door openings, warm foods added to the compartments, or defective door gaskets or door seals. There are distinctly two advantages to running a compressor at a low speed. First, the compressor will run more efficiently since there is less of a pressure difference that the compressor must overcome. Secondly, the reduced evaporator capacity will force the refrigerator compressor to run longer, meaning a reduction in the cycling losses.

Modeling of a two speed compressor has already been performed by Woodall and Bullard (1997). Those results showed that at least a 5% savings in the yearly steady-state energy use could be achieved with a compressor that is only 1.5% more efficient at the low speed. Woodall's results were dependent on scaling factors used on an existing high speed compressor map to simulate how the low speed compressor map would operate. These experiments were undertaken because no compressor maps existed for a compressor operating at 2400 RPM. Analysis of the measured performance of the Americold 2-speed compressor (Appendix I) shows that the compressor is approximately 15% more efficient at the low speed. Since the 2-speed compressor is more efficient than Woodall's modeling had initially assumed, the experimental results should show a greater than 5% savings in energy.

The two speed Americold compressor analyzed has a three phase motor. Essentially, the compressor operated at two different frequencies which produced speeds of 2400 RPM and 3600

RPM. Compressor maps for the two different speeds were generated in-house as described in Appendix I.

K.2 Steady-state energy savings

Data was taken at four ambient temperatures of 60 °F, 75 °F, 90 °F, and 100 °F. The lowest ambient temperature was first started at the lowest compartment temperatures. Once steady state was reached, data was logged first at the low compressor speed of 2400 RPM and then at the high compressor speed of 3600 RPM before the next higher ambient temperature was set. The average time between logging data points at both speeds of 2400 and 3600 RPM was 3 hours. By logging data in this manner, comparisons between the low and high speed for a given temperature (ambient, freezer, and fresh food) can be made without fear of distortion due to frosting of the evaporator or refrigerant leaking from the refrigerator. To further help eliminate uncertainty due to evaporator frosting, the evaporator was defrosted after approximately 24 hours of compressor operation. Typically, only 4 to 9 oz of frost had formed. Figure K.1 through K.4 show the graphs of the evaporator capacity and system power for the four ambient temperatures tested.

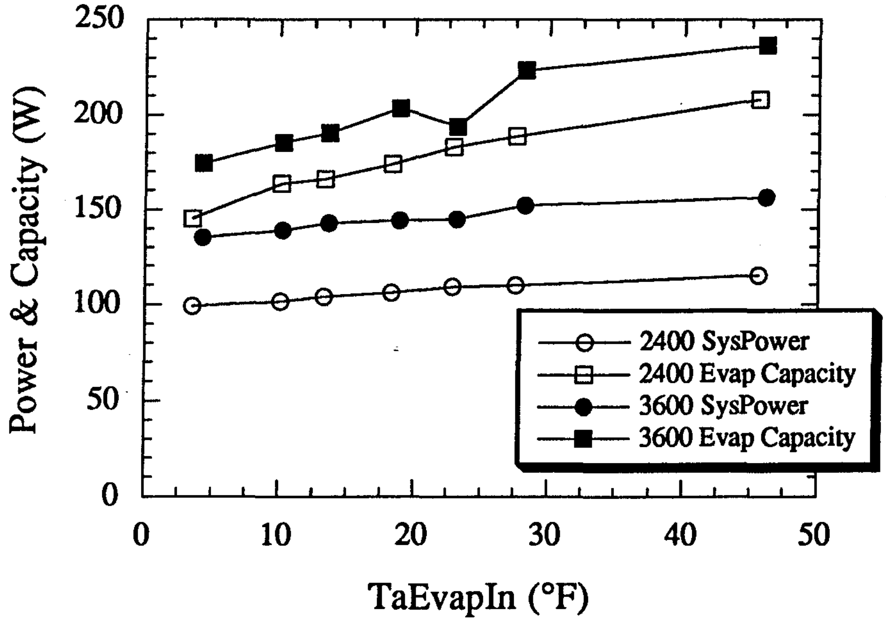

Figure K.1 60 °F ambient temperature

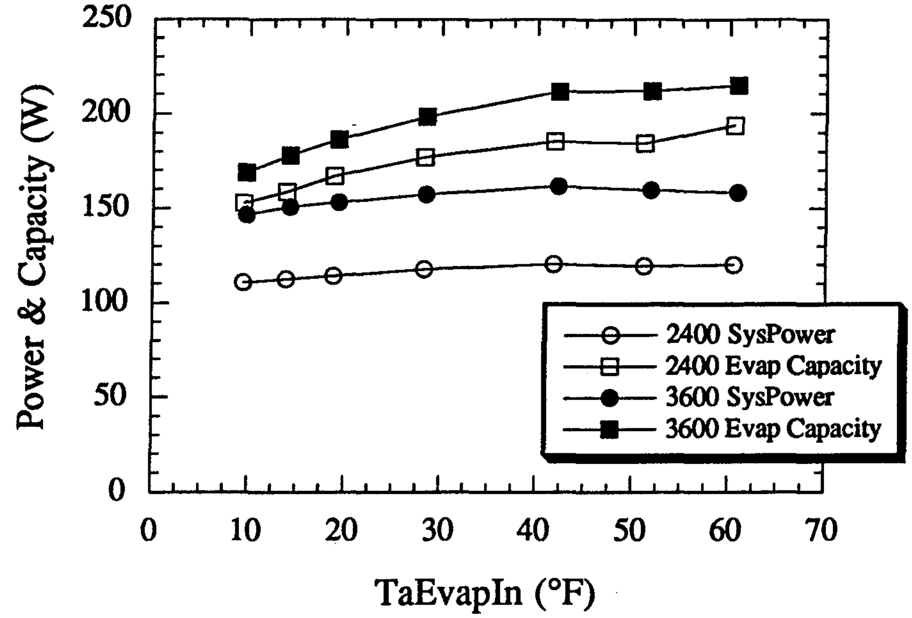

Figure K.2 75 °F ambient temperature

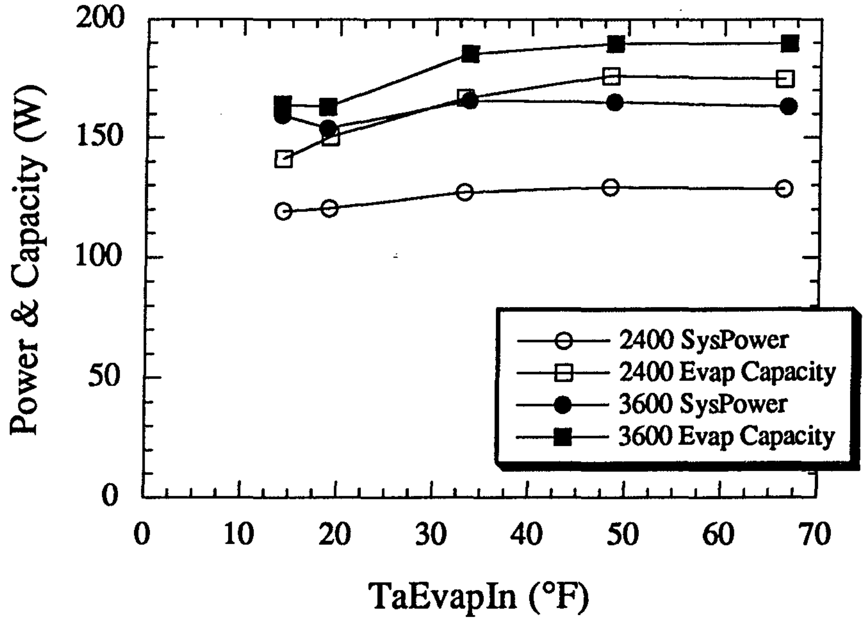

Figure K.3 90 °F ambient temperature

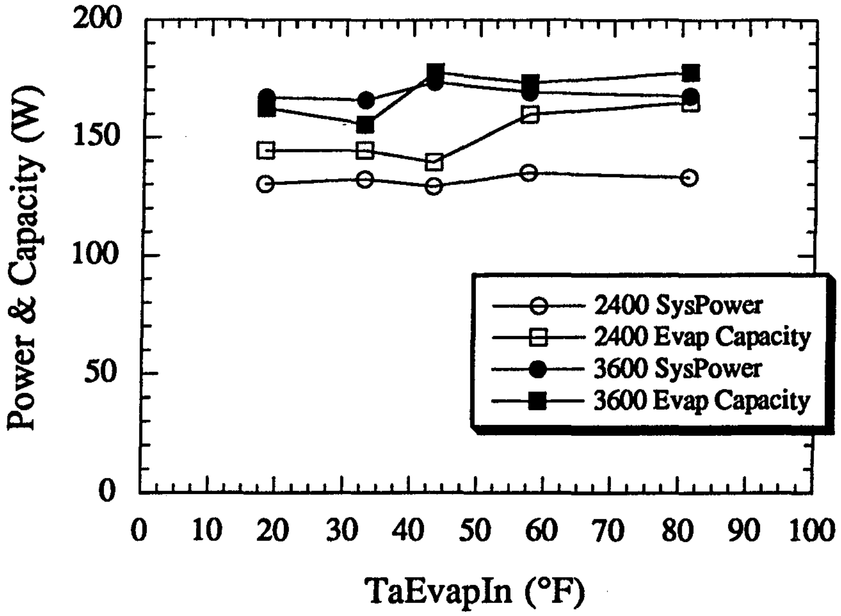

Figure K.4 100 °F ambient temperature

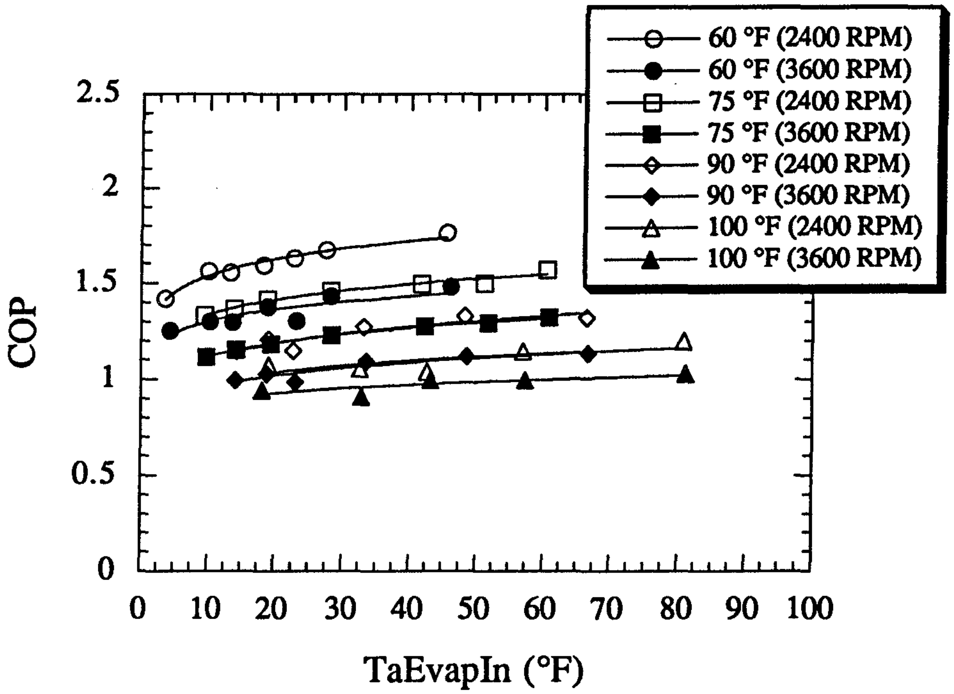

Figure K.5 COP comparison

Experiments at high compartment temperatures were conducted to provide the basis for analyses of the evaporator performance (Appendix G). There is a noticeable trend in the data for evaporating capacity and power to increase as the compartment temperatures rise. This is due to having a larger temperature difference occurring across the evaporator. In some of the data, there is a noticeable dip in evaporator capacity and system power that remains unexplained. Most likely, experimental error may account for some of the problems experienced. However, the graphs still do show the trends of what is occurring in the data set.

The system COP for each data point is then the calculated as the ratio of the evaporator capacity minus the evaporator fan to the system power. Figure K.5 shows the calculated steady-state COP for the data taken. Again there is a tendency for the COP to rise as the evaporator inlet air temperature is increased. For a baseline case in which the inlet mixed air to the evaporator is 12 °F, the COP is analyzed more completely as shown in Table K.1 and K.2.

Table K.1 Net efficiency gain

Ambient Temp (°F)	COP		COP gain (%)
	2400 RPM	3600 RPM	
60	1.55	1.30	19.2
75	1.37	1.15	19.1
90	1.14	1.00	14.0
100	1.03	0.92	12.0

Table K.2 Net power and capacity difference

Tamb (°F)	System Power (W)		Power Difference	Evap. Capacity (Btu/hr)		Capacity Difference
	2400 RPM	3600 RPM		2400 RPM	3600 RPM	
60	103.7	142.8	27.4%	566.7	649.5	12.7%
75	112.6	150.6	25.2%	542.1	608.2	10.9%
90	119.7	159.5	25.0%	481.7	559.6	13.9%
100	130.0	165.1	21.3%	476.0	535.6	11.1%

K.3 Conclusions

The system COP was observed to increase as much as 19% in a 60 °F ambient room and 12% in a 100 °F ambient room. These COP measurements show that a tremendous advantage can be achieved in running the compressor at a low speed. A breakdown of the evaporator capacity and power show that the 12 percent reduction in evaporator capacity is nearly independent of ambient temperature. A greater reduction in system power is achieved at the lower ambients, hence the higher COP gain. Previous simulation results by Woodall had identified a potential 9% energy savings due to the reduced temperature lift in a top-mount refrigerator. Woodall also found that if the compressor ran more efficiently at the low speed, then a higher increase could be achieved. In our experiments at 90 °F ambient, the COP increased about 14%. A combination of three factors arrive at this overall 14% increase which is difficult to break down. Some of the energy savings is due to the reduced temperature lift that the compressor must overcome and some is due to the fact that the compressor is more efficient at the low speed. The third factor to consider is that the heat exchanger fans are going to reduce the energy savings due to the long on-cycle they experience.

Appendix L

Optimal Charging for Maximum COP

L.1 Introduction

With the installation of the new two-speed Americold compressor into the 25 cu. ft. side-by-side Amana refrigerator, it was first noticed that the previous Tecumseh compressor was rated at a higher capacity (900 Btu/hr) while the new Americold was rated at 800 Btu/hr. Initial experiments showed that the new Americold compressor required a longer pull-down period as expected, and that 100% runtime for the low compressor speed (2400 rpm) occurred at 90 °F ambient with 5 °F and 45 °F in the freezer and fresh food respectively. Ideally the entire refrigeration system should be redesigned for the new compressor, but another approach taken was to increase the charge in the system until a maximum in steady state COP is reached at 5 °F and 45 °F in a 90 °F chamber.

L.2 Finding optimal charge

The optimization procedure was performed at the low compressor speed (2400 rpm) since this is the speed that the compressor will operate for the majority of the time. The chamber was set at 90 °F ambient and the refrigerator was charged with the factory recommended 5.125 oz of R-134a. Once 5 °F and 45 °F was reached in the freezer and fresh food compartment, data was logged for 20 minutes. Increments of 5 grams of R-134a were added to the system and allowed to equilibrate at steady state. Figure L.1 shows how the resulting COP changes as refrigerant charge was added.

A maximum in COP was finally reached when the system had 6 oz of charge. At this charge level, the COP is 12% better than the original factory charged system. Figure L.2 shows how the resulting superheat in the system changed. It is worth noting that the maximum COP was obtained when the exit of the evaporator existed as a saturated vapor. This result is not surprising at all because with a 2-phase evaporator exit, the heat exchanger has entirely filled with 2-phase refrigerant which has a higher refrigerant-side heat transfer coefficient than superheated vapor. Therefore, the evaporator runs at a higher capacity. A look at the system with the original 3600 rpm Tecumseh compressor showed that the system operated with around 13 °F of superheat at the same test point.

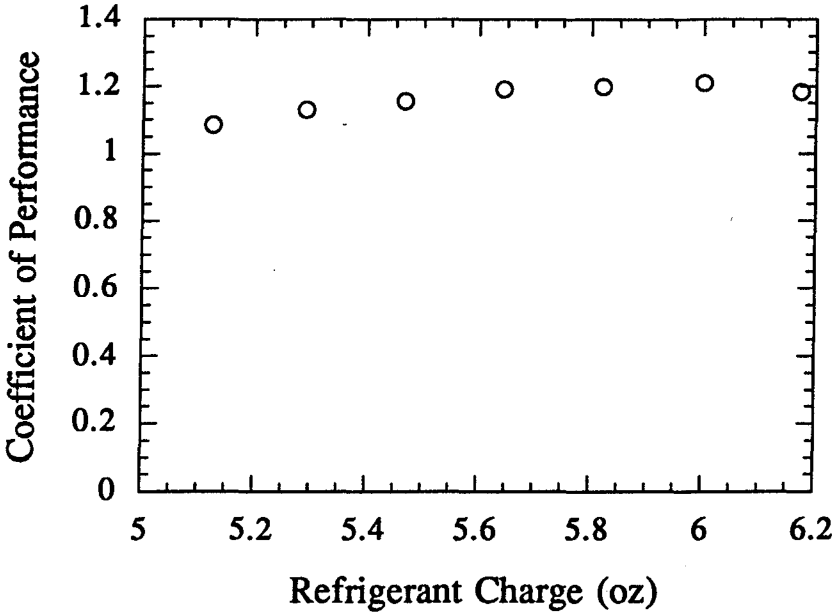

Figure L.1 Effect of charge on refrigerator performance

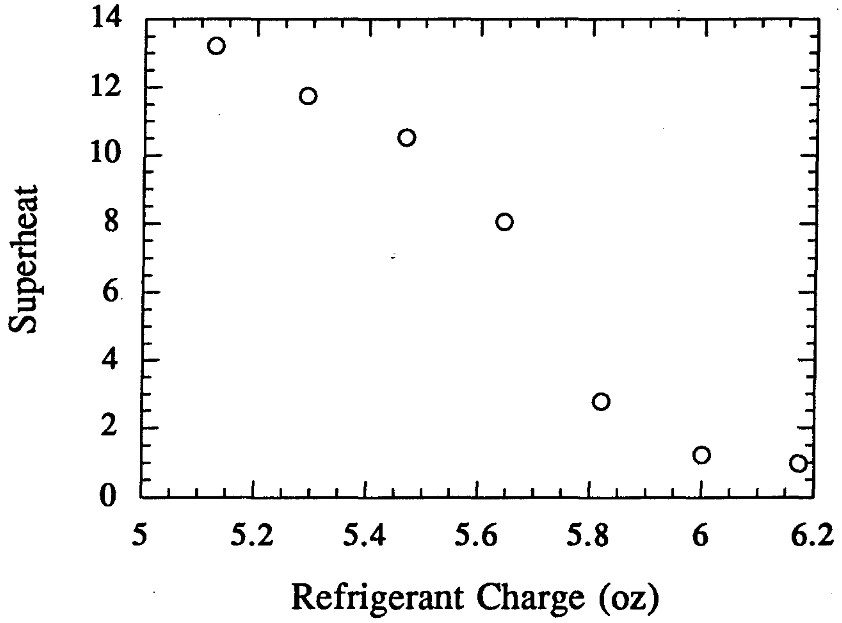

Figure L.2 Amount of evaporator superheat vs. charge level

L.3 Experiments conducted at optimal charge

The condenser fan speed was reduced, as described in Appendix J were conducted with the optimally-charged system. Since the new optimal system had no superheat at 5 °F and 45 °F in a 90 °F chamber, reducing the fan speed had no affect on the system COP because there was no superheated zone in the evaporator to eliminate. Figure L.3 shows how the system COP changes with a reduction in the condenser fan speed for a 60 °F and 90 °F ambient temperature. In this test data, the actual condenser fan power consumption was used in the COP calculation. Had a constant efficiency fan been assummed in the COP calculation, then a slight increase (about 2%) in COP would result from the decrease in fan speed and power. It is believed that the increase in system COP due to decreasing the condenser fan speed is a direct result of charge re-distribution. Charge from the condenser would migrate to the evaporator ultimately reducing the amount of superheat, meaning a greater 2-phase evaporator area. Since 2-phase refrigerant has a higher heat transfer coefficient than vapor, an increase in evaporator capacity would be seen.

In these experiments, there was no superheat even at the 60 °F ambient. Therefore the evaporating temperature did not change in response to the charge migration. On the other hand, the increase in condensing temperature due to the lower air-side heat transfer coefficient on the condenser offsetted the effect of the reduced condenser fan power to result in a constant COP.

To see what affects system COP has when the condenser fan speed is reduced, the refrigerator was recharged back to the factory recommended amount where 13 degrees of superheat existed.

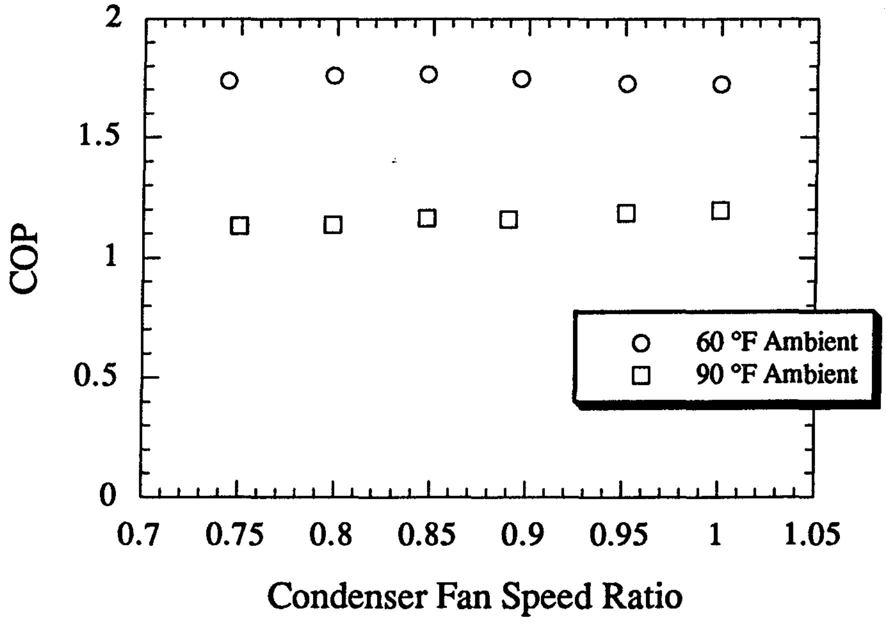

Figure L.3 Effects of reducing the condenser fan speed

L.4 Conclusion

Increasing the charge in the refrigerator by 20% has shown that the steady state COP can be increased by 12%. The drawback of keeping the system charged at 6 oz of R-134a is that no superheat exists in the system at these highly charged conditions. The refrigerator with the original single speed compressor had around 13 °F of superheat at the exact same point. Although the system was optimized for steady-state operation, actual refrigerators are optimized for cycling operation. As more refrigerant is added to the system, the actual runtime of the refrigerator will decrease causing the refrigerator to cycle more frequently. This will then cause more cycling losses to occur which is what manufacturers look at when optimizing their systems.

Appendix M

Refrigerant Dissolved in Oil

M.1 Introduction

During cycling and steady state operation of the refrigerator, knowing the amount of refrigerant dissolved in the oil is important in modeling the refrigerator since there is only a fixed amount of charge in the system. The amount of refrigerant dissolved in oil is mainly a function of temperature and pressure. Refrigerant/oil solubility equations relate pressure, temperature, and concentration at saturation conditions. Grebner and Crawford (1992) published a set of equations which are presently used in the RFSIM model. In this Appendix, those equations will be analyzed to see how accurate they are at predicting the amount of refrigerant dissolved in the oil for operating conditions. Finally, an analysis of the error associated with the Grebner-Crawford equations will be made to see if the equations can be used to detect a leak in the refrigerator test unit.

M.1 Steady state and cycling

The refrigerant that is dissolved in the oil exists in a liquid phase. The Grebner-Crawford equations shown in equation M.1-M.5 where x1 through x7 are experimentally determined constants can be used to calculate w which represents the liquid refrigerant fraction shown in equation M.5.

$$T^* = (1-w)(A+BP) \tag{M.1}$$

where:

$$T^* = \frac{T - T_{sat}(P)}{T_{sat}(P)} \tag{M.2}$$

$$A = x1 + \frac{x2}{w^{1/2}} \tag{M.3}$$

$$B = x3 + \frac{x4}{w^{1/2}} + \frac{x5}{w} + \frac{x6}{w^{3/2}} + \frac{x7}{w^2} \tag{M.4}$$

$$w = \frac{m_{liq\ ref}}{m_{oil} + m_{liq\ ref}} \tag{M.5}$$

Only T, the mixture temperature, and P, the vapor pressure of the mixture, need to be specified in order to calculate the liquid refrigerant fraction. For the refrigerant-oil mixture of R-12 with Naphthenic mineral oil, the pressure and temperature ranges for which these equations are valid is 0 - 600 psia and 400 - 750 R respectively. Steady-state and cycling data for the Whirlpool refrigerator model ET20PKXYW02 were obtained by Krause and Bullard (1994) and used with the Grebner-Crawford equations to calculate the liquid refrigerant fraction. Figure M.1 shows amount of refrigerant dissolved in the oil for the different steady state and cycling points, assuming that the amount of oil in the compressor is equal to the factory charge.

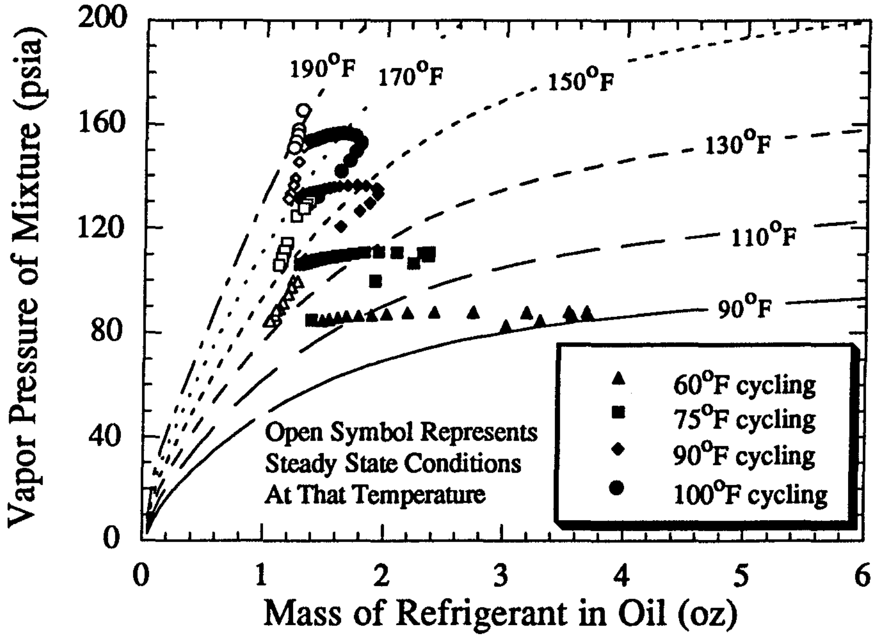

Figure M.1 Cycling and steady state data

The Whirlpool has a high side compressor so the compressor exit pressure was used as the vapor pressure of the mixture and the compressor shell temperature was used to represent the mixture temperature of the liquid refrigerant in oil. During the first minute of the on-cycle, the compressor exit pressure rises steadily at a constant shell temperature and the maximum amount of refrigerant now exists in the oil. With time, the shell temperature starts to increase and the amount of refrigerant in the oil decreases as the shell temperature rises at a constant compressor exit pressure. The above calculation assumes instantaneous adjustment to equilibrium states. It ignores time lags for a refrigerant-oil mixtures which under some conditions have been know to take more than 1 hr to reach equilibrium. Hyung Yoon reported that his R-134a/Napthanic oil mixture took over 1 hour to reach an equilibrium state when exposed to approximately the same temperature and pressure that our refrigerator compressor sees (1995).

At the start of the on-cycle when the pressure rises at a constant cold compressor shell, there is an initial driving force for the refrigerant to enter the oil. It is only after the compressor shell heats up does this driving force diminishes and there is actually a driving force pulling the refrigerant out of the oil. The open boxes represents the range of steady state (equilibrium) conditions observed at the different ambient temperatures. From viewing the graph, it appears that at the 90 and 100 degree ambient temperature, the refrigerator reaches steady state at the end of the on-cycle. For the 75 and 60 ambient temperatures, the refrigerator seems to just miss reaching steady state. The refrigerator can reach steady state operation during cycling for the 90 and 100 ambient temperature because the on-cycle time at these temperatures is much longer than the on-cycle time for the 60 and 75 ambient temperature.

M.2 Error for steady state and cycling data

Actual data from the Grebner-Crawford experiment were reviewed and analyzed to see how accurately their curve-fitted equations could predict liquid refrigerant given mixture temperature and vapor pressure near our operating data points. In addition, error associated with the calibration of the pressure (± 0.648 psia) and temperature(± 1.8 °F) instruments were also analyzed. For the cycling data, there was only one point in the Grebner-Crawford test matrix which was representative of all the cycling data points. This point was used and compared with the pressure and temperature measurement errors as shown in Table M.1.

Table M.1 Uncertainty in the mass of liquid refrigerant

Ambient Temperature (°F)	Grebner-Crawford Curve Fit	Pressure and Temperature Measurement
60	± 13%	- 7%, + 8%
75	± 13%	- 5%, + 5%
90	± 13%	- 3%, + 4%
100	± 13%	- 3%, + 3%

Table M.1 clearly shows that our accuracy in predicting the amount of refrigerant dissolved in the oil is limited by the Grebner-Crawford curve fit. While the Grebner-Crawford equations account for most of the error in predicting refrigerant dissolved in oil, additional errors occur due to the random error (uncertainty) associated with our pressure and temperature measurements.

M.3 Leak detection

To determine whether our refrigerator setup leaks its charge, isothermal "soak" data points are obtained in order to see if the total mass of refrigerant in our system remains constant. When the refrigerator is off and the allowed to equilibrate with the ambient temperature, the total refrigerant charge exists as superheated vapor in the tubing and as liquid dissolved in a refrigerant-oil mixture as shown in equation M.6.

$$m_{\text{vap ref}} + m_{\text{liq ref}} = m_{\text{tot}} \qquad \text{(M.6)}$$

where:

$$m_{vap\ ref} = \rho \cdot V_{tubing} \tag{M.7}$$

$$m_{liq\ ref} = f(P, T, m_{oil}) \tag{M.8}$$

With a known equilibrium pressure and temperature measurement of the refrigerant, the specific volume of the R-12 refrigerant can be determined and the mass of vapor refrigerant can be calculated once the total air volume of the refrigerator tubing is known. Table M.2 shows the volume calculations made for the Whirlpool refrigerator model ET20PKXYW02. The volume of the condenser, evaporator, interchanger, accumulator, and pressure taps are calculated by knowing their diameters and lengths. The filter dryer volume is also calculated by knowing the diameter and length, but the assumption is made that 1/3 of the volume of the filter dryer is desiccant so 2/3 of the volume is assumed to be occupied by the vapor refrigerant. (Krause and Bullard, 1994). Lastly, the compressor is modeled as a combination of a cylinder and a hemisphere. Once the compressor volume is calculated, the assumption that the free volume is only 1/2 the total volume is made based on discussions with the compressor manufacturer (Coriano, 1993). Therefore, only 1/2 the total volume of the compressor is assumed to be occupied by the refrigerant vapor.

Table M.2 Whirlpool volume estimations

Component	Volume (ft^3)
Evaporator	0.0230
Condenser	0.00768
Capillary Tube	0.000039
Suction Line	0.00292
Accumulator	0.00161
Pressure Taps	0.000593
Filter Dryer (2/3 Total)	0.000505
Compressor (1/2 Total)	0.0303
Total	0.0667

For calculations of the mass of liquid refrigerant existing as a refrigerant-oil mixture, the Grebner-Crawford equations are used again. Since the entire refrigeration loop is in equilibrium during an isothermal "soak" condition, the measured compressor temperature and pressure is used in the Grebner-Crawford equations for the mixture temperature and vapor pressure.

Data from a soak at 75 degree ambient was performed and Figure M.2 shows the steady state temperature and pressure obtained. For the soak data point, the refrigerator was charged with the factory recommended amount of 8.25 oz of R-12 and the refrigerator doors were remained opened during the test.

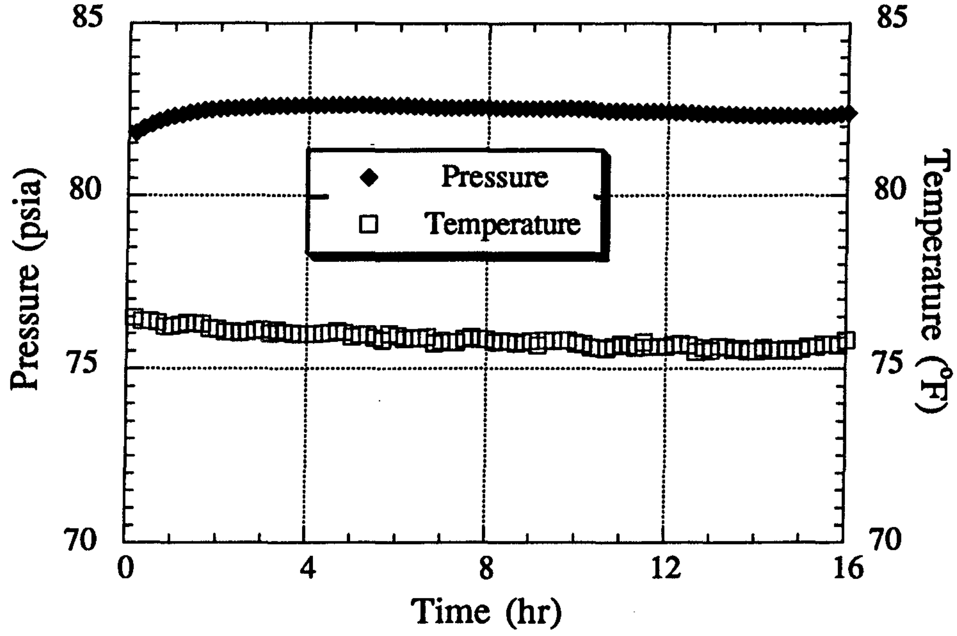

Figure M.2 Steady state temperature and pressure

Data points in the soak were recorded at 10 min intervals for 16 hours. Solving each of these values assuming that the amount of oil in the refrigerator is equal to the factory charge overpredicts of the total refrigerant mass as shown in Figure M.3.

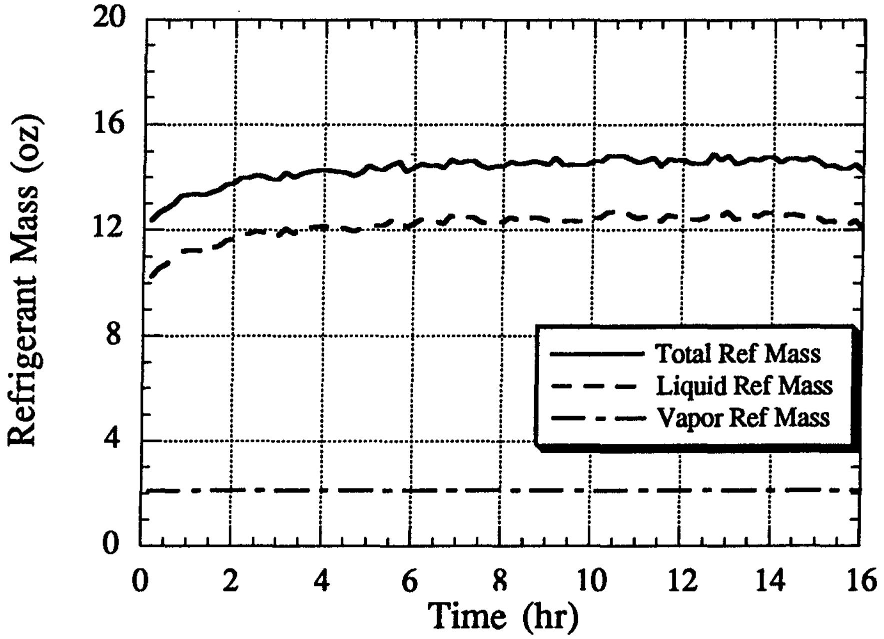

Figure M.3 Total mass of refrigerant in system

The total mass of refrigerant appears to have remained constant at 14 oz for the entire 16 hours that testing was performed. The initial rise in mass at the beginning of testing occurred because steady state conditions had not been reached when testing began. This can be seen in Figure M.3.1 because there is an initial rise in pressure and an initial fall in temperature at the beginning. Since the refrigerator was charged with only 8.25 oz of refrigerant, it is clear that the model overpredicts the amount of refrigerant present in the system. From viewing Figure M.3, it is seen that the Grebner-Crawford equations are the source of error since they predict the amount of liquid refrigerant to be around 12.5 oz.

M.4 Error for soak data test

Actual data from the Grebner-Crawford curve fit were found near the temperature and pressure of our soak point. Error calculations for the data were performed along with error calculations associated with the accuracy of our temperature and pressure measurements. Table M.3 summarizes the error found for each case.

Table M.3 Percentage error for soak data

Ambient Temperature (°F)	Grebner-Crawford Curve Fit	Pressure and Temperature Measurement
75	± 23%	- 28%, + 54%

Table M.3 shows that our model for predicting the amount of refrigerant dissolved in the oil has huge uncertainties. The amount of refrigerant dissolved in oil in the soak data range is much more sensitive to pressure and temperature than at cycling and steady state operating conditions. The accuracy of our instruments was the same for the two cases (± 0.648 psia, ± 1.8 °F), but their effects are greater. Also, our review of Grebner and Crawford's original data shows that their curve fit is also much poorer at those conditions, probably for the same reason: their pressure and temperature instruments were no more accurate than ours. Figure M.4 illustrates the fact that the refrigerant and oil mixture is very sensitive to pressure and temperature in the soak data range and this concludes why the amount of refrigerant in the oil is predicted to be around 12.5 oz when the refrigerator was only charged with a total of 8.25 oz.

Figure M.4 shows how the prediction of the liquid refrigerant can vary from approximately 8 oz to 19 oz due to temperature and pressure uncertainty alone, assuming the Grebner-Crawford equuations to be 100% accurate. With the addition of the error associated with the Grebner-Crawford equations, it can be seen that the total amount of liquid refrigerant in the oil can be as low as 6 oz which is where it should be in order for the total charge to equal 8.25 oz. The open circles in the figure above represents the "soak" data points taken for the test.

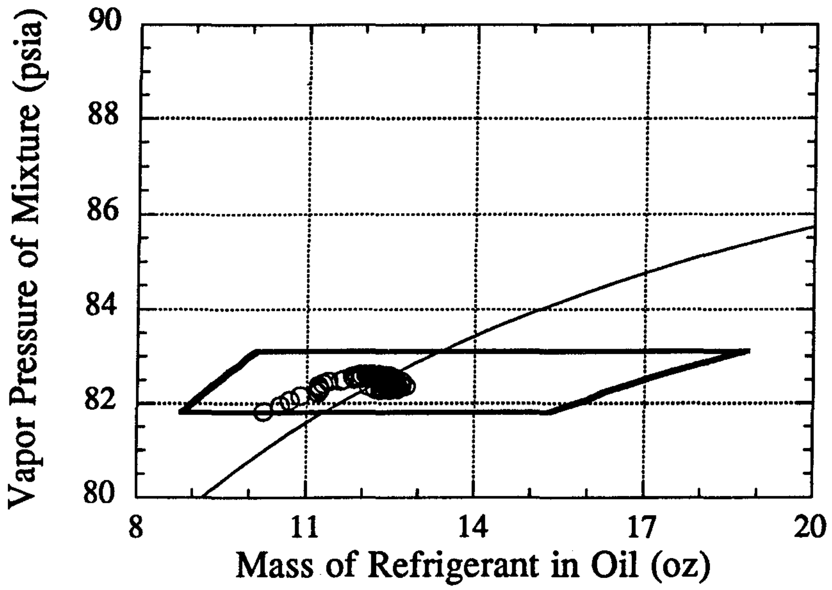

Figure M.4 Error associated with pressure and temperature uncertainty

M.5 Conclusion

During cycling and steady state operation of the Whirlpool refrigerator, the amount of refrigerant dissolved in the oil appears to be low, by approximately 1 to 3 oz. The Grebner-Crawford equations used to predict the amount of refrigerant in the oil appear to be sufficiently accurate for system modeling purposes, but an uncertainty of approximately ± 13% still remains.

When the amount of refrigerant dissolved in the oil is large, for example 60% at the soak condition, the amount of dissolved refrigerant changes by large amounts when pressure and temperature change only slightly. Therefore, given the accuracy of our pressure transducers (± 0.648 psia) and thermocouples (± 1.8 °F), it is not possible to predict accurately the amount of our 8.25 oz of refrigerant charge that is dissolved in the oil sump. The RMS error calculated for the soak condition is around 37.5% which can explain why the Grebner-Crawford equations predict 12.5 oz of refrigerant dissolved in the oil when only 8.25 oz exist in the system. Because the amount dissolved is so sensitive to temperature and pressure at these high concentrations, calculating a total mass during a soak condition cannot be used for determining whether a leak exists in the refrigerator setup.

Appendix N

Cabinet Heater Power Measurement Uncertainty

N.1 Current setup

In running the experimental refrigerator at steady-state conditions, the temperature of both the freezer and fresh food cabinet needs to be controlled to an exact temperature. Currently, electric resistance heaters have been built for both cabinets in order to control the cabinet temperatures. Together, there are three heaters built for the fresh food compartment and three heaters built for the freezer compartment. The original system for controlling and measuring the heater power was designed and described by Staley, Bullard and Crawford (1992). The controller used in controlling the heaters is an Omega Controller Model CN9121. The Omega controller outputs a pulse width modulated signal which is then read by a control box located in each compartment. The control box contains a Solid State Relay circuit which interprets the signal sent by the Omega controller and then switches the power on and off to the heaters appropriately. The Omega system incorporates a PI temperature controller in which the Proportional Time, Dead Band, and Integral Time can be set to different values. Overall there are 7 thermocouples in both the fresh food and freezer cabinets. Six of the thermocouples for each compartment are read directly by the data acquisition system which is used to calculate the average compartment temperature while the seventh thermocouple in each compartment is read by the Omega controller. Also connected to the control box is a 120 VAC power input connected to a watt transducer which is used to measure the amount of power that the control box sends to the heaters. Figure N.1 shows a better picture of the actual setup of the controllers and the heaters. The watt transducers connected to the system are Scientific Columbus Model XL5C5A2. Since the power sent to the heaters are actually a series of on and off pulses, it is necessary to measure the average power dissipated by the heaters. A check at the manufacturer has confirmed that the watt transducers measure only the instantaneous power dissipated by the heaters. Therefore, a first order low pass filter designed by Staley has been connected to the output of the watt transducer to average the power dissipated. The schematic of the filter is shown in Figure N.2. The original setup for the PI controller was designed specifically for the refrigerator that Staley used. With the new instrumentation of the Side-by-Side Amana refrigerator, it was necessary to change some of the parameters and understand how they affect the heater. This appendix will look at different settings and different sampling rates for our PI controller in order to choose the correct settings that will give us the minimum amount of error in our measurements.

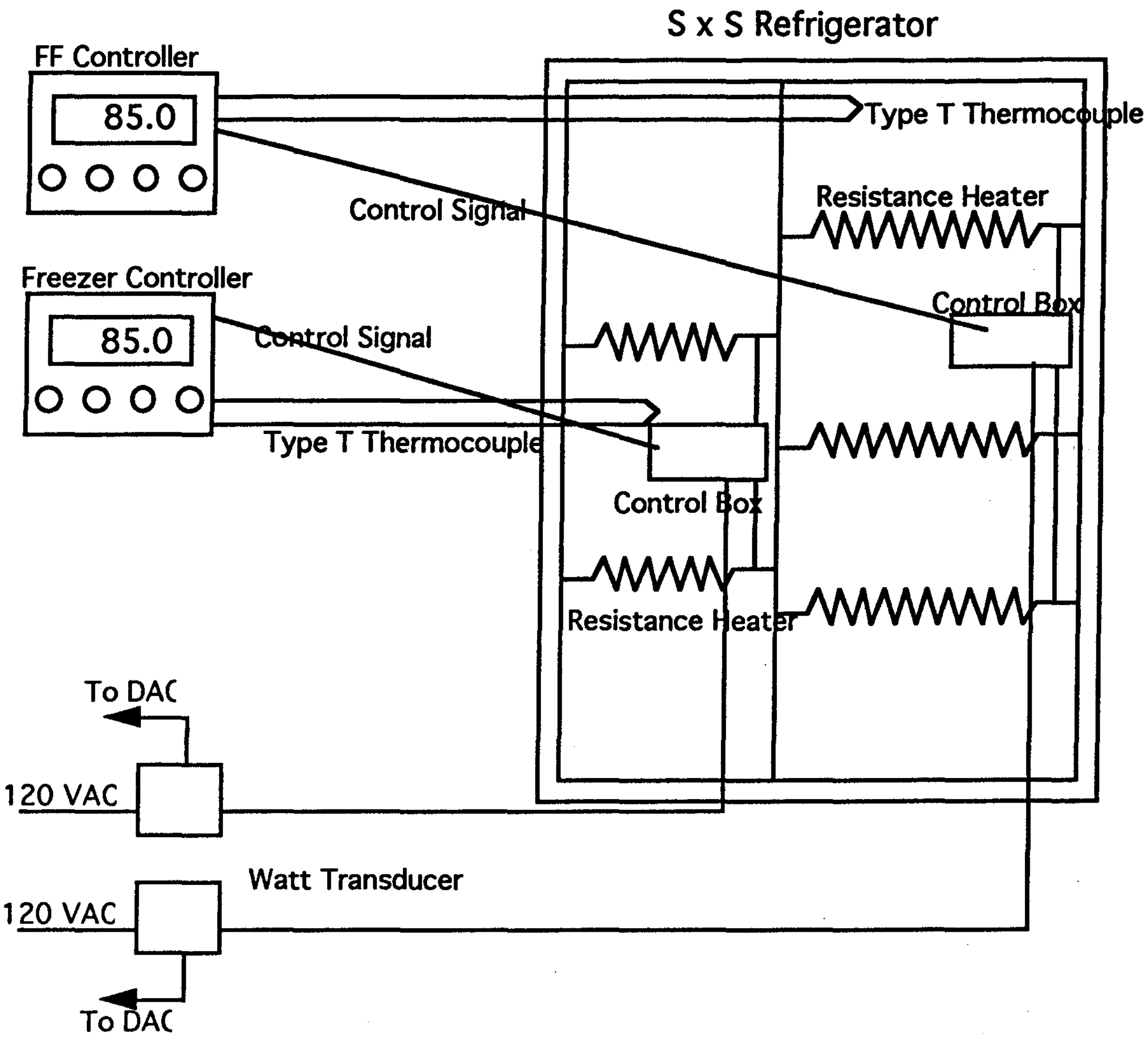

Figure N.1 Heater Control System

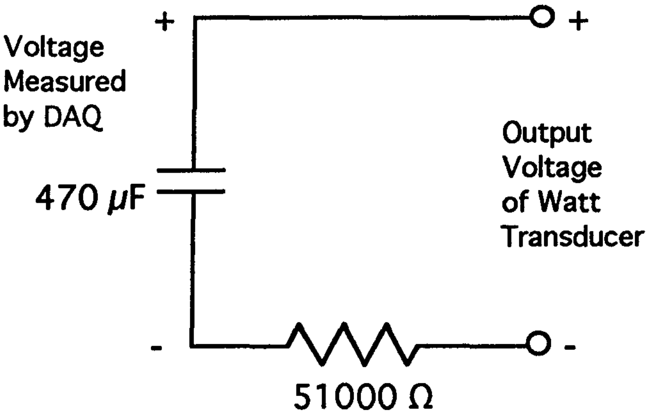

Figure N.2 Low Pass Filter

N.2 Data recorded

As explained earlier, data has been acquired by adjusting the proportional time, dead band, and integral time parameter. The proportional time parameter basically sets the total length of time for a complete on and off cycle. Therefore, if the proportional time is set to 5 sec, then the heaters will turn on and off in a 5 sec. cycle. The dead band basically sets the range at which the controller will start to use PI control. If the temperature is either above or below the dead band range, then the heater powers will be off full power or on full power, respectively. As of now, it is not quite known how the integral time works. With the use of proportional time, there is a great chance that the controller will ultimately steady out at a different temperature from the set point. Integral time is used to help eliminate this offset introduced by using proportional control.

Presently, two data sets were analyzed in which each was taken over a six hour period. The following settings for the proportional, dead band, and integral time for the two data sets are described below in Table N.1. The following test performed with these parameters settings was a reverse heat leak test in which the ambient temperatures are set low at 55 °F and the compartment temperatures are set equal and higher than the ambient at 85 °F so that heat leaks out of the compartment. This type of testing is used to estimate the compartment cabinet conductances as described in Appendix B.

Table N.1 Parameter settings

	Proportional Time	Dead Band	Integral Time
Data Set I	1 sec	1 %	350 sec
Data Set II	5 sec	5 %	350 sec

Figure N.3 shows a graph of the average compartment temperature as measured by six thermocouples located in the fresh food compartment. The average cabinet temperature appears to have remained constant over the time period taken as does the average power dissipated by the heaters at each hour interval as seen in Figure N.4-5. The data was sampled every 2 seconds, but the graphs in Figure N.4-5 show that the heater power for both the fresh food and freezer compartment appear to fluctuate by ±10 W. This type of fluctuation is not uncommon in PI control, but it presents a problem as to how long the sampling rate should be when data is acquired.

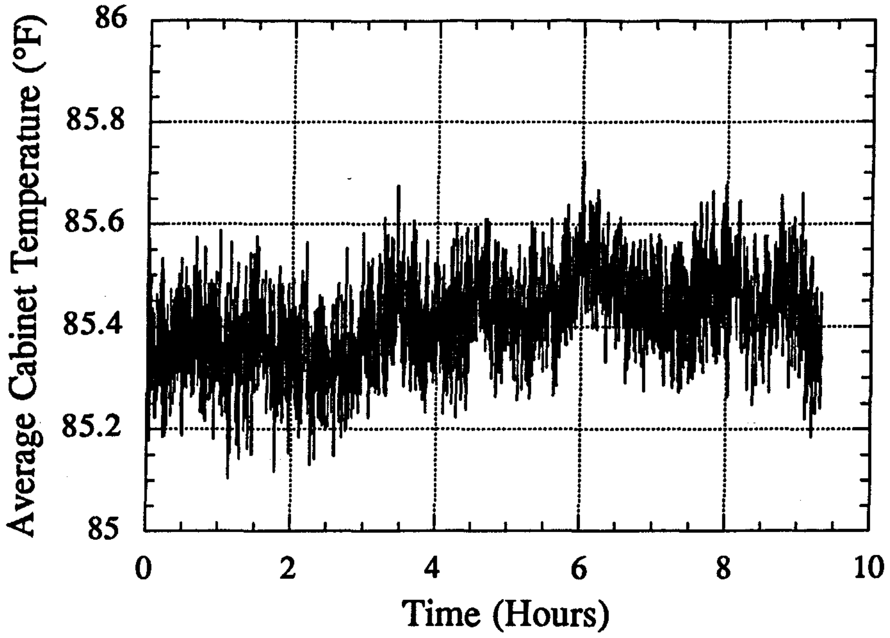

Figure N.3 Cabinet temperature for data set I

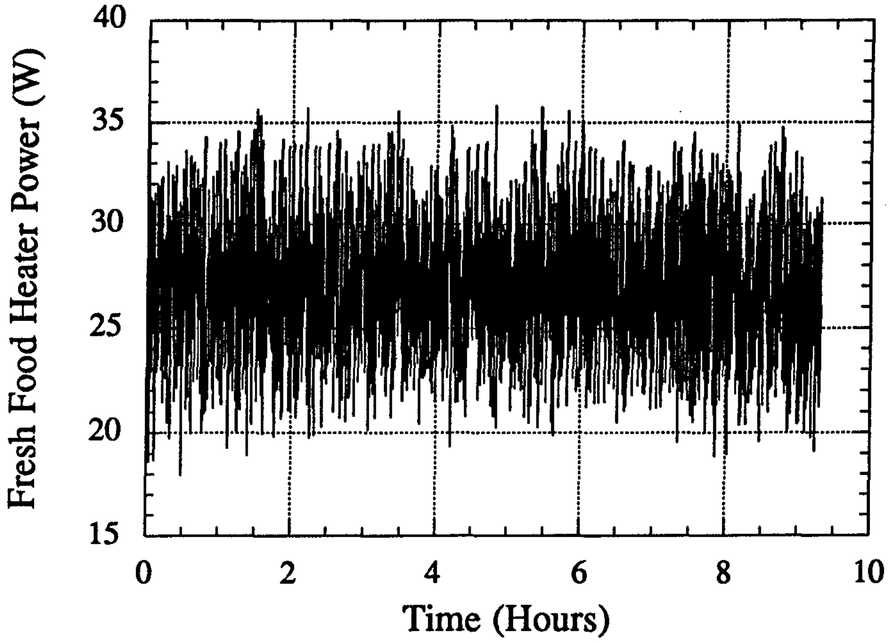

Figure N.4 Fresh food heater power for data set I

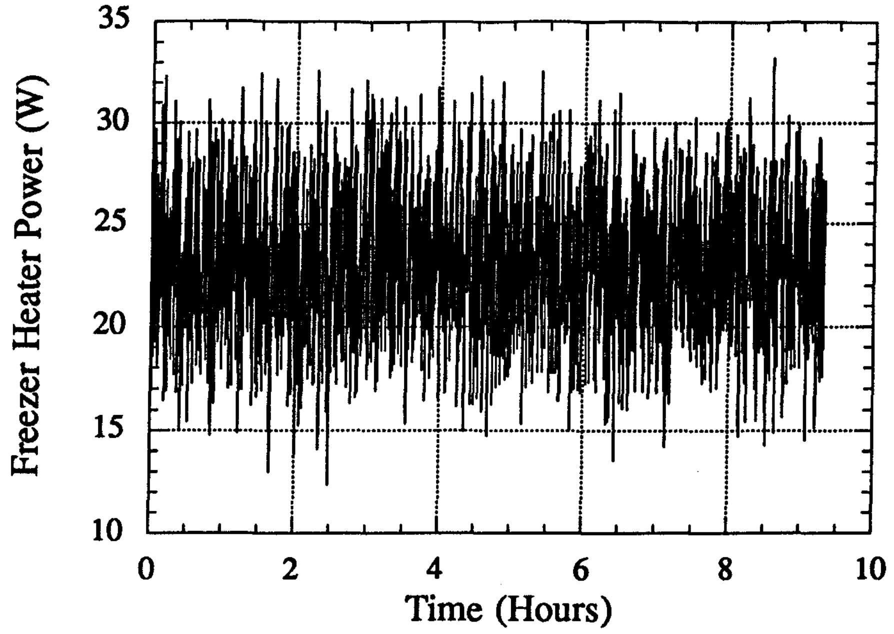

Figure N.5 Freezer heater power for data set I

For data set II, the cabinet temperatures have remained constant over the six hour period as seen in Figure N.6, but this time fluctuations in the heater powers are only ±3 W. The only problem with data set II is that there appears to be general oscillation occurring every ±3 hours. The general oscillation is most likely due to the relaxed dead band of ±5%. Figure N.7-8 shows the graphs pertaining to data set II.

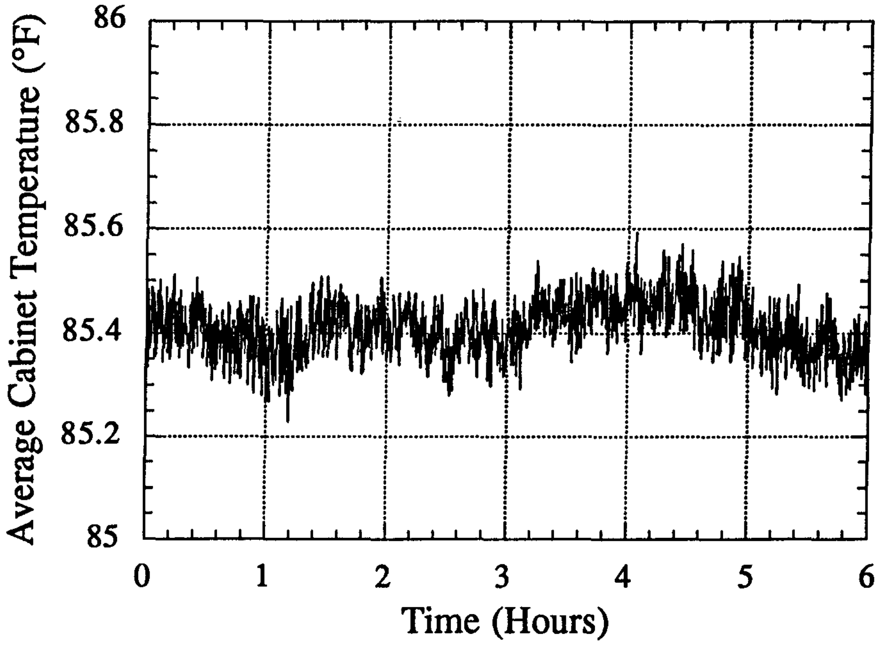

Figure N.6 Cabinet temperature for data set II

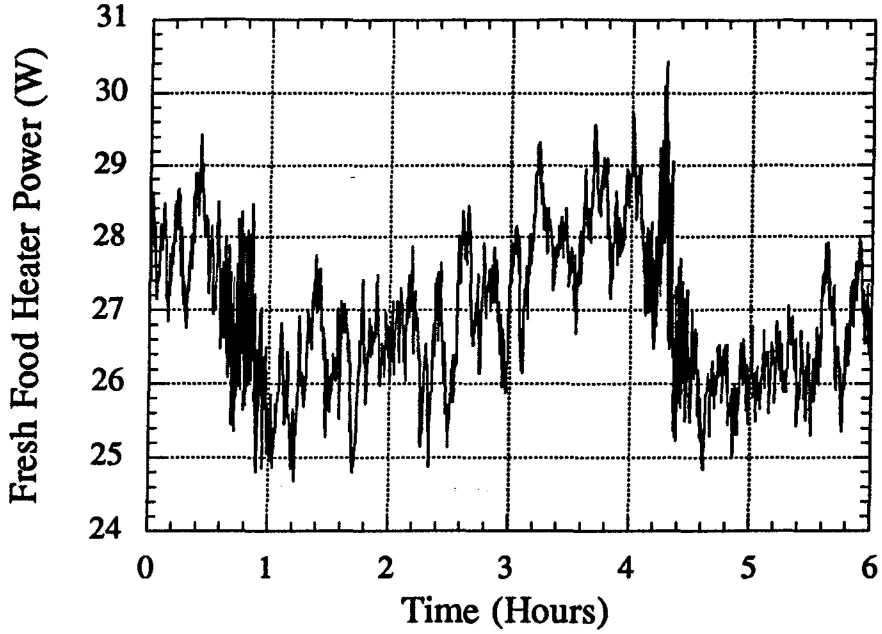

Figure N.7 Fresh food heater power for data set II

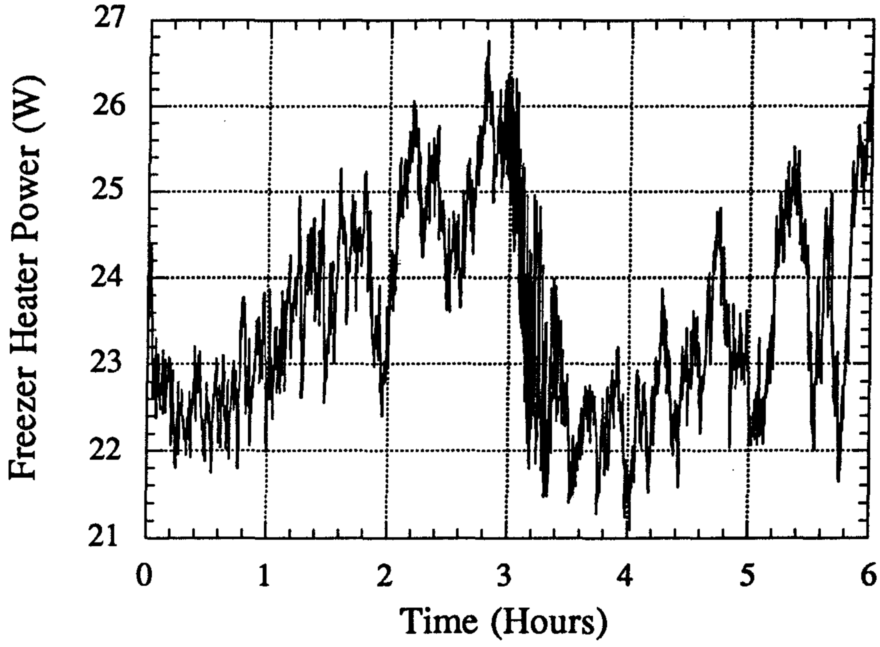

Figure N.8 Freezer heater power for data set I

N.3 Conclusion

From viewing the data taken, averaging data set I over a time period of 1 hour appears to give a constant power. The only problem with data set I is the large power spikes which can be as high as ±10 W from the average. Other settings have been analyzed for the controller and have been found not to reduce this power spike while keeping the power constant. Ways of controlling the spikes in the heater powers are being examined. Perhaps the low pass filter can be redesigned to minimize these spikes. Another alternative which is being considered is to install an integrator on the watt transducer. The integrator would essentially accumulate the W-hr of the heaters and the average power can be obtained by dividing by the total time that the data set was taken.

One approach that has been taken is to reduce the total power that the fresh food heater can output. It has already been seen that once the heaters operate at around their maximum power, the power spike are greatly reduced. For the testing shown in these results, a reverse heat leak test was performed where the heaters outputted around 20-30 W of heat which is around 10% of their total capacity. During steady state operation of the refrigerator, it is seen that at the high compartment temperatures, only around 300 W of heat is needed for the freezer compartment and around 100 W is needed for the fresh food compartment. The original heaters for the freezer and fresh food compartment were designed to give about 300 W of total power each. To reduce the total power in the fresh food compartment, the middle heater was removed which increased the overall resistance of the wire since the three heaters were in parallel. This has helped to decrease the power spike when steady state data is taken. For the reverse heat leak tests, the data still had to be sampled for 2 seconds and averaged over a 1 hour time span to ensure that an accurate measurement was taken for the two heater powers.

Appendix O

Thermocouple Calibration

O.1 Introduction

Before any testing was performed on any of the refrigerator setup, it was necessary to confirm that the forty-eight thermocouples would give accurate temperature readings. The current data acquisition system contains six Strawberry Tree T21 terminal panels and 3 Strawberry Tree ACMC-16 cards. The cards are inserted in the computer and two terminal panels are connected to one card. Each terminal panel contains 8 channels to read eight different thermocouples. The terminal panels are initially calibrated by the manufacturer so it is important that each terminal panel be connected to the its appropriate card.

O.2 Top-mount Whirlpool refrigerator

Initially, the constant temperature bath was used to obtain a constant temperature of 30 °C in the chamber. Using the temperature bath, all forty-eight channels were measured inside the chamber to see how much error existed in each channel. Figure O.1 shows the error for each channel.

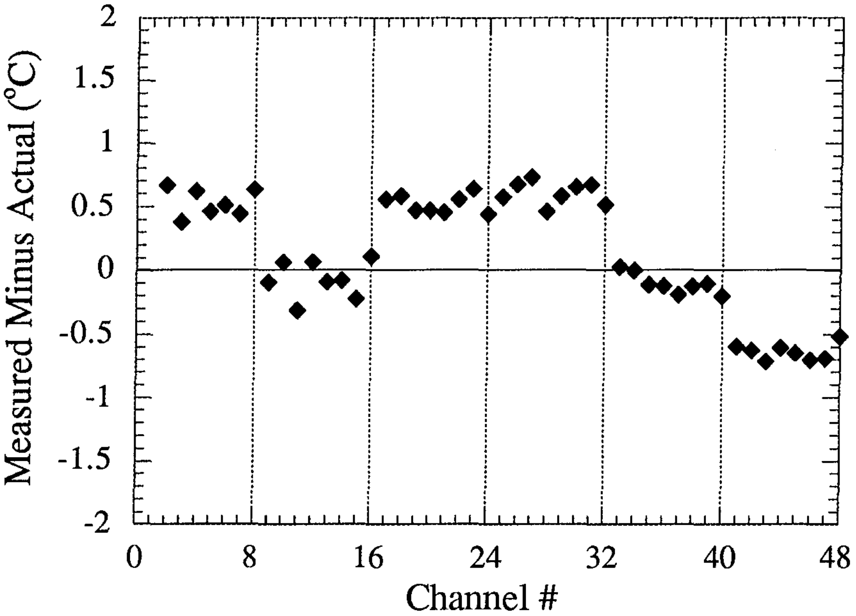

Figure O.1 Thermocouple channel error at temperature of 30 °C (Whirlpool)

Currently, terminal panel two and four appear to read the most accurately. The other panels appear to have some error, but there are ways to reduce the error seen in the all the panels.

O.3 Calibration of thermocouple

From the manufacturer, each terminal panel is calibrated with a CCAL number which is written on the ACMC-16 card. A program called ADRIVE initially reads the calibration number written on the card and saves these numbers in a file called CALIB.DAT. The CCAL numbers written in the data file can be manually changed in order to achieve a more accurate calibration number for each terminal panel. From the manufacturer, it is known that an increase in the CCAL number by 75 points will increase the temperature readings by 1 °C. For each terminal panel, an average error was calculated and used in order to change the CCAL number associated with each terminal panel. After changing the CCAL numbers for all of the terminal panels, all forty eight channels were again tested with the 30 °C temperature bath. Figure O.2 shows how much error existed after changing the CCAL numbers.

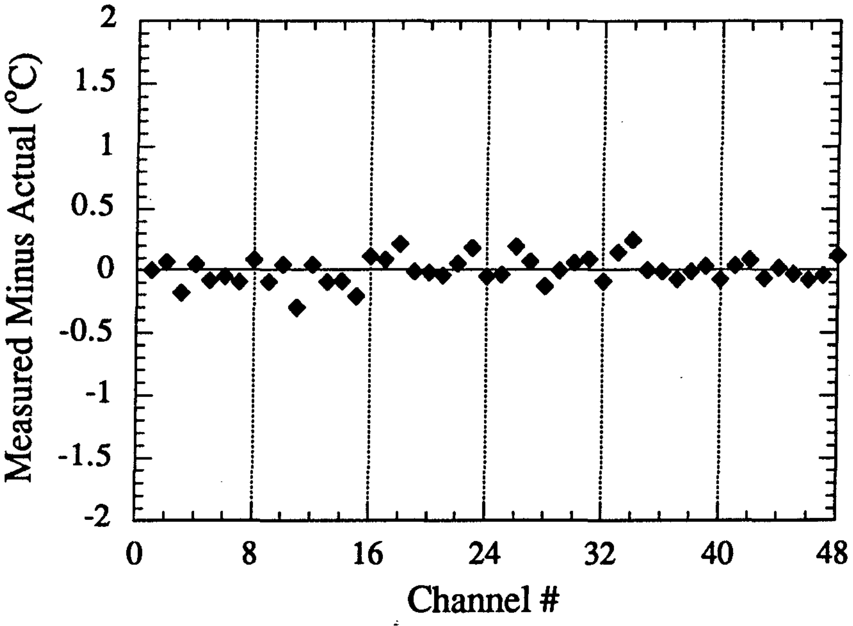

Figure O.2 Thermocouple channel error after recalibration (Whirlpool)

From viewing Figure O.2, it is obvious that the amount of error for each terminal panel has decreased since modifying the CCAL numbers. Each panel of eight thermocouples was altered by a constant correction factor so the relative error of the eight thermocouples to one another remained constant. Now that the average error for each panel has been corrected, the final calibration step will be to create a calibration file which represents the current error in each channel. This is achieved by soaking the refrigerator at an ambient temperature of 75 °F and measuring the temperature for all forty-eight thermocouple. The difference of each thermocouple from the actual chamber temperature will be the correction to add. Whenever data is taken, this calibration file will be used to further correct the temperature data from errors, assuming that the offset at 30 °C applies at all temperatures.

O.4 Side-by-side Amana calibration

With the instrumentation of the Amana side-by-side refrigerator complete, it was necessary to recalibrate all forty-eight thermocouple channel. For the new Amana refrigerator, two different batches of thermocouple wire, as explained in Appendix A, was used so it was necessary to calibrate each panel with its appropriate wire. For the 6 terminal panels, the first three panels used the same wire used in the instrumentation of the Top Mount Whirlpool refrigerator. For the remaining three terminal panels, a new batch of wire was ordered from Omega Electronics (Part # 1045). In order to get a more accurate range of temperature to calibrate from, the constant temperature bath was set to three different temperature (0 °C, 30 °C, and 55 °C). These three temperatures give a good range as to what can be seen in the actual refrigerator. Figure O.3 below shows the error existing in each thermocouple for the thermocouple panel.

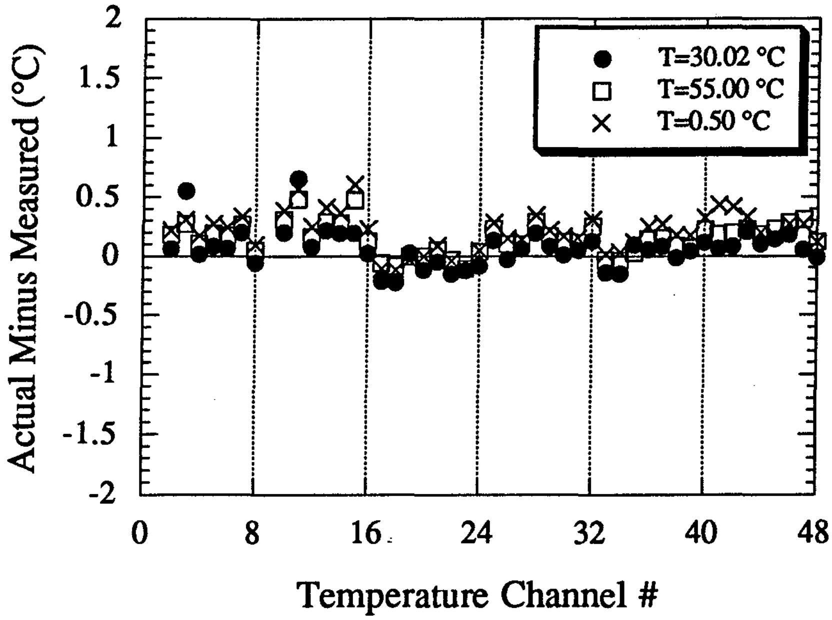

Figure O.3 Thermocouple channel error (SxS Amana)

As can be seen in Figure O.3, the average error in each terminal panel is less than 0.5 °C. Although the terminal panels appear to read temperatures accurately within 0.5 °C, the average error was still corrected in order to get a more accurate reading. This was accomplished as before where the CCAL number was changed by 75 for every 1 °C that the average of each terminal panel was off by. Once new CCAL numbers were determined for all 6 terminal panels, the constant temperature bath was again set to 30 °C to see what errors now existed. The results of current existing errors for each thermocouple channel is shown in Figure O.4.

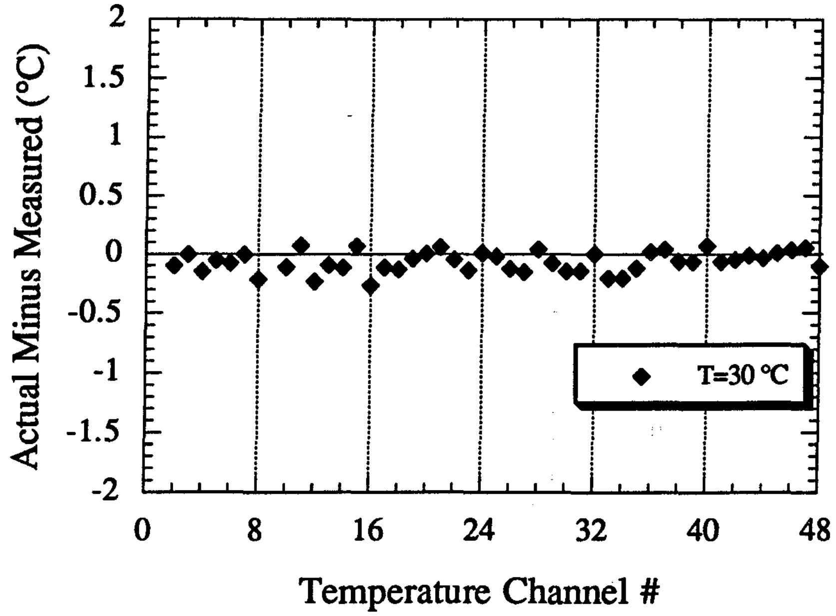

Figure O.4 Thermocouple channel error after recalibration (SxS Amana)

As we now can see from Figure O.4, the average error for each terminal panel appears to be about 0 °C. From here, a final correction value is obtained for each thermocouple as described before. The chamber was soaked at 90 °F and the current error in each thermocouple was recorded and will be used as its correction factor whenever data is taken with the experimental refrigerator.